Kinetic Studies with Shock Tubes:
Instrumental Developments and the
Thermal Decomposition of Furan Derivatives

Zur Erlangung des akademischen Grades eines

DOKTORS DER NATURWISSENSCHAFTEN
(Dr. rer. nat.)

von der KIT-Fakultät für Chemie- und Biowissenchaften
des Karlsruher Instituts für Technologie (KIT)

genehmigte

DISSERTATION

von

Dipl.-Chem. Isabelle Kathrin Weber

Dekan: Prof. Dr. Reinhard Fischer
Erster Gutachter: Prof. Dr. Matthias Olzmann
Zweiter Gutachter: PD. Dr. Patrick Weis
Tag der mündlichen Prüfung: 17.10.2017

This document is licensed under a Creative Commons
Attribution-ShareAlike 4.0 International License (CC BY-SA 4.0):
https://creativecommons.org/licenses/by-sa/4.0/deed.en

A huge THANK YOU to

Prof. Dr. Matthias Olzmann for the opportunity of writing this work the way it went.

Patricia Hibomvschi, not only for all the technical help, but also for the floor internal chocolate trade.

The mechanical and electrotechnical workshops for the technical support.

PD Dr. Andreas-Neil Unterreiner for discussions about the experiment, and mathematical gimmicks.

Desmond Kelly for help with all IT issues, and the identification of missing and unnecessary commas in the latest version of this manuscript.

Daniela Rohmert-Hug for the administrative help, and patience with my sometimes chaotic organisation.

Dr. Binod Giri from KAUST for the opportunity to visit, and the introduction to the alternative membrane system.

The fellow PhD students of the group. Especially to Leonie Golka, Lena Genthner, and Johannes Kiecherer for the daily lab and office life. And to the ones correcting the PCII exams this term for covering.

The students throughout the years, Sabrina Syskowski, Leonie Golka, Fabian Hundemer, Tobias König, Manuel Kraft, and Felix Poschen for the good work done.

Mensa Karlsruhe and TNS for a diverse environment besides the university setting. Especially to Anne, Julian, Christian, and Jens for often short nights and good laughs.

My family for the support the last years and before. And a helping hand whenever needed.

Contents

Zusammenfassung v

1 Introduction 1

2 Theoretic Foundations 3

2.1 Shock Wave Experiments 3

2.2 Atomic Resonance Absorption Spectroscopy (ARAS) 7

2.2.1 Line Absorption Theory 8

2.2.2 Detection 12

2.2.3 Calibration 13

2.3 Introduction to Reaction Kinetics 17

2.3.1 Reaction Mechanisms 17

2.3.2 Analysis of Complex Reaction Mechanisms 18

2.3.3 Temperature and Pressure Dependence of Rate Coefficients 19

2.3.4 Experimental Determination of Rate Coefficients 21

3 Experiment 23

3.1 Experimental Setup 23

3.1.1 Shock Tube 23

3.1.2 ARAS Setup 24

3.1.3 Mixing System 25

3.2 Experimental Procedure 26

3.3 Mixtures 26

3.4 Software 27

3.5 Errors and Uncertainties 27

4 Instrumental Modifications 29

4.1 Overview 29

4.2 Test of an Alternative Membrane System 29

4.3 The Dual ARAS Experiment 33

4.3.1 The Second ARAS Setup 33

4.3.2 The Oxygen Filter 35

4.3.3 A Vertical I ARAS Setup 37

4.4 The Atom Filter 40

4.5 Outlook: Variations of the Dual ARAS Setup 43

5 Thermal Decomposition of Ethyl Iodide: A Test for the Dual ARAS System ... 45

5.1 Introduction 45

5.2 Experiments and Calibration 47

5.3 Experimental Results: Comparison to the Mechanism by Varga et al. [65] 49
5.4 I ARAS Calibration 51
5.4.1 Iodine Monochloride: An Alternative I Atom Source 51
5.4.2 Thermal Decomposition of Methyl Iodide 53
5.5 Reinterpretation of the Ethyl Iodide Experiments 62
5.6 Conclusions 65

6 Thermal Decomposition of Furan and its Methyl Substituted Derivatives 66
6.1 Introduction 66
6.2 Literatur Overview and Choice of Mechanism 67
6.3 Furan 70
6.3.1 Initial Reaction Pathways in Furan Pyrolysis 70
6.3.2 Experiments 71
6.3.3 Mechanistic Considerations 71
6.3.4 Formation of H atoms in the Pyrolysis of Furan 75
6.4 2-Methylfuran (2-MF) 78
6.4.1 Initial Reaction Pathways in 2-MF Pyrolysis 78
6.4.2 Experiments 78
6.4.3 Mechanistic Considerations 79
6.4.4 Formation of H Atoms in the Pyrolysis of 2-MF 83
6.5 Formation of H Atoms in the Pyrolysis of 2,5-Dimethyfuran (2,5-DMF) 85
6.6 The 2017 Mechanism by Tran et al. [103] 87
6.7 Conclusions 90

7 Overall Conclusions and Outlook 93

Appendix 97
A.1 Chemicals and Gases 97
A.2 Identified Atomic Emission Lines in Accordance with Ref. [28] 98
A.2.1 Hydrogen (H) 98
A.2.2 Nitrogen (N) 98
A.2.3 Carbon (C) 99
A.2.4 Oxygen (O) 99
A.2.5 Chlorine (Cl) 100
A.2.6 Iodine (I) 100
A.3 Abbrevations of Experimental Techniques 102
A.4 Experimental Conditions and Rate Coefficients for the Thermal Decomposition of Methyl Iodide 103
A.5 Experimental Conditions and Branching Ratios for the Thermal Decomposition of Ethyl Iodide 104

A.6 Experimental Conditions for the Thermal Decomposition of Furan Detivatives 105
A.6.1 Furan 105
A.6.2 2-Methylfuran 105
A.6.3 2,5-Dimethylfuran 105
A.7 Rate Coefficients Implemented in the Modified Furan Mechanism 106

Bibliography 107

Publications 115

Curriculum Vitae 117

Zusammenfassung

Ziel dieser Arbeit war der Aufbau und Test einer Apparatur zur zeitgleichen Messung zweier atomarer Spezies in Stoßwellenexperimenten. Aufgrund der Bedeutung von iodierten Radikalvorläufern in der Untersuchung von Zerfallsreaktionen von Kohlenwasserstoffradikalen, wurde der bestehende Stoßrohr/H ARAS Aufbau um eine I ARAS Apparatur ergänzt. Um die Qualität der H ARAS Messunge zu erhalten, wurde diese in der zweiten Detektionsebene montiert. Variationsmöglichkeiten wurden diskutiert.

Der neue Aufbau wurde in Untersuchungen zum thermischen Zerfall von Ethyliodid erstmals getestet. Die bestimmten Verzweigungsverhältnisse der zwei Zerfallskanäle des Ethyliodids stimmen gut mit den bekannten Literaturwerten überein. Im Rahmen der Messungen wurden Unstimmigkeiten in der Kalibrierung des I ARAS festgestellt. Um diese zu beheben wurde die Geschwindigkeitskonstante für die C-I Bindungsspaltung in Methlyiodid mit Hilfe von I ARAS Messungen neu bestimmt.

Im zweiten Teil der Arbeit wurde der thermische Zerfall der Furanderivate Furan, 2-MF und 2,5-DMF näher untersucht. Die erhaltenen Messergebnisse konnten durch die Anpassung eines Literaturmechanismus für die Oxidation der Furanderivate erklärt werden. Mittels Sensitivitätsanalysen und Reaktionsflussanalysen wurden die wichtigsten Reaktionskanäle für die Bildung von Wasserstoffatomen identifiziert.

Damit konnten in dieser Arbeit die apparativen Voraussetzungen für eine genauere Untersuchung der thermischen Zerfallsreaktionen von Kohlenwasserstoffradikalen in Stoßwellenexperimenten geschaffen werden.

1 Introduction

The combustion of hydrocarbons and other fuels accounts for a great part of todays energy supply. Due to the restricted amount of fossil fuels, the focus shifts to alternative biofuels. To assess their combustion properties, and their tendency to form possibly hazardous products, a lot of effort is put into the investigation of their oxidation and pyrolysis behaviour. However, the extreme conditions in combustion processes, especially the high temperatures, make an investigation experimentally challenging.

Combustion chemistry can be investigated directly in flames. In this case, the high number of different processes occurring (e.g. chemical reactions, transport processes) make a simulation of the experimental results difficult. Information about specific reactions can hardly be deduced from flame measurements. A different method for the generation of high temperatures is the use of shock tubes and shock waves. In a traditional membrane shock tube, high temperatures in a probe gas are generated by passing of a shock wave through the probe gas.

Under pyrolytic conditions, H atoms are the predominant chain carrier species. Thus, the concentration of H atoms mainly influences the temporal development of the system (e.g. conversion rates, product yields, species concentrations). H atoms at short reaction times are primarily formed from the reactant by bond fission reactions. Consequently, information about these reactions can be directly deduced from H atom concentrations at short reaction times. With increasing concentration of H atoms, the influence of bimolecular consumption pathways increases. One important pathway is the abstraction of H atoms from the reactant or other molecules by H atoms yielding H_2. Information about these consecutive reactions can also be deduced from H atom concentration-time profiles.

A very sensitive method for the measurement of atom concentrations is the atomic resonance absorption spectroscopy (ARAS). It is commonly employed for the determination of H atom concentrations in shock rube experiments [3]. Due to its high sensitivity, experiments on very dilute mixtures can be conducted. Thereby, it is possible to reduce the influence of bimolecular reactions, and to directly determine rate coefficients for H atom forming reactions from the recorded concentration-time profiles. However, with increasing complexity of the reactant, the number of H atom forming and consuming reaction pathways increases. Usually, the decomposition of the radicals formed form the reactant in the initial reaction steps has a non-negligible influence on the concentrations of H atoms in the system. Therefore, it is of interest to investigate the decomposition of these radicals.

In shock tube experiments, hydrocarbon radicals are often generated from iodinated radical precursors molecules. In these molecules, the C-I bond is usually the weakest bond. Nonetheless, the elimination of hydrogen iodide is often competitive to the C-I bond fission reaction. To assess the initial concentration of the radical, branching fractions of the initial reaction pathways must be known. These can be determined from measurements of I atom yields, for example by I ARAS experiments. As the reproducibility of shock tube experiments is restricted, it would be advantageous to follow the concentration of both species, H and I atoms, simultaneously.

In this work, the existing shock tube/ARAS setup has been extended by a second ARAS detection unit. Thereby it is possible to record concentration-time profiles of two atomic species simultaneously. The second ARAS setup was mounted perpendicular to the already existing one. Throughout this work, they will be denoted as ‘horizontal’ and ‘vertical’ ARAS unit in accordance with their spatial orientation. In the original horizontal ARAS system, a monochromator is used as dispersing component to isolate the detection wavelength. Due to the restricted space in the vertical detection axes, the utilization of a monochromator in the vertical ARAS unit was not possible. Different approaches to restrict the wavelength range detected (e.g. choice of optical materials) are considered. Both combinations of H and I ARAS (vertical H ARAS/horizontal I ARAS and vice versa) are discussed and advantages and disadvantages are elucidated. Remarks on a further application of the dual ARAS setup to other ARAS techniques are given.

As a first trial of a H ARAS/I ARAS combination, the thermal decomposition of ethyl iodide was investigated. This system is especially suitable, since the underlying mechanism is well known. However, a comparison of simulated and measured concentration-time profiles indicated inconsistencies in the calibration of I ARAS with methyl iodide. Therefore, the thermal decomposition of methyl iodide itself was studied, and the rate coefficient for the C-I bond fission reaction of methyl iodide was revaluated based on the results of new I ARAS experiments. Additionally, the formation of H atoms in the high temperature thermal decomposition of methyl iodide was examined.

For the implementation of a vertical H ARAS setup, an oxygen filter was developed. This filter could also be operated as an atom filter. In a first trial of the atom filter, the amount of resonance radiation emitted by the H ARAS lamp was determined and compared to earlier high temperature experiments on highly concentrated hydrogen mixtures. Furthermore, in a trial to improve the reproducibility of the experimental conditions in the shock tube experiments, an alternative membrane system was tested. The new system simplifies the experiment as the uncontrolled splintering of the diaphragm is avoided.

In a second part, the pyrolysis of furan and its two methyl substituted derivatives 2-methylfuran (2-MF) and 2,5-dimethylfuran (2,5-DMF) was investigated in shock tube/H ARAS experiments. Information about the initial reaction steps was deduced from an extensive literature review and integrated into an oxidation mechanism for the three furan derivatives published by Liu et al. [4-6] The modified mechanism was analysed to highlight the formation pathways of H atoms. Trends in H atom formation were discussed.

With this work, the instrumental requirements for a thorough investigation of thermal decomposition reactions of radicals in shock tube experiments were established in our shock tube facility.

2 Theoretic Foundations

2.1 Shock Wave Experiments

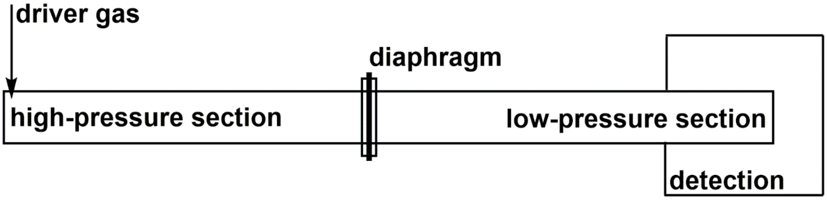

Figure 2.1: Schematic layout of a membrane shock tube.

A schematic setup of a shock tube experiment is depicted in figure 2.1. The shock tube consists of a high- and a low-pressure section, which are separated by a diaphragm. By introducing the driver gas into the high-pressure section, the pressure difference between the two sections increases. At some point, the diaphragm bursts. Subsequently, compression waves spread into the probe gas in the low-pressure section. Their velocity equals the sound velocity as, which is related to the temperature of the medium by

$$a_\mathrm{s} = \sqrt{\frac{\kappa \mathrm{R} T}{M}}. \tag{2.1}$$

$$\kappa = c_\mathrm{p} / c_\mathrm{v} \tag{2.2}$$

R denotes the ideal gas constant. κ is the adiabatic coefficient of the gas in the low-pressure section, which is defined by equation (2.2), T its temperature and M its molar mass. Each compression wave leads to an adiabatic compression of the gas and thereby to an increase in temperature and pressure. As later compression waves propagate through the already heated medium, their velocity is higher. In consequence, they overtake previously formed waves. A shock front is formed which moves with supersonic velocity with respect to the probe gas. The thickness of the shock front amounts to a few mean free path lengths. At the end of the low-pressure section, the shock wave is reflected. It then moves through the already compressed gas, leading to a second jump in temperature and pressure.

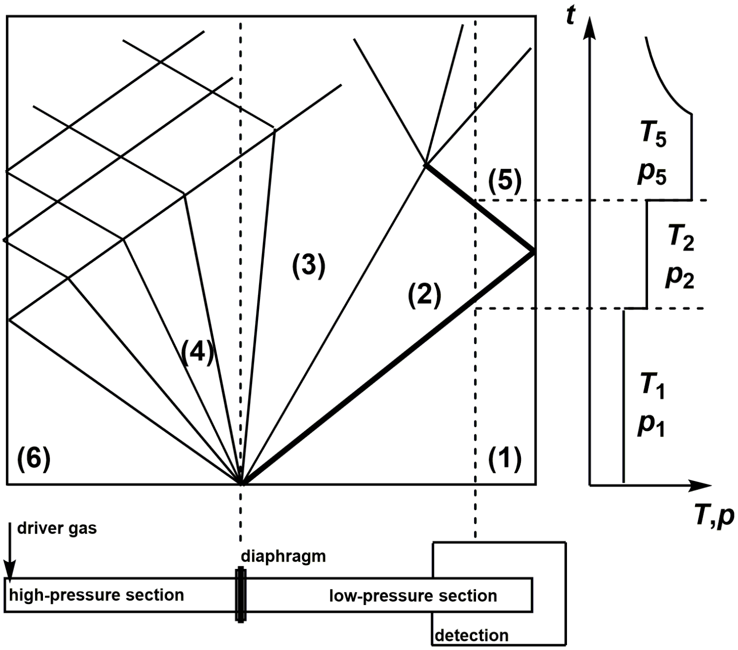

Figure 2.2: Shock wave propagation in a shock tube (left) and evolution of temperature and pressure in the plane of detection (right), according to [7-9].

In figure 2.2, the propagation of a shock wave in a shock tube is summarized and different states of driver and probe gas are highlighted. These states can be assigned to

(1) The gas in the low-pressure section before the passing of the shock wave.

(2) The probe gas in the low-pressure section after the transition of the incident shock wave.

(3) The driver gas after transition of the expansion waves.

(4) The driver gas during the passing of the expansion waves.

(5) The probe gas in the low-pressure section after the transition of the reflected shock wave.

(6) The gas in the high-pressure section before the passing of the expansion waves.

To define the experimental conditions behind the reflected shock wave, a mathematical description of the shock wave is necessary. Therefore, some assumptions have to be made:

- No energy and momentum is transferred between the shock wave and the shock tube wall.
- The thermal boundary layer close to the shock tube wall can be neglected.’

- All gases are regarded as ideal gases and fulfil the ideal gas equation (2.7).
- The diaphragm bursts without interaction with the gases or the shock tube wall.

With respect to a coordinate system with origin in the shock front, the conservation laws for mass, energy and momentum can be formulated as

mass
$$\rho_1 u_1 = \rho_2 u_2, \tag{2.3}$$

momentum
$$p_1 + \rho_1 u_1^2 = p_2 + \rho_2 u_2^2, \tag{2.4}$$

energy
$$E_1 + \frac{u_1^2}{2} + \frac{p_1}{\rho_1} = E_2 + \frac{u_2^2}{2} + \frac{p_2}{\rho_2}. \tag{2.5}$$

E denotes the energy per mass unit, ρ the mass density and u the flow velocity. Additionally, caloric (2.6) and ideal gas (2.7) state equations are considered:

$$E_2 - E_1 = c_\mathrm{v}(T_2 - T_1), \tag{2.6}$$

$$pV = n\mathrm{R}T. \tag{2.7}$$

With these, the conservation laws (2.3) - (2.5) can be solved to give relations between the conditions before and after the incident shock wave as a function of the shock Mach number M_1 (2.8):

$$M_1 = \frac{u_1}{a_\mathrm{S}}, \tag{2.8}$$

$$\frac{p_2}{p_1} = \frac{2\kappa M_1^2 - (\kappa - 1)}{\kappa + 1}, \tag{2.9}$$

$$\frac{\rho_2}{\rho_1} = \frac{u_1}{u_2} = \frac{(\kappa + 1)M_1^2}{(\kappa - 1)M_1^2 + 2}, \tag{2.10}$$

$$\frac{T_2}{T_1} = \frac{p_2}{p_1} \cdot \frac{\rho_1}{\rho_2} = \left(\frac{2\kappa M_1^2 - (\kappa - 1)}{\kappa + 1}\right) \cdot \left(\frac{(\kappa - 1)M_1^2 + 2}{(\kappa + 1)M_1^2}\right). \tag{2.11}$$

Under the assumption that the shock wave is perfectly reflected at the end of the low-pressure section, the conditions behind the reflected shock wave can be calculated by

$$\frac{p_5}{p_1} = \left(\frac{(3\kappa - 1)M_1^2 - 2}{M_1^2 + \frac{2}{\kappa - 1}}\right) \cdot \left(\frac{\left(\frac{2\kappa}{\kappa - 1}\right)\mathrm{M}_1^2 - 1}{\frac{\kappa + 1}{\kappa - 1}}\right), \tag{2.12}$$

$$\frac{\rho_5}{\rho_1} = \frac{\frac{\kappa + 1}{\kappa - 1} M_1^2 \left(\frac{2\kappa}{\kappa - 1} M_1^2 - 1\right)}{\left(M_1^2 + \frac{2}{\kappa - 1}\right) \cdot \left(2M_1^2 + \frac{3 - \kappa}{\kappa - 1}\right)}, \tag{2.13}$$

$$\frac{T_5}{T_1} = \frac{\left(\left(\frac{3\kappa - 1}{\kappa - 1}\right) M_1^2 - 2\right) \cdot \left(2M_1^2 + \frac{3 - \kappa}{\kappa - 1}\right)}{\left(\frac{\kappa + 1}{\kappa - 1}\right)^2 M_1^2}. \tag{2.14}$$

If highly diluted mixtures are investigated, the heat capacities c_v and c_p are determined by the properties of the bath gas. For a monoatomic noble gas (ideal in first approximation) they are given by

$$c_\mathrm{v} = \frac{3}{2}\,\mathrm{R}, \tag{2.15}$$

$$c_\mathrm{p} = \frac{5}{2}\,\mathrm{R}. \tag{2.16}$$

To increase the reproducibility of the experimental conditions in shock tube experiments, a slightly different method of shock wave generation is often chosen. Instead of a spontaneous rupture of the diaphragm due to the pressure difference between high- and low-pressure section, the membrane is cut manually [7]. In these experiments, the experimental conditions are determined by the ratio of driver gas to probe gas introduced into the shock tube prior to the destruction of the membrane. To predict the pressure of driver gas necessary to generate the desired experimental conditions, a relation between the pressure in the high-pressure section at the beginning of the experiment (p_6) and the pressure of the probe gas behind the incident (p_2) or reflected shock (p_5) is needed.

These relations can be derived, if the changes induced by the expansion waves are considered (for a complete description see [7]):

$$\frac{p_2}{p_6} = \left(1 - \frac{\frac{f_1 a_1}{f_6 a_6}\left(\frac{p_2}{p_1} - 1\right)}{(2 + f_1) \cdot \left(1 + \frac{1 + f_1}{2 + f_1}\left(\frac{p_2}{p_1} - 1\right)\right)^{0.5}} \right)^{2+f_6} \tag{2.17}$$

$$\frac{p_5}{p_6} = \frac{(3 + f_1)M_1^2 - 2}{M_1^2 + f_1} \cdot \left(1 - \frac{f_1 a_1}{f_6 a_6}\frac{M_1^2 - 1}{(1 + f_1)M_1}\right)^{2 + f_6} \tag{2.18}$$

a_1 and a_6 are the sound velocity in the probe gas and the driver gas respectively. f_1 and f_6 denote the number of degrees of freedom for the two gases. For a monoatomic gas, f equals three. For a diatomic molecule, f equals five.

From equations (2.9) and (2.17) a relation between the shock Mach number and initial pressures of driver and probe gas can be derived:

$$\frac{p_6}{p_1} = \frac{1 + \frac{2 + f_1}{1 + f_1}\left(M_1^2 - 1\right)}{\left(1 - \frac{f_1 a_1}{f_6 a_6} \cdot \frac{M_1^2 - 1}{(1 + f_1)M_1}\right)^{2 + f_6}} \tag{2.19}$$

The higher the shock Mach number, the greater is the increase in temperature and pressure after passing of the shock wave. For a simple membrane shock tube, the thickness and the stability of the membrane define the pressure differences reachable. For a fixed initial pressure of probe gas in the low-pressure section, a thicker diaphragm will lead to a higher pressure and temperature behind the shock wave.

Driver and driven gas are usually chosen to obtain a maximum pressure and temperature jump with a minimum amount of driver gas. In most cases, the detection method employed determines the choice of the driven gas. As the driver gas, a light weight gas should be used. Common choices are helium and H_2. H_2 is the more effective driver gas. However, it sometimes cannot be utilized due to its reactivity.

2.2 Atomic Resonance Absorption Spectroscopy (ARAS)

Atomic resonance absorptions spectroscopy (ARAS) is a very sensitive method for the detection of atomic species (lower detection limit H ARAS: ~ 5×10^{-12} mol cm^{-3} [3]). Myerson et al. [10] were the first to combine the ARAS technique with a shock tube setup to quantitatively follow the production of hydrogen atoms in the high temperature thermal decomposition of (H_2).

Throughout the years, ARAS has been applied to numerous different atomic target species. Some of them are exemplarily listed in table 2.1.

Table 2.1: Different ARAS techniques, the associated detection wavelength and calibration systems (based on [3]).

target species	λ / nm	calibration	ref.
N	119.9	NO or N_2	[11, 12]
D	121.5	N_2O/D_2	[13]
H	121.6	N_2O/H_2 or H_2	[13, 14]
O	130.4	N_2O	[15-17]
Cl	137.9	CH_3Cl	[18, 19]
C	156.1	CH_4	[20, 21]
I	183.0	CH_3I	[22, 23]

Key part of an ARAS experiment is the ARAS lamp or light source. Usually, a microwave discharge lamp is used. The lamp gas contains the ARAS target species precursor (e.g. H ARAS: H_2 [10], I ARAS: CH_3I [22], Cl ARAS: Cl_2 [19]).

2.2.1 Line Absorption Theory

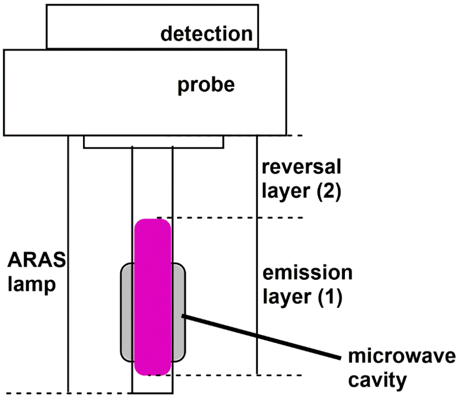

Figure 2.3: Two layer model for the description of an ARAS lamp.

Emission and absorption processes within an ARAS lamp can simplified be described by a two layer model [3, 24, 25]. The differentiation of the layers is illustrated in figure 2.3. The first layer is the ‘emission layer’ within the lamp. In this layer, excited atoms are generated by microwave discharge. Resonance radiation is emitted due to the relaxation of the excited atoms to the ground state. The second layer is directly bordered to the emission layer. In this ‘reversal layer’, resonance radiation generated in the emission layer is absorbed by atoms in the ground state. Depending on its length and the concentration of absorbing atoms in this layer, the line shape can become completely reversed – the so called self-absorption or self-reversal phenomena (for a detailed description, see Cowan and Dieke [26]). Thereby, the presence of the ‘reversal layer’ leads to the necessity of a separate calibration procedure as Beer-Lamberts law only holds for infinitely narrow emission lines, and exact line shape calculations are difficult.

For a mathematical description of the total emission of an ARAS lamp, some assumptions have to be made [25]:

- Emission only occurs in a restricted emission layer with the length l_1.
- Emitters are uniformly distributed in this layer. There are no concentration gradients.
- Reemission of absorbed resonance radiation is negligible.

Under these conditions, the frequency distribution ($E_1(v)$) of the radiation emitted by emission layer can be written as

$$E_1(v) = 1 - \exp(-\sigma_1(v)[\mathrm{X}]_1 l_1). \tag{2.20}$$

$[\mathrm{X}]_1$ denotes the concentration of the emitting atoms (species X) in the emission layer. If a Doppler line shape is assumed for the emission line, the absorption cross section in layer i, $\sigma_i(v)$, is given by

$$\sigma_i(v) = \sigma_0 \exp\left(-\left(\frac{\gamma(v)}{\alpha_i}\right)^2\right). \tag{2.21}$$

σ_0 is the absorption cross section at the centre wavelength. The quantity γ describes the line form caused by doppler broadening. It is connected to the centre line frequency v_0 by

$$\gamma(v) = \frac{v - v_0}{\delta_i}, \tag{2.22}$$

with the Doppler line width

$$\delta_i = \frac{v_0}{\mathrm{c}}\left(\frac{2\mathrm{R}T_i}{M}\right)^{0.5}. \tag{2.23}$$

α_i accounts for temperature differences between the layers. If the reversal layer is accepted as reference state and its temperature is assumed to be 298 K [3], α_i is defined as

$$\alpha_i = \left(\frac{T_i}{298\ \mathrm{K}}\right)^{0.5} \tag{2.24}$$

with T_i as the temperature of the layer i.

The reversal layer (length l_2, concentration $[\mathrm{X}]_2$) is a purely absorbing layer. Its emission ($E_2(\nu)$) depends on the emission ($E_1(\nu)$) of the emission layer and the absorption cross section $\sigma(\nu)$ of the absorbing species [24]. $E_2(\nu)$ is the total emission of the ARAS lamp.

$$E_2(\nu) = E_1(\nu) \cdot \exp(-\,\sigma_2(\nu)[\mathrm{X}]_2 l_2) \tag{2.25}$$

If the emission line consists of an overlapping multiplet, equations (2.20) and (2.25) have to be slightly modified. Fractions by all j components must be summed up:

$$E_1(\nu) = 1 - \exp\left(\textstyle\sum_j(-\,\sigma_1(\nu,j)[\mathrm{X}]_1 l_1)\right) \tag{2.26}$$

$$E_2(\nu) = E_1(\nu) \cdot \exp\left(\textstyle\sum_j(-\,\sigma_2(\nu,j)[\mathrm{X}]_2 l_2)\right) \tag{2.27}$$

These equations were first derived by Ladenburg and Reiche [27] in 1913.

The Lyman-α line of hydrogen atoms is an overlapping doublet with the two centre wavelengths 121.5668 nm ($^2\mathrm{S}_{1/2} \leftarrow {}^2\mathrm{P}_{3/2}$) and 121.5673 nm ($^2\mathrm{S}_{1/2} \leftarrow {}^2\mathrm{P}_{1/2}$) [28]. With equation (2.27), the total emission function of an H ARAS lamp as a function of $\gamma(\nu)$ (2.22) is given by

$$E_2(\gamma) = \left(1 - \exp\left(-\left(\sigma_{01}[\mathrm{H}]_1 l_1 \exp\left(-\left(\frac{\gamma}{\alpha_1}\right)^2\right) + 2\sigma_{01}[\mathrm{H}]_1 l_1 \exp\left(-\left(\frac{\gamma + \Delta\gamma}{\alpha_1}\right)^2\right)\right)\right)\right) \cdot$$

$$\left(\exp\left(-\sigma_{02}[\mathrm{H}]_2 l_2 \exp\left(-\gamma^2\right) + 2\sigma_{02}[\mathrm{H}]_2 l_2 \exp\left(-\,(\gamma + \Delta\gamma)^2\right)\right)\right). \tag{2.28}$$

The total emission of a H ARAS lamp for different concentrations of H atoms in the reversal layer ($[\mathrm{H}]_2 = 0\ \mathrm{cm}^{-3}$ to $[\mathrm{H}]_2 = [\mathrm{H}]_1 = 5 \times 10^{11}\ \mathrm{cm}^{-3}$) is illustrated in figure 2.4. With increasing concentration $[\mathrm{H}]_2$, self-reversal of the line becomes more pronounced. However, also for small concentrations, effects on the line shape are noticeable.

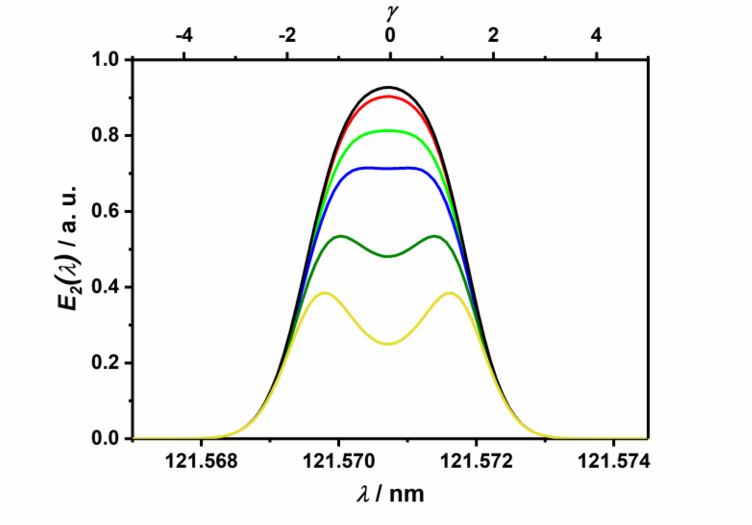

Figure 2.4: Total emittance calculated for the H Lyman-α line by equation (2.28). Input parameters: l_1 = 3 cm, l_2 = 1.5 cm, T_1 = 300 K, T_2 = 298 K, $[H]_1 = 5 \times 10^{11}$ cm^{-3}, $[H]_2 = 0$ cm^{-3} (black), 1×10^{10} cm^{-3} (red), 5×10^{10} cm^{-3} (green), 1×10^{11} cm^{-3} (blue), 1.25×10^{11} cm^{-3} (dark green), 5×10^{11} cm^{-3} (yellow).

Usually, lamp setups for ARAS experiments are designed to reduce self-absorption effects. This can easily be achieved by low precursor concentrations in the lamp mixtures. Alternatively, the flow direction of the lamp gas through the lamp setup can be varied: If the lamp mixture passes through the microwave discharge from the probe side of the lamp, H atoms between emission zone and probe originate only from diffusion of H atoms from the emission layer. Different lamp designs were also discussed: Myerson and Watt [29] experimented with an ARAS lamp with expansion chamber. Lifshitz et al. [1] omitted the reversal layer by dividing the quartz tube into two parts by an additional optical window (figure 2.5).

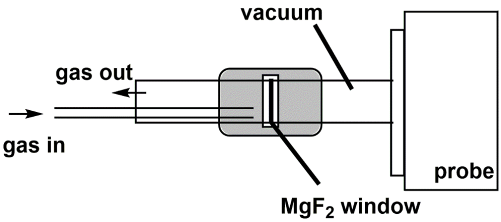

Figure 2.5. Microwave discharge lamp design by Lifshitz et al. [1] to reduce self-absorption.

2.2.2 Detection

The detection unit of an ARAS experiment usually consists of a wavelength selector to isolate the detection wavelength (compare table 2.1), and a photomultiplier tube to record the transmitted intensities. The choice of the devices mainly depends on the detection wavelength, and the space available in the experimental facility.

2.2.2.1 Instruments for the Isolation of Specific Wavelength

Specific wavelengths can be isolated with a monochromator [30]. The incident radiation enters the monochromator through the entrance slit. The light beam passes through a dispersing component (e.g. prism, grating) where the different wavelengths are separated. The spatial orientation of the dispersing element relative to the exit slit determines the wavelength of the monochromatic radiation transmitted through the device. Two lenses or spherical mirrors are used to focus the incoming light onto the dispersing element, and the monochromatic radiation onto the exit slit. Aberrations (e.g. astigmatism, coma) can be reduced by the choice of the optical components (gratings, mirrors, lenses) and the spatial arrangement of these [31-33].

If the utilization of a monochromator is not feasible (e.g. due to space restrictions), optical filters can be an alternative. Commercial filters are categorized either according to the underlying physical processes (e.g. absorption filter, interference filter) or according to their spectral properties (e.g. edge filter, band pass filter) [32]. Edge filters exhibit high transmissions, and a steep edge separating the transmitted and blocked wavelengths. Short pass and long pass filters are distinguished. Band pass filters transmit a restricted range of wavelengths. Their transmission curves are characterized by the peak wavelength, their maximum transmission and the full width at half maximum. They usually show a lower maximum transmission compared to edge filters. Broad band and narrow band filters are distinguished. Alternatively, also gases (molecular or atomic) can used as transmission filters [34]. The absorption spectrum of the filter species determines the application range. Additionally, the reactivity of the filter species must be considered to prevent damage to the experimental setup.

The main difference between the two components, filter and monochromator, lies in the bandwidth of the light transmitted. To obtain unbiased ARAS results, it is important to ensure that only radiation of the detection wavelength of the ARAS target species is transmitted to the detector, if the probe additionally contains other absorbing species. Due to the high sensitivity of ARAS and the often low concentrations in the probe, the interfering absorption processes are mostly resonance absorption processes by other atomic species. The utilization of a monochromator is recommendable. If an ARAS setup is operated with a filter, the filter and the material of the other optical components must be chosen to restrict the wavelength range transmitted as much as possible. Therefore, possibly interfering species have to be identified in the planning of the experiment.

2.2.2.2 Photomultiplier Tubes

Detection of light by photomultiplier tubes is based on the photoelectric effect. After passing the entrance window, the incident radiation causes the emission of photoelectrons from the photocathode. These electrons are accelerated and focussed onto the first dynode of the electron multiplier unit. In this unit, the electron emission of the first dynode is amplified. Electrons emitted by the final dynode of the unit are collected at the anode, and the current is measured. This current is related to the intensity of the incident radiation.

The material of the entrance window and the photocathode mainly determine the spectral response range of the photomultiplier. The entrance window should exhibit a high transmission in the range of the detection wavelength. For the photocathode, materials with a low work function are used. The number of dynodes and their spatial arrangement influence the sensitivity, time resolution and response linearity of the photomultiplier tube.

2.2.3 Calibration

Three principal approaches to calibrate an ARAS experiment are available. In the following, a brief introduction will be given.

Calibration through a well-known reaction system

To calibrate ARAS, a reaction system with a well know mechanism is chosen. Rate coefficients should be known with good precision. ARAS experiments on this system are conducted and the concentration-time profile of the ARAS target species is simulated under the conditions of the experiment. To obtain a calibration curve, simulated concentrations are assigned to measured absorbance values for each point of time during the measurement. Each experiment corresponds to one calibration curve.

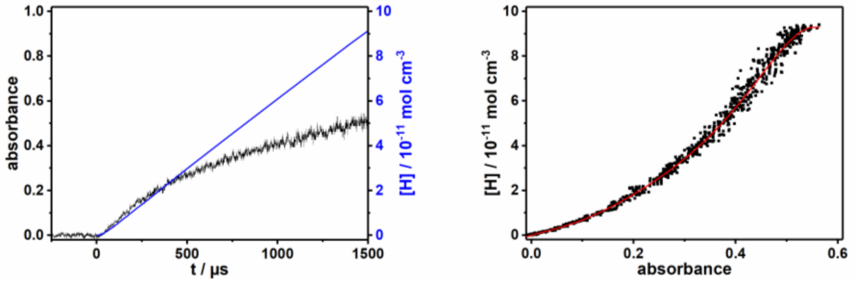

Figure 2.6: Right: Comparison of a measured absorbance-time profile with the simulated concentration-time profile. Left: Resulting calibration curve.

This calibration technique is regularly employed in H ARAS experiments [3, 13, 35]. H ARAS calibration measurements are performed on mixtures of N_2O and H_2.

Table 2.2.: Reaction mechanism for the calibration of H ARAS with N_2O/H_2 mixtures.
Parameterization: $k(T) = A \times (T/\mathrm{K})^n \times \exp(-E_a/RT)$. Units: s^{-1}, kJ, mol^{-1}, cm^3, K.

	reaction	A	n	E_a	ref.
($R_{2.1}$)	$N_2O + M \rightarrow N_2 + O + M$	3.97×10^{14}	0.00	237	[36]
($R_{2.2}$)	$O + H_2 \rightarrow OH + H$	5.11×10^{4}	2.76	26	[37]
($R_{2.3}$)	$H_2 + M \rightarrow H + H + M$	6.02×10^{18}	- 1.10	343	[38]
($R_{2.4}$)	$H + H + M \rightarrow H_2 + M$	6.89×10^{17}	- 1.00	0	[38]
($R_{2.5}$)	$H + OH + M \rightarrow H_2O + M$	8.34×10^{21}	- 2.00	0	[37]
($R_{2.6}$)	$H_2 + OH \rightarrow H_2 + O$	1.02×10^{8}	1.60	14	[37]
($R_{2.7}$)	$N_2O + H \rightarrow N_2 + OH$	2.23×10^{14}	0.00	70	[39]
($R_{2.8}$)	$N_2O + O \rightarrow N_2 + O_2$	1.02×10^{14}	0.00	117	[40]
($R_{2.9}$)	$O + O + M \rightarrow O_2 + M$	1.01×10^{17}	-1.00	0	[41]
($R_{2.10}$)	$OH + OH \rightarrow H_2O + O$	1.50×10^{9}	1.14	0.4	[37]
($R_{2.11}$)	$OH + O \rightarrow O_2 + H$	1.44×10^{13}	0.00	2.9	[37]

The decomposition of N_2O yields N_2 and atomic oxygen ($R_{2.1}$). These oxygen atoms can abstract a hydrogen atom from H_2 forming hydroxyl radicals and hydrogen atoms ($R_{2.2}$). By these two reactions a sufficient amount of atomic hydrogen can be produced, also at lower temperatures. The ratio of N_2O to H_2 in the mixtures determines the temperature range that can be covered in the calibration experiments. Under low temperature conditions, an excess of N_2O should be used. At higher temperatures, mixtures containing a surplus of H_2 are better suited. For temperatures above 2000 K, calibration with mixtures containing only H_2 is feasible.

The main disadvantage of this calibration method lies in the sensitivity of calibration curves to the rate coefficients in the calibration mechanism. For H ARAS calibration, this problem is reduced by the number of reactions influencing H atom concentrations. However, if only one or two reactions determine the absolute concentrations of the ARAS target species in the simulation, uncertainties in the corresponding rate coefficients directly translate into errors in the calibration curve.

Calibration by maximum absorbance measurements

If a molecule completely decomposes, and secondary reactions are negligible, concentrations of products at long reaction times are equivalent to the initial concentration of the reactant. For calibration, a reactant is chosen, which yields the ARAS target species in one reaction step. Experiments on mixtures of this reactant are conducted in a temperature range, in which a complete dissociation of the reactant is highly probable. Measured absorbance-time profiles will converge to a constant absorbance value for long reaction times. This constant absorbance value corresponds to a concentration of the ARAS target species equal to the initial concentration of the reactant. To obtain a calibration curve, measurements on different initial reactant concentrations are evaluated. Each measurement translates into one point of the calibration curve.

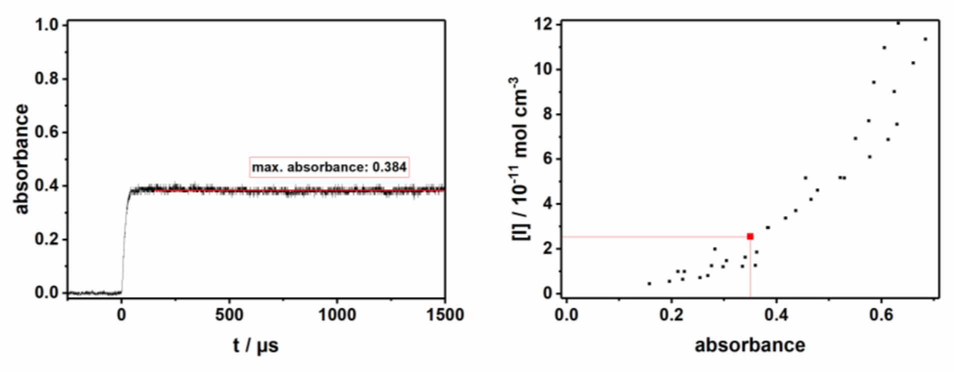

Figure 2.7: Right: Determination of the maximal absorbance. Left: Calibration curve (red square: experiment).

The main disadvantage of this calibration technique lies in the number of experiments necessary to generate one calibration curve. Due to the fairly poor reproducibility of shock tube measurements it is difficult to obtain calibration curves for specific experimental conditions, for instance at a specific pressure. To cover the entire range of absorbances values, experiments on different mixtures with distinct reactant concentrations are required. Very low reactant concentrations are reached by stepwise dilution of higher concentrated mixtures. With each dilution step, the error in the absolute concentration of the reactant increases. Thus, also the error in the calibration curve increases for low absorbance values.

Calibration through line absorption theory calculations

An introduction to line absorption theory for ARAS was given in section 2.2.1. For the computation of calibration curves, the two layer model is extended by a third, purely absorbing layer, corresponding to the probe.

Absorption by this layer, denoted with the index three, can be described by

$$A_3(v) = \exp(-\,\sigma_3(v)\;[\mathrm{X}]_3\;l_3)\,. \tag{2.29}$$

For an overlapping multiplet, equation (2.29) changes to

$$A_3(v) = \exp\left(\textstyle\sum_j(-\,\sigma_3(v,j)\;[\mathrm{X}]_3\;l_3)\right). \tag{2.30}$$

With these equations, the transmission through the probe layer Tr can be calculated as

$$Tr \;=\; \frac{I}{I_0} = \frac{\int_{-\infty}^{\infty} E_2(v)\,A_3(v)\,\mathrm{d}v}{\int_{-\infty}^{\infty} A_3(v)\,\mathrm{d}v}\,. \tag{2.31}$$

The absorbance by a probe is related to its transmittance by

$$Abs = -\log\,(Tr). \tag{2.32}$$

By varying the concentration of the absorber in the probe ($[\mathrm{X}]_3$) in equations (2.29) or (2.30), calibration curves for a specific temperature T_3 can be calculated with equations (2.31) and (2.32). Thereby, calibration curves for the entire range of absorbance values can be obtained quite easily and without the dependence on specific rate coefficients of various reactions. However, the determination of accurate lamp parameters is crucial and experimentally challenging. Whilst the experimental conditions (temperature T_3 and length of optical pathway l_3) are in most cases well known, lamp parameters, especially concentrations and temperatures, cannot be directly measured. As an additional parameter, the fraction of non-resonant radiation emitted by the ARAS lamp has to be known. As calculations are based on a simplified model, daily fluctuations in lamp intensities are not accounted for.

2.3 Introduction to Reaction Kinetics

2.3.1 Reaction Mechanisms

To describe the temporal development of a reacting system (e.g. the variation of species concentrations), reaction mechanisms are developed. Depending on the complexity of the system (number of reactants, reactivity of reactants, reaction conditions) and the properties to be described (concentrations of one species, concentrations of more species), the corresponding mechanisms can consist of only a few up to several thousand elementary reactions. An elementary reaction proceeds in only one step. Its molecularity equals the order of the reaction [42].

In general, the chemical equation of an (elementary) reaction can be expressed as [43]

$$\sum_{i=1}^{n} v_i^{\mathrm{e}} A_i \xrightarrow{k} \sum_{i=1}^{n} v_i^{\mathrm{p}} A_i \,. \tag{2.33}$$

A_i denotes the species i in the system. v_i represents the stoichiometric coefficient for species A_i as educt (e) or product (p). k is the rate coefficient for the reaction.

From equation (2.33), the differential rate expression for the concentration of species j (c_j) can be derived to

$$\frac{\mathrm{d}c_j}{\mathrm{d}t} = k\left(v_j^{\mathrm{p}} - v_j^{\mathrm{e}}\right) \prod_{i=1}^{n} c_i^{v_i^{\mathrm{e}}} \,. \tag{2.34}$$

For a mechanism of r reactions with the rate coefficients k_l ($l = 1 \dots r$), the total rate of formation of a species i is given by

$$\frac{\mathrm{d}c_j}{\mathrm{d}t} = \sum_{l=1}^{r} k_l\left(v_{j,l}^{\mathrm{p}} - v_{j,l}^{\mathrm{e}}\right) \prod_{i=1}^{n} c_i^{v_{i,l}^{\mathrm{e}}} \,. \tag{2.35}$$

To predict the temporal development of the concentrations of different species in a reaction system, the differential rate equations (2.35) have to be solved. For the integration of these coupled differential equations, different program packages are available (e.g. OpenSMOKE [44, 45]). The results mainly depend on the values for the rate coefficients of the different reactions. To assess which reaction has the maximum impact on the concentration of a species or by which reaction path a certain species is formed, different methods are available [43, 46].

2.3.2 Analysis of Complex Reaction Mechanisms

2.3.2.1 Sensitivity Analysis

Sensitivity analysis is a tool to identify the most important reaction steps in the formation and consumption of one species in a complex mechanism. In this context, the most important reaction is not necessarily the reaction which dominates the production or consumption of a species, but the one for which a small change in the rate coefficient implies the most radical change in concentration. Hence, sensitivity analysis singles out rate determining steps in a mechanism

In practice, sensitivity coefficients are calculated. These are defined as:

$$S_{i,r} = \frac{\partial c_i}{\partial k_i}. \tag{2.36}$$

$S_{i,r}$ denotes the absolute sensitivity coefficient for the concentration of species i (c_i) in relation to reaction r with the corresponding rate coefficient k_r. More frequently, relative sensitivity coefficients are employed. These can be calculated as:

$$S_{i,r}^{\mathrm{rel}} = \frac{\partial \ln(c_i)}{\partial \ln(k_r)} = \frac{k_r}{c_i} \cdot \frac{\partial c_i}{\partial k_r}. \tag{2.37}$$

The larger the sensitivity coefficient, the higher is the influence of a distortion in the related rate coefficient on the concentration. For sensitivity coefficients with positive sign, the change in the rate coefficient is positively correlated to the change in concentration. In the case of negative signs, the two numbers are negatively correlated, meaning an increase in the rate parameters leads to a decrease in concentration.

In general, local and global sensitivities are distinguished. For a time-dependent system, a local sensitivity coefficient at time t is the sensitivity coefficient calculated with the values at this time. On the contrary, global sensitivity coefficients are the result of integration over the complete time interval simulated.

2.3.2.2 Reaction Flux Analysis

In contrast to a sensitivity analysis, where the impact of change of rate coefficients is evaluated, a reaction flux analysis describes how much of one species is directly formed or consumed in a specific reaction. Commonly, a reaction flux analysis is performed for an atomic species. The redistribution of this species throughout the reaction is than followed.

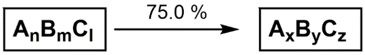

Figure 2.8: Reaction flux diagram.

Reaction flux analysis results are usually visualized as reaction flux diagrams. A schematic example is displayed in figure 2.8. Assuming that this example shows the result of a reaction flux analysis regarding the atomic species B, two cases need to be distinguished for the interpretation of the diagram:

- Reaction flux analysis for the consumption of '$A_nB_mC_l$':
  75 % of the atoms B in the reactant are found in the product.
- Reaction flux analysis for the production of '$A_xB_yC_z$':
  75 % of the atoms B in the product originate from the reactant.

Thus, in the interpretation of reaction flux diagrams, the stoichiometry of reactants and products needs to be considered. All reaction channels originating from, or resulting in, a species have to sum up to 100 %.

2.3.3 Temperature and Pressure Dependence of Rate Coefficients

Rate coefficients usually vary with temperature. To adequately describe a reaction system the temperature dependence of the rate coefficients has to be parameterized. In most cases an Arrhenius parameterization (2.38) is sufficient:

$$k(T) = A \exp\left(- \frac{E_\mathrm{a}}{\mathrm{R}T}\right). \tag{2.38}$$

The rate coefficient k is given as a function of the Arrhenius parameter A and the activation energy of the reaction E_a. This equation was first found by S. Arrhenius [47] in 1889.

If wide temperature ranges are covered, deviations from the simple Arrhenius form (2.38) can be noted. In such cases, an extended Arrhenius expression [48] is employed:

$$k(T) = A' \, T^n \exp\left(- \frac{E_\mathrm{a}'}{\mathrm{R}T}\right). \tag{2.39}$$

Total rate coefficients of unimolecular reactions often additionally vary with pressure. A first model to describe the pressure dependence of unimolecular reactions was developed by Lindemann [49, 50]. It was further refined by Hinshelwood [51], Rice, Ramsperger [52] and Kassel

[53] and Rice, Ramsperger, Kassel and Marcus [54, 55]. According to Lindemann, a unimolecular reaction

$$A \xrightarrow{k_{uni}} P \tag{R2.1}$$

is better represented by

$$A + M \xrightarrow{k_1} A^* + M, \tag{R2.2}$$

$$A^* + M \xrightarrow{k_{-1}} A + M, \tag{R2.3}$$

$$A^* \xrightarrow{k_2} P. \tag{R2.4}$$

The reactant A is activated through collision with the bath gas M. The activated species A^* can be either deactivated (R2.3) or react to form the product(s) P (R2.4).

k_{uni} can be expressed as a function of the rate coefficients k_1, k_{-1} and k_2 and the bath gas concentration [M] which is proportional to the pressure in the system:

$$k_{uni} = \frac{k_1\, k_2\, [M]}{k_{-1}\, [M] + k_2}. \tag{2.40}$$

At low pressures, k_{uni} is directly proportional to the concentration of the bath gas [M]. At high pressures an upper boundary value, the high-pressure rate coefficient, is reached.

2.3.4 Experimental Determination of Rate Coefficients

In general, rate coefficients can be determined either experimentally (direct or indirect) or calculated with quantum chemical methods. The choice of the method mainly depends on the reaction to be described. In the optimal case, not only one single method is employed, but a combination of both experimental and theoretic methods is chosen. In the following, two experimental approaches will be discussed.

Determination of rate coefficients for first-order decomposition reactions from concentration-time profiles

If a chemical reaction can be isolated experimentally, meaning it can be assured that only the desired reaction or a small set of reactions influences the experimental results, rate coefficients can be determined directly from the experimental data. This is especially true if concentration-time profiles are recorded in the experiment conducted. For a simple first order reaction

$$\mathrm{A} \xrightarrow{k} \mathrm{P}, \tag{R2.1}$$

the corresponding differential rate law is given by

$$-\frac{\mathrm{d[A]}}{\mathrm{d}t} = \frac{\mathrm{d[P]}}{\mathrm{d}t} = k \cdot \mathrm{[A]}. \tag{2.41}$$

Dividing equation (2.41) by the initial concentration of the reactant and evaluating the equation for short reaction times leads to the following expression for the rate coefficient k under the conditions (temperature, pressure) of the experiment:

$$k = \frac{1}{\mathrm{[A]_0}} \cdot \left.\frac{\mathrm{d[P]}}{\mathrm{d}t}\right|_{t \to 0} \tag{2.42}$$

The initial slope ($\mathrm{d[P]}/\mathrm{d}t$) can be determined directly from measured concentration-time profiles. Evaluating equation (2.42) for different experiments with different initial conditions provides the data necessary for the deduction of an Arrhenius parameterization of the rate coefficient, and gives information about a possible pressure dependence.

The main challenge is to ensure that only one isolated reaction influences the measured concentration-time profiles. Experiments must be performed on very dilute reactant mixtures, which restricts the available detection methods. At higher concentrations, the influence of bimolecular (initiation) reactions increases as well as the number of influencing reactions. Furthermore, the experimental conditions must be chosen so that the reaction process can be timely resolved by the detection method. This mainly defines the temperature range for the determined rate coefficients. Errors in the concentrations determined in the experiment directly translate into errors in the rate coefficient.

Determination of rate coefficients by simulation of a (complex) reaction mechanism

If it is not possible to isolate a single reaction or to obtain uniform experimental conditions, rate coefficients cannot be determined directly. In these cases, simulations must be employed. A mechanism is chosen and, by variation of a (small) number of rate coefficients, adjusted to best describe the experimental results. As before, by repeating the procedure for different initial reaction conditions, Arrhenius parameterization and pressure dependence can be deduced.

Only rate coefficients of reactions which exhibit a high sensitivity towards the concentration of the measured species can be determined this way. The quality of the obtained rate coefficients strongly depends on the quality of the mechanism utilized and the rate coefficients implemented therein. Especially missing reactions can falsify the obtained coefficients.

3 Experiment

3.1 Experimental Setup

3.1.1 Shock Tube

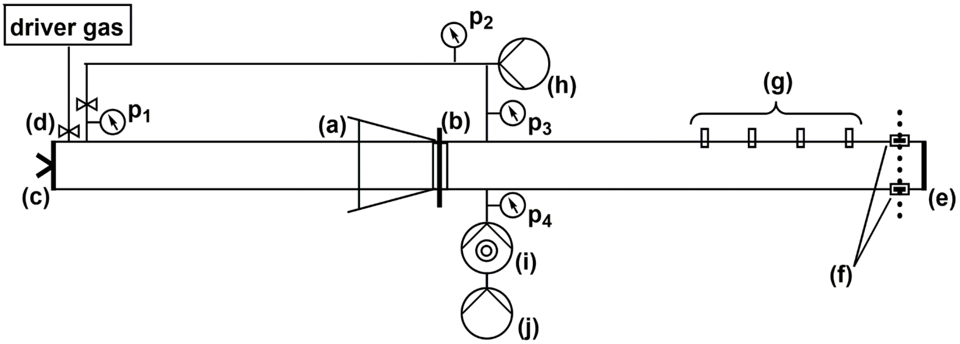

Figure 3.1: The shock tube. For detailed explanations see text.

All experiments were conducted in a stainless steel shock tube with polished inner walls. It consists of a 4.25 m long low-pressure and a 3.05 m long high-pressure section. The low-pressure section has an inner diameter of 10.0 cm and a wall thickness of 1.00 cm, whilst the high-pressure section has an inner diameter of 9.85 cm and a wall thickness of 1.30 cm. Both parts are connected by a quick-lock (a). At this position, a diaphragm (b) can be clamped.

On its other end, the high-pressure section is sealed with an end flange (c). Close to the end flange, the inlet for the driver gas is mounted. The driver gas is introduced into the shock tube via an electropneumatic valve (d) (Co.: SMC, NVZ110), which is operated with compressed air.

The low-pressure section is also sealed with an end flange (e). 5.3 cm from this end flange, four mountings for optical windows (f) are positioned. These define two perpendicular optical detection axes.

To measure the shock wave velocity, four piezo resistant pressure transducers (g) (Co.: Kistler, 603B) are mounted into the wall of the low-pressure section starting 15.8 cm from the end flange. The distance between two adjacent pressure transducers accounts to 40.0 cm.

The entire shock tube can be evacuated by a rotary vane pump (h) (Co.: Adixen, Pascal 2021SD) mounted to the connection of low- and high-pressure section. To reach pressures below 8×10^{-3} mbar, a turbomolecular pump (i) (Co.: Pfeiffer, TMU 260) with a rotary vane backing pump (j) (Co.: Pfeiffer Balzers, DUO 004B) is used. Pressures in the shock tube are monitored by four pressure gauges ((p_1) Co.: MKS, 122A; (p_2) Co.: Balzers, TPR020; (p_3) Co.: MKS, Baratron 626AX13MDE; (p_4) Co.: Pfeiffer, IKR 550).

3.1.2 ARAS Setup

Only the original horizontal ARAS setup will be described here. The second, vertically mounted, ARAS system will be discussed in chapter 4.3.1 as a part of the new dual ARAS experiment.

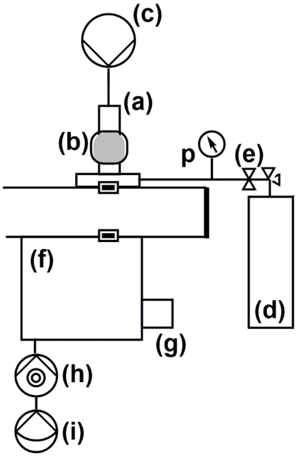

Figure 3.2: The horizontal ARAS setup. For detailed explanations see text.

An ARAS setup in general consists of two parts: a light source and a detection unit.

The light source is a 15 cm long quartz tube (a) (Co.: Aachener Quartzglas, inner diameter: 10 mm; wall thickness: 1.5 mm), partly enclosed by an Evenson cavity (b) which is connected to a microwave generator (Co.: Muegge, MW-GPR YJ 1511-300-01). In this cavity, the microwave discharge is generated and stabilized. To prevent melting of the quartz tube, cavity and tube are cooled by a compressed air flow. One end of the quartz tube is connected to a rotary vane pump (c) (Co.: Leybold, Trivac D4B). The other end is embedded into a stainless steel flange to mount the ARAS lamp to the shock tube. To shield the shock tube from radiation, a shutter is integrated into the flange.

The lamp mixture is stored in a mixture tank (d) which is connected to the stainless steel flange of the ARAS lamp. A metering valve (e) is used to set the gas flow through the lamp system. This flow is characterized by the pressure inside the lamp system which is measured by a pressure gauge ((p) Co.: MKS, Baratron 626BX12MDE). For H ARAS and Cl ARAS experiments, an inner lamp pressure of ~ 15 mbar is chosen. It is decreased to ~ 10 mbar for I ARAS experiments.

The detection unit consists of a monochromator (f) (Co.: Acton Research Cooperation, VM504) and a photomultiplier tube (g) (Co.: Hamamatsu, R6349). The monochromator is directly mounted to the shock tube. It is constantly evacuated by a turbomolecular pump (h) (Co.: Pfeiffer, HiPace 80) with a diaphragm backing pump (i) (Co.: Pfeiffer, MVP015-4). The photomultiplier tube is operated with a high voltage supply (Co.: Stanford Research Systems, PS325) and connected to an oscilloscope (Co.: Tektronix, TDS5104B) for data acquisition.

To increase the time resolution of the ARAS experiments, two slits (width: 1 mm) are inserted into the system. These are positioned in front of the optical windows of the shock tube.

3.1.3 Mixing System

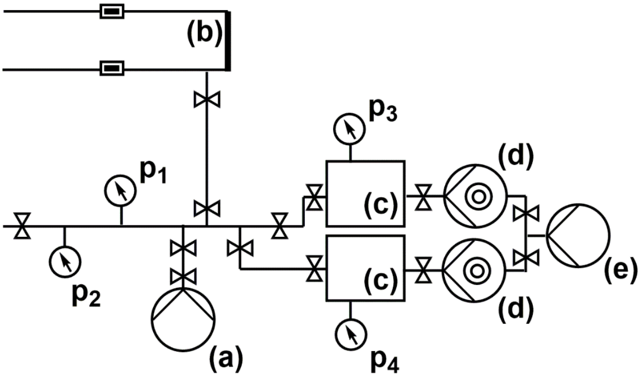

Figure 3.3: The gsa mixing system. For detailed explanations see text.

The gas mixing system consists of a stainless steel tube with seven KF flanges. It can be evacuated by a rotary vane pump (a) (Co.: Adixen, Pascal 2021SD). Two pressure gauges (p_1, p_2) (Co.: MKS, Baratron 626AX02MDE (max. 2 mbar) and Baratron 626AX13MDE (max 1000 mbar)) are utilized to record the pressure inside the mixing system. Via another flange, the mixing system is connected to the low-pressure section of the shock tube (b). Through this connection, gases can be let into the shock tube. By the remaining three flanges, mixing and lamp tanks, flasks, and gas cylinders can be connected to the mixing system.

For mixture preparation and storage, three 100 l vessels are available. Two of them (c) are constantly coupled to the mixing system. These are both equipped with a turbomolecular pump (d) (Co.: Pfeiffer, TMU261; Co.: BOC Edwards, EXT255H) and a pressure gauge (p_3, p_4) (Co.: Balzers, PKR251). The two turbomolecular pumps are connected to one shared rotary vane backing pump (e) (Co.: Edwards, RV8).

3.2 Experimental Procedure

Prior to each experiment, the entire shock tube was evacuated to pressures below 8×10^{-6} mbar. To avoid any interaction of the probe with radiation emitted by the ARAS lamp (e.g. absorption, photoinduced reactions) before the experiment, the ARAS lamp shutters were closed throughout the preparation procedure. They were opened short before the start of a measurement.

The preparation of an experiment began with disconnecting the high- and low-pressure section of the shock tube. After turning on the ARAS lamps, the probe gas was introduced into the low-pressure section. A measurement was started by handling the foot pedal which operates the electropneumatic valve. The driver gas H_2 was introduced into the high-pressure section of the shock tube until the rupture of the diaphragm. Registration of a pressure rise at the first pressure transducer triggered the data acquisition at the oscilloscope. Data points were recorded for 2000 µs.

After an experiment, the valve separating high- and low-pressure section was opened again. The shock tube was evacuated to pressures around 5×10^{-1} bar. Afterwards, it was filled with nitrogen and opened to remove the rest of the diaphragm. Parts of the diaphragm which were carried into the shock tube, were removed by a strong flow of nitrogen. After inserting a new diaphragm at the quick-lock, the shock tube was evacuated again.

To ensure a contamination-free setup, the first experiment each day was performed on pure argon as probe gas. If an absorbance was recorded with any of the detection setups, another measurement on argon was conducted. When the neatness of the shock tube was proven, calibration experiments were performed. These had to be repeated every day to account for intensity fluctuations of the ARAS lamps.

3.3 Mixtures

Mixtures were prepared in the mixing system (section 3.1.3) by the partial pressure method. Components were introduced into the tanks in order of increasing ratio in the mixture. All liquid chemicals were degassed in three pump-freeze circles prior to use.

Lamp mixtures contained 1 % precursor in helium. That is H_2 for H ARAS, methyl iodide (CH_3I) for I ARAS and chlorine (Cl_2) for Cl ARAS. Calibration mixtures for H ARAS experiments consisted of N_2O and H_2 in a ratio of one to ten in argon. Mole fractions in these mixtures usually ranged between 200 and 300 ppm N_2O and 2000 and 3000 ppm H_2. The composition of all other mixtures was varied during the experiments and will be stated in the corresponding sections.

A complete list of chemicals used, including their purity and manufacturer can be found in appendix A.1.

3.4 Software

For the calculation of the experimental conditions behind reflected shock waves based on the shock wave equations (compare section 2.1) Mathcad 2000 and Mathcad Prime 2.0 (Co.: PTC / Mathsoft) were used. Data was processed and evaluated with Origin (Co.: OriginLab Corporation, Versions 8 and 2017).

ARAS calibration curves were deduced with the LabView program ‘ARAS-Kalib’ written by T. Bentz [56]. It was slightly modified to process the output data of OpenSmoke simulations.

All simulations were performed with the program package OpenSmoke Suite++ [45]. The experiment was represented as a batch reactor under non-isothermal constant volume conditions. To solve the coupled differential equations, the implemented ODE-solver ‘OpenSMOKE’ [45] was used.

3.5 Errors and Uncertainties

The main source of errors in the experimental results is the restricted precision of the instruments utilized. Errors in the experimental conditions behind reflected shock waves are mainly due to uncertainties in the measured shock wave velocity. The precision of the calculated temperatures was estimated to ± 10 K. For the calculated pressures, uncertainties amount to circa ± 0.1 bar.

The restricted precision of the pressure gauges leads to errors in the mixing ratios of probe and calibration mixtures. These directly translate into uncertainties in reactant concentrations in the experiment as calculated by the shock wave equations. Very dilute mixtures are prepared by dilution of higher concentrated ones. With each dilution step, the error in the concentration increases. The relative error for the calculated initial concentrations in the experiments was estimated to ± 10 %.

For rate coefficients directly determined from the initial slope of recorded concentration-time profiles, errors were estimated to ± 30 %. These include uncertainties in the concentration measurements due to calibration, signal-to-noise ratio of the measurement and fluctuations in lamp intensities. Differences originating from the choice of the initial time interval for the determination of the initial slope are also included in this error estimate. This was shown in a trial with students of the 2016 summer term reaction kinetics course. The participants were asked to mark the initial part in ten H atom concentrations-time profiles from H ARAS experiments. From the marked intervals, rate coefficients were calculated.

If rate coefficients were determined through modelling of a reaction mechanism, errors were estimated to ± 50 % to additionally account for uncertainties in rate coefficients of other reactions, and for possibly missing reactions.

4 Instrumental Modifications

4.1 Overview

Throughout this work, different instrumental modifications were developed and tested. Main objective was the implementation of a second ARAS setup into the existing shock tube/ARAS experiment. The second ARAS unit was installed onto the second available optical pathway, perpendicular to the original ARAS system. However, as the detection axes do not exhibit exactly the same conditions, some changes were necessary in the adoption of the ARAS setup. In the process, a filter flange was constructed which can be employed either as a molecular or as an atom filter.

In another series of experiments a different membrane system was tested. Aim was an improvement of the reproducibility of the experiments. An inlet for the low-pressure section of the shock tube has been developed by which a mandrel can be positioned close to the diaphragm. The rupture of the diaphragm should then be determined by the position of the mandrel, rather than by the pressure difference alone. Thereby, the spontaneous and ‘uncontrolled’ rupture of the diaphragm should be avoided.

Both instrumental modifications will be described in detail in this chapter. In the first section, the alternative membrane system will be presented and the reproducibility of shock tube measurements will be discussed. The dual ARAS setup will be introduced in the second part. An introduction to the oxygen filter system (one application of the filter flange) will be given. Interchangeability of ARAS for different species will be discussed. The second utilization of the filter flange is the topic of section 4.4. Possible applications of this atom filter will be considered.

This work has been partly performed as a student work supervised by the author. L. Golka participated in the trial of the atomic filter flange during her seven week practical lab course (‘Vertieferpraktikum’). M. Kraft conducted the test measurements of the new membrane system in his bachelor thesis. F. Poschen took part in the trial of a vertical Cl ARAS setup during his seven week practical lab course (‘Vertieferpraktikum’).

4.2 Test of an Alternative Membrane System

A main disadvantage of the traditional membrane shock tube is the restricted reproducibility of experimental conditions behind the incident or reflected shock wave. This is mainly due to the spontaneous rupture of the diaphragm once the pressure difference between high- and low-pressure section is high enough. Slight variations in the condition of the aluminium foil (e.g. unwanted small bents) influence the tear properties of the material. The problem can be reduced, if the rupture of the diaphragm is introduced manually. If a cutter is placed into the low-pressure section at a given distance from the diaphragm, the contact of the strained membrane with the cutter induces the rupture of the diaphragm. In this case, the experimental conditions should be mainly determined by the position of the cutter and the pressure in the high-pressure section.

In this work, a cutter system was developed in analogy to a setup utilized in the shock tube facility at the Clean Combustion Research Centre at KAUST [57]. It was tested with polycarbonate sheets (Co.: coloprint tech-films, Makrofol DE 1-1, thickness: 175 µm and 250 µm) and aluminium foil (Co.: Alfol, 99.9 % Al, thickness: 80 µm and 60 µm) as membranes.

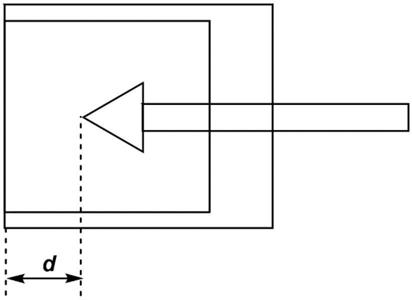

Figure 4.1: The currer system.

The cutter setup consists of an inlet which can be positioned into the low-pressure section of the shock tube. It is crafted out of an 8.00 cm long hollow messing cylinder with an outer diameter of 9.98 cm and a wall thickness of 0.98 cm. In the centre of this cylinder, the cutter can be fixed in a thread by a lock nut. Three thin messing struts hold the thread in the centre of the cylinder. A threaded rod with a four-sided pyramidal head is used as cutter. To ensure a cutting of the membrane, a blunt tip is utilized. A sharp tip would result in a hole in the diaphragm and the pressure in the two shock tube sections would equalize without generation of a shock wave. The distance *d* characterises the position of the cutter relative to the membrane.

Test measurements with polycarbonate sheets were performed on pure argon as probe gas. In a small number of high-temperature H ARAS experiments, no absorbance due to the presence of H atoms was recorded. This indicates, that no or only negligible quantities of hydrocarbons or other hydrogen containing substances are outgassed from the polycarbonate sheets even under high vacuum conditions.

Temperatures behind the reflected shock wave as a function of the initial pressure in the low-pressure section for different positions of the cutter are displayed in figure 4.2. All experiments were performed with 175 µm thick polycarbonate sheets.

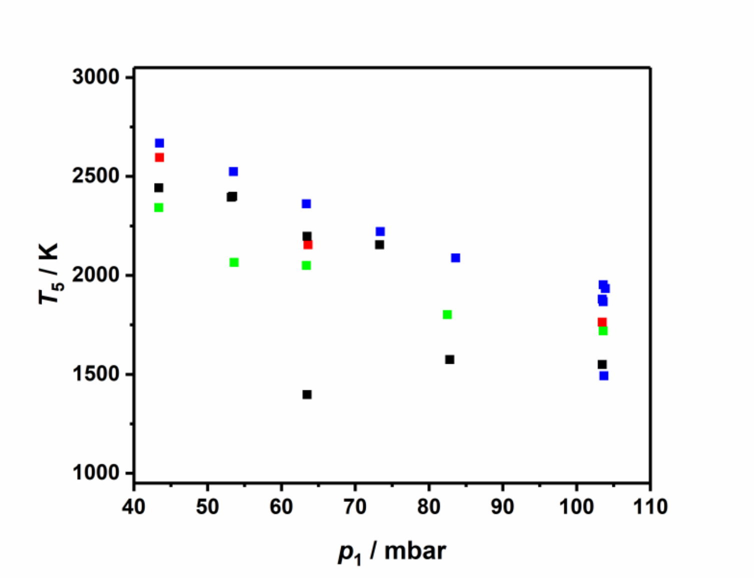

Figure 4.2: Temperature (T_5) behind the reflected shock wave for different initial pressures (p_1) in the low-pressure sections and different cutter positions *d*: black: 4.1 mm; green: 5.2 mm; red: 6.1 mm; blue: 7.0 mm.

With increasing initial pressure, the temperatures behind the reflected shock wave decreases. Apparently, the greater the distance between cutter and membrane, the higher the temperature behind the reflected shock. For a greater distance d, the generation of a shock wave requires a stronger straining of the membrane. Therefore, higher pressures of driver gas in the high-pressure section are necessary. In accordance with equation (2.18), this results in a higher pressure behind the reflected shock wave and thus a higher temperature.

This is supported by figure 4.3. The initial pressures of driver gas in the high-pressure section were calculated from the initial pressures in the low-pressure section, and measured shock wave velocities by equation (2.19). If the rupture of the diaphragm was mainly determined by the position of the cutter, the inlet pressure in the high-pressure section should not change much for small changes in the pressure in the low-pressure section. The results displayed in figure 4.3 indicate, that this is not the case for the experiments performed in this work. The greater the distance d, the more pronounced are the differences in the initial pressure in the high-pressure section. Thus, the destruction of the diaphragm is most probably dominated by the spontaneous rupture of the membrane. This could change if thinner polycarbonate sheets were used as membranes. The higher flexibility of thinner sheets should reduce pressures necessary to obtain a certain curvature of the membranes. In consequence, also the pressure differences should be reduced.

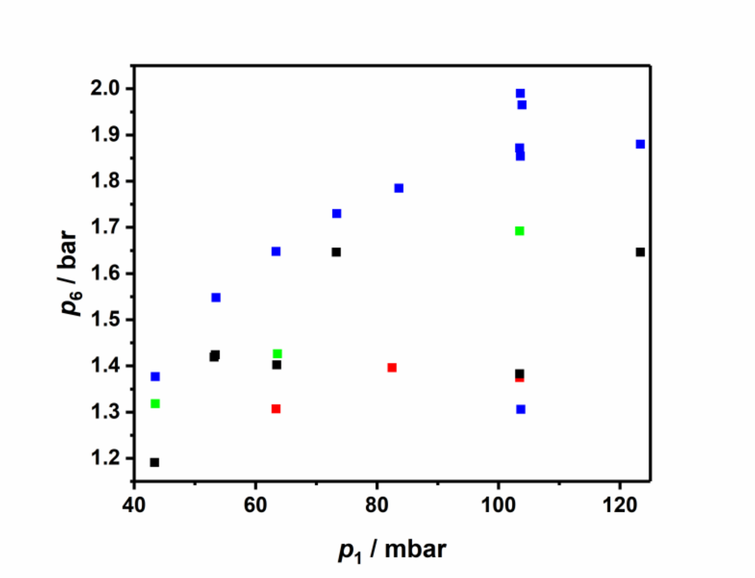

Figure 4.3: Initial pressures in the high-pressure section for the experiments depicted in figure 4.2 calculated with equation (2.19). Different cutter positions *d*: black: 4.1 mm; green: 5.2 mm; red: 6.1 mm; blue: 7.0 mm.

Plastic sheets with a thickness of 250 µm proved too thick for practical applications. Pressures and temperatures behind the reflected shock wave ranged between 2.0 and 4.2 bar and 2100 and 3100 K respectively (inlet pressure low pressure section: 40.0 to 75.0 mbar). The position of the cutter was varied between 4.1 and 5.2 cm. However, of the 50 experiments conducted, only in 25 a shock wave was generated. In most of the other experiments, the plastic sheets did not rupture. This was mainly due to the thickness and mechanical stiffness of the material.

No significant increase in the reproducibility of the shock wave experiments was obtained with the new membrane system. However, due to the manual cutting, the uncontrolled splintering of the diaphragms was prevented. This is not extremely important for the shock tube/ARAS setup. However, at the second shock tube of our shock tube facility, it could be a significant improvement. This second shock tube is coupled to a TOF-MS as detection unit. The sampling occurs via a cone with a small pinhole (diameter 60 µm) in the endplate of the low-pressure section. Aluminium splinters can lead to a blocking of the sampling system.

In a few experiments, also a combination of aluminium foil with the cutter system was tested. As for the plastic sheets, the reproducibility of the experimental conditions was not improved. However, also in this case the uncontrolled splintering of the membranes was avoided.

4.3 The Dual ARAS Experiment

4.3.1 The Second ARAS Setup

The second ARAS setup is mounted perpendicular to the already existing horizontal ARAS unit. Thereby, the second optical detection axis of the shock tube is used. Due to its spatial orientation, it will be denoted vertical ARAS to distinguish it from the already present horizontal one.

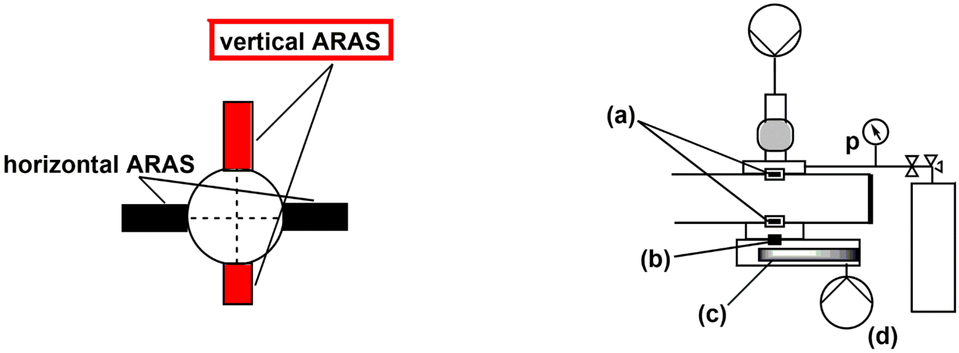

Figure 4.4: Orientation of the two ARAS setups (left) and the design of the vertical ARAS setup (right). For detailed explanations see text.

Like the horizontal ARAS unit described in section 3.1.2, it consists of a light source and a detection setup. The light source is installed on top of the shock tube over the optical axis. Its design resembles the one of the horizontal ARAS light source. Only the microwave generator (Co.: MUEGGE, MG0300D-211TC) and the rotary vane pump (Co.: Pfeiffer, DUO 005M) differ.

As detection unit, a photomultiplier (c) (Co.: Hamamatsu, R1259) in a stainless steel case is directly mounted onto the other side of the optical axis. A rotary vane pump (d) (Co.: Leybold, TRIVAC) is utilized to evacuate the photomultiplier case. Due to the very restricted space available, a monochromator, as in the horizontal ARAS detection unit, cannot be used. Between the optical window and the photomultiplier, an optical filter (b) can be placed as alternative for the monochromator (see discussion section 2.2.2.1).

To operate the vertical ARAS as H ARAS, a vacuum UV narrow band pass filter with a centre wavelength of 121.6 nm (Co.: Pelham Research, 122-NB, peak wavelength: 122 +/- 2.5 nm, peak transmission: 15 %, FWHM: 20 nm) was chosen. In figure 4.5 the transmission spectrum of the filter is compared to a representative emission spectrum of the H ARAS lamp (operating conditions: mixture: 1 % H_2 in He; pressure: ~ 15 mbar). In the spectrum, the atomic emission line of hydrogen (121.6 nm) can be clearly identified.

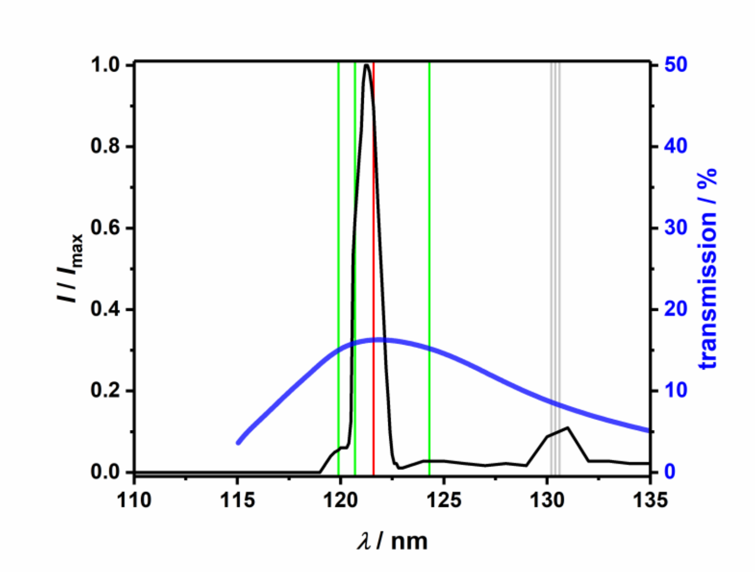

Figure 4.5: H ARAS lamp emission spectrum (1 % H_2 in He, p_{lamp} ~ 15 mbar) and selected atomic emission lines (red: hydrogen; green: nitrogen; grey: oxygen) [28]. Blue: transmission spectrum of the narrow band pass filter (Co.: Pelham Research, 122-NB).

Additional emission lines can be assigned to transitions of oxygen and nitrogen atoms. These are most probably formed from impurities in the gases used for mixture preparation. A list of the identified emission lines and the corresponding atomic transitions can be found in appendix A.2. All emission lines will be transmitted through the optical filter (compare figure 4.5).

H ARAS is calibrated by measurements on mixtures of N_2O and H_2 (see section 2.2.3). The associated mechanism (table 2.2) predicts the formation of oxygen atoms as an intermediate species. It is likely that the oxygen atomic emission lines at 130.2 to 130.6 nm will be absorbed by the atomic oxygen generated in the reaction system. In consequence, a higher total absorbance would be recorded in the calibration experiments. The resulting calibration curves would be flatter, and the actual H atom concentrations in experiments would be underpredicted. Nitrogen atoms are not generated in the system. To suppress the effect of non-hydrogen absorption, all other emission lines in the lamp spectrum have to be omitted.

4.3.2 The Oxygen Filter

For the isolation of the Lyman-α line, an oxygen filter is often used (e.g. [13, 58]). The absorption coefficient of molecular oxygen at 121.6 nm is relatively small and increases significantly to slightly smaller and slightly larger wavelengths (compare figure 4.6).

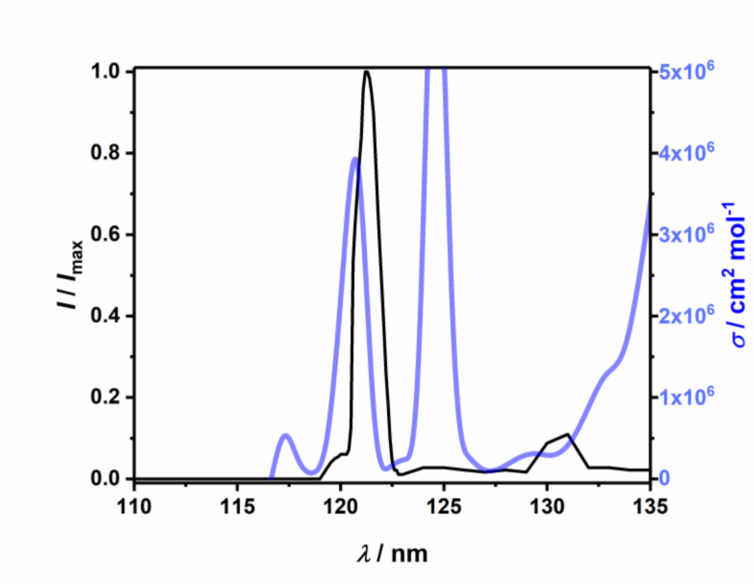

Figure 4.6: H ARAS lamp emission spectrum (black) and absorption coefficients of molecular oxygen (blue) [59].

Even though the absorption coefficient of O_2 is not maximal at ~130 nm, it is sufficiently high to absorb the atomic oxygen emission line in the H ARAS lamp spectrum.

The oxygen filter designed in this work consists of a hollow stainless steel flange which can be installed between the ARAS lamp and the shock tube. The upper side of the flange is sealed by a magnesium fluoride window (Co.: Korth Kristalle, diameter: 12 mm, thickness: 2 mm). Thereby, the filter cavity and the ARAS lamp are separated. The filter is connected to an O_2 gas cylinder and a rotary vane pump (Co.: Pfeiffer, DUO 3M). By a metering valve the pressure inside the filter system can be regulated. It is measured by a pressure gauge (Co.: Pfeiffer, CMR262).

To assess the effects of the oxygen filter, H ARAS lamp spectra were recorded for different oxygen pressures inside the filter setup. The intensities for oxygen and nitrogen atomic emission lines were evaluated relative to the maximum intensity in the spectrum (figure 4.7). With increasing oxygen pressure, the relative intensity of the atomic emission lines decreases. An inner filter pressure between 30 and 50 mbar proved to be sufficient to suppress the atomic oxygen emission line. The intensity of the Lyman-α line is only slightly affected.

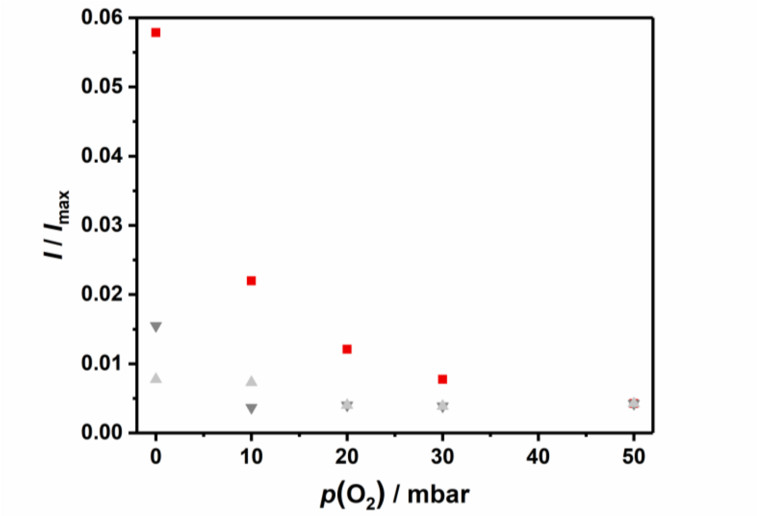

Figure 4.7: Relative intensities of the oxygen (red squares: 130.2 nm) and nitrogen (grey triangles: 119 nm, light grey triangles: 124.3 nm) atomic emission lines with increasing O_2 pressure in the filter flange.

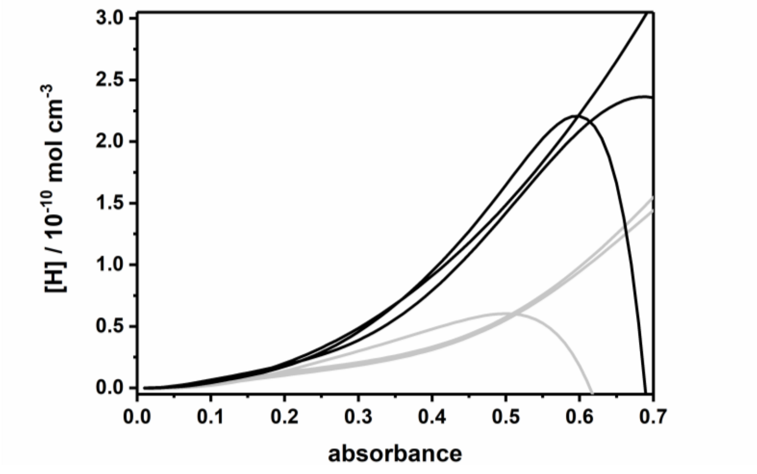

Figure 4.8: Calibration curves for the vertical H-ARAS measured with (black lines) and without (grey lines) the filter flange (p(O2) ~ 30 mbar).

The effect of absorption by oxygen atoms on calibration curves is illustrated in figure 4.8. The original calibration curves for the vertical H ARAS, measured without the oxygen filter, are depicted as grey lines. The black lines were calculated from calibration measurements with the oxygen filter ($p(O_2) \sim 30 – 35$ mbar). The differences between the two groups indicate that atomic absorption by oxygen atoms occurs in the experiments without the filter. As discussed before, suppressing the atomic oxygen emission lines in the lamp spectrum leads to a steepening of the calibration curves deduced from the experiments.

The main disadvantage of the oxygen filter is the insertion of a third magnesium fluoride window into the optical path. Transmission of Lyman-α radiation through the optical window is relatively small (~ 66 % maximum). Consequently, absolute intensities decrease, and the signal-to-noise ratio of the recorded profiles is significantly worsened.

4.3.3 A Vertical I ARAS Setup

To preserve the advantages of the horizontal H ARAS experiment, especially the significantly better signal-to-noise ratio, the feasibility of a vertical I ARAS unit was explored. The I ARAS lamp is operated with a mixture of 1 % methyl iodide in helium. Apart of iodine atoms, the dissociation of the precursor molecule will also yield carbon andhydrogen atoms. The emission lines of these species will most probably be a part of the lamp spectrum.

A representative emission spectrum of an I ARAS lamp (operating conditions: mixture: 1 % CH_3I in He; pressure: ~ 10 mbar) is depicted in figure 4.9. It was recorded with the horizontal ARAS setup, utilizing the monochromator to successively scan wavelengths from 115 to 195 nm. This wavelength range corresponds to the spectral response range of the photomultiplier tube (Co.: Hamamatsu, R1259) employed in the detection setup. Atomic emission lines of hydrogen, nitrogen, oxygen, carbon and iodine can be identified in the lamp spectrum. Only the signals at 163.7 nm, 157.8 nm, 154.2 nm and 123.0 nm could not be assigned to specific transitions.

For I ARAS, often a detection wavelength of 183.0 nm is chosen (e.g. [60]). However, the 183.0 nm emission line could not be identified in the lamp spectrum. To reduce self-absorption effects (see chapter 2.2), the lamp mixture is introduced into the lamp on the side connected to the shock tube. In consequence, a layer of (almost) 1 % methyl iodide in helium will be present in between the emitting plasma and the optical window of the shock tube. Methyl iodide shows a strong absorption ability at 183.0 nm [59]. Thus, it is likely that the 183.0 nm emission line is completely absorbed within the lamp.

In shock tube experiments, hydrocarbon radicals are usually generated from iodinated precursor molecules (e.g. propargyl radicals from C_3H_3I [61], benzyl radicals from C_7H_7I [22]). Following the concentration of I atoms in the system, concentrations of the desired radical species can be

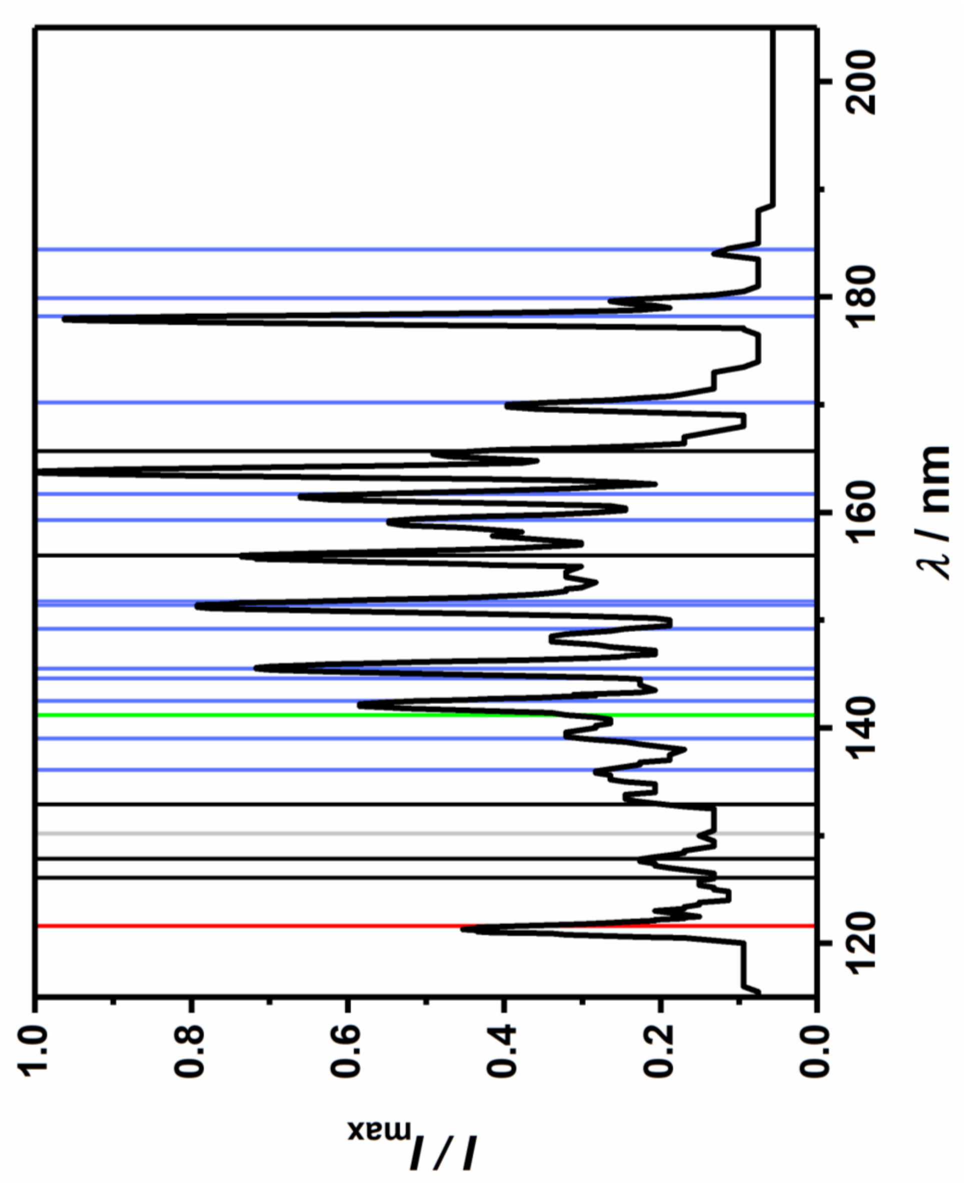

Figure 4.9: Emission spectrum of the I-ARAS lamp (1 % CH_3I in He, p_{lamp} ~ 10 mbar) and selected atomic emission lines (blue: iodine, red: hydrogen, green: nitrogen, grey: oxygen, black: carbon) [28].

inferred. For hydrocarbon radicals, H atoms will almost always be generated during the experiment. If oxygenated species are investigated, a generation of oxygen atoms is also possible. Except under extreme conditions, the production of atomic carbon and nitrogen is highly unlikely. Therefore, to avoid a distortion of I ARAS measurements by the absorption of non-iodine emission lines, it should be sufficient to suppress the oxygen and hydrogen atomic emission lines in the lamp spectrum.

An operation of the I ARAS lamp with mixtures of I_2 in helium could significantly improve the spectrum. However, due to the low vapour pressure of I_2, this solution is not feasible. Thus, in this work the materials of the optical components were changed to restrict the spectral bandwidth transmitted to the detector. The magnesium fluoride windows utilized in the H ARAS setup exhibit a high transmission for wavelengths above 121 nm. For quartz windows, the transmission cut off is shifted to ~ 146 nm. Consequently, the magnesium fluoride window on the upper side of the shock tube was replaced by a quartz window (Co.: Haereus, Suprasil 1, diameter; 12 mm, thickness: 2 mm). No additional optical filter was used.

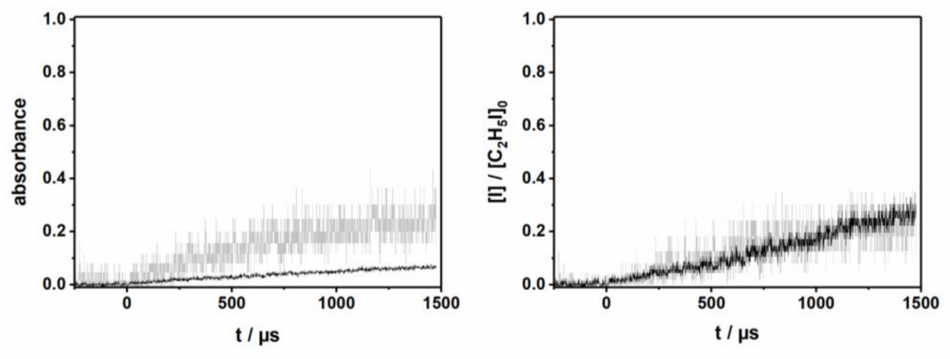

Figure 4.10: Parallel I-ARAS measurement on ethyl iodide decomposition (T = 900 K, p = 1.6 bar, $[C_2H_5I]_0 = 5.7 \times 10^{-11}$ mol cm^{-3}, $[Ar]_0 = 2.1 \times 10^{-5}$ mol cm^{-3}). Absorbance-time (left panel) and relative I atom concentration-time profile (right panel). Black: vertical I ARAS results. Grey: horizontal I ARAS results.

In figure 4.10, results of a dual I ARAS experiment (horizontal and vertical I ARAS) are displayed. Despite the low signal-to-noise ratio of the results obtained with the horizontal ARAS setup, relative I atom concentration-time profiles recorded with the two ARAS units show a good agreement. This indicates that possibly interfering emission lines are effectively blocked by the selected optical window material, and that there is no interaction of the two optical detection units.

Absorbance-time profiles recorded by the two ARAS setups differ noticeably (figure 4.10, left). The broader spectrum transmitted to the detector in the vertical ARAS unit leads to an overall higher intensity and, at the same time, to a smaller ratio of iodine resonance radiation. On the contrary, in the horizontal setup, a single line is isolated with a monochromator. Thus, the fraction of iodine resonance radiation from the total radiation transmitted to the detector is higher. In consequence, higher absorbance values can be recorded.

The low signal-to-noise ratio of the results obtained by the horizontal ARAS experiment are a result of the low overall intensities recorded by the detector. For the test measurements, the horizontal I ARAS setup was operated with a photomultiplier tube with maximum quantum efficiency at 130 nm. At the detection wavelength of the experiments (178.3 nm) the quantum efficiency of the photomultiplier tube accounts to 0.5 %. If a photomultiplier tube with a detection maximum at 180 nm is utilized, the signal quality can be significantly improved.

4.4 The Atom Filter

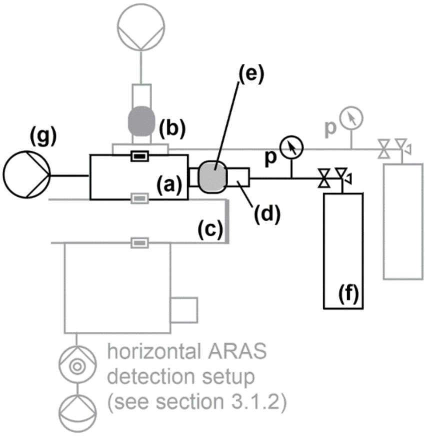

Figure 4.11: The atom filter setup (black) installed within the horizontal ARAS unit (grey). For detailled explanations see text.

A different method to suppress atomic emission lines is the installation of an atom filter. This type of filter can also be used to determine the fraction of resonance radiation in ARAS experiments [62, 63]. This information is necessary for the calculation of calibration curves based on line absorption theory (see section 2.2.1).

In this work, the oxygen filter flange (section 4.3.2) was extended to function as atom filter. In figure 4.11 the combined horizontal ARAS/atom filter setup is depicted. The filter flange (a) is placed between the ARAS lamp (b) and the shock tube (c). A quartz tube (d) (Co.: Aachener Quartzglas, inner diameter: 10 mm; wall thickness: 1.5 mm) is directly mounted to the flange. As in an ARAS lamp, the quartz tube is partly enclosed by an Evenson cavity (e). The quartz tube is connected to a tank (f) containing the atom precursor mixture. A rotary vane pump (g) (Co.: Pfeiffer, DUO 3M) is utilized to evacuate the system. The pressure inside the filter unit can be monitored with a pressure gauge (Co.: Pfeiffer, CTR 262).

Atoms are generated inside the quartz tube by microwave discharge. These atoms pass through the optical path of the ARAS detection setup. In passing, atoms previous relaxed to the ground state absorb the corresponding resonance radiation. If the concentration of atoms in the filter flange is high enough, the remaining signal recorded by the detection unit corresponds to the amount of non-resonance radiation emitted by the ARAS lamp.

The atom filter was tested for H atoms. Filter mixtures contained 1, 3 and 10 % H_2 in helium respectively. The intensity at the detector was recorded with respect to pressure inside the filter unit, which was varied between 0 and 300 mbar.

To describe the behaviour of the filter, the fraction of radiation omitted (*Omr*) was calculated. This fraction was defined as

$$Omr = \frac{I_{\mathrm{max}} - I}{I_{\mathrm{max}}} \cdot 100. \qquad (4.1)$$

Results are displayed in figure 4.12. Error bars account for the signal-to-noise ratio of the experimental data. The microwave input power was set to the same value as for the ARAS lamps and the cavity was adjusted to minimize the fraction of reflected microwave power.

The amount of transmitted radiation decreases with increasing internal pressure in the filter. This inner filter pressure correlates to the amount of H atoms produced within the system. For high pressures, a constant value of omitted light is reached. In the case of the 3 % H_2 filter mixture, this value amounts to circa 87 %. A further increase of the fraction of H_2 in the filter mixture has almost no effect on the omission curve. Decreasing the fraction of H_2 in the filter mixture to 1 % leads to a lower maximum value which is reached at higher inner filter pressures. This indicates, that the concentration of atomic hydrogen generated in the filter setup is too low to ensure a complete absorption of the resonance radiation emitted by the ARAS lamp.

Interestingly, the omission curves exhibit a minimum at small internal filter pressures. At this point, the intensity registered at the detector is higher than the one for zero mbar inner filter pressure and no microwave discharge. The increase in intensity at the minimum depends on the position of the cavity on the quartz tube of the filter. Therefore, it could be an emission effect in the filter. If the excited hydrogen atoms generated by microwave discharge have only partly relaxed to the ground state before passing the optical pathway of the ARAS setup, an emission of resonance radiation by the remaining atoms in the excited state is possible. At the detector, radiation by the ARAS lamp and radiation in the filter cannot be distinguished.

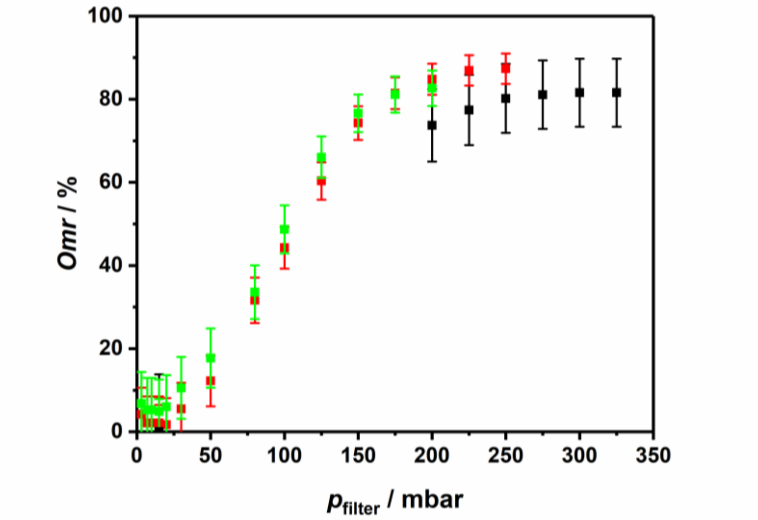

Figure 4.12: Fraction of omitted radiation (*Omr*) as a function of the inner pressure of the atom filter and the percentage of H_2 in the filter mixture: black squares: 1 %; red squares: 3 %; green squares: 10 %.

A different method for the determination of the fraction of resonance radiation emitted by the H ARAS lamp are high temperature experiments on highly concentrated mixtures of H_2 in argon. For very high H_2 concentrations in the mixtures, it can be assumed that all resonance radiation is absorbed by the H atoms produced in the experiment.

For the experimental determination of the Lyman-α fraction, high temperature experiments (T = 2200 – 2600 K) at pressures around 1 bar were performed. Mole fractions of H_2 in the mixtures ranged from 6.5 to 15.0 ‰. The percentage of Lyman-α radiation was calculated with equation (4.1).

The determined resonance radiation fractions are independent of the mole fraction of H_2 in the mixtures. At temperatures below 2400 K it appears that the dissociation of hydrogen is not complete. Fitting of the high temperature values leads to a fraction of resonance radiation of approximately 89 %. This is in good agreement with the values extrapolated from the test of the atomic filter. For the vertical ARAS setup, a lower value is expected. The resonance radiation fraction amounts to approximately 70 %. This is due to the bandwidth of the interference filter as discussed in section 4.3.3.

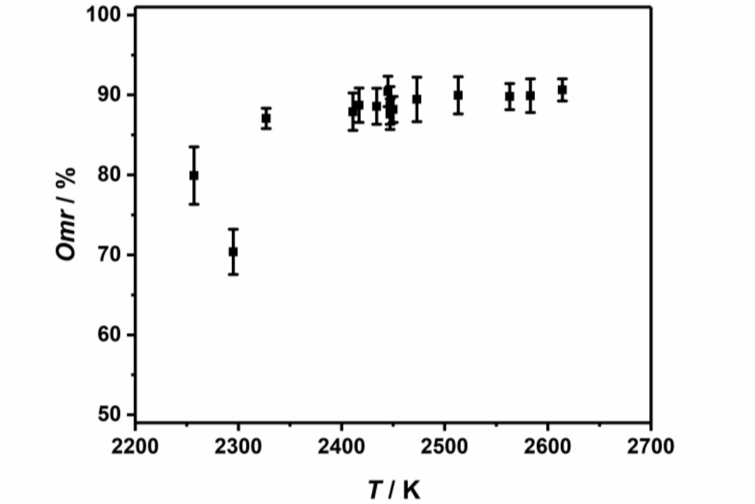

Figure 4.13: Fraction of resonance radiation for the horizontal H ARAS lamp determined in experiments on highly concentrated H_2/argon mixtures.

4.5 Outlook: Variations of the Dual ARAS Setup

The main focus of this chapter was the extension of the existing shock tube/ARAS setup by an additional ARAS detection unit. This was realized for a combination of H and I ARAS. The interchangeability of the two ARAS setups (horizontal H ARAS/vertical ARAS and vice versa) was discussed. The argumentation can be extended to combinations of other ARAS types, if some general principles are considered.

For the operation of an ARAS system, it must be ensured that no atomic emission lines can be absorbed by the probe, except the one of the ARAS target species. Therefore, it is necessary to isolate specific atomic emission lines by restricting the wavelength range to be detected. This can be archived by different methods:

- Choice of lamp gas
- Utilization of a monochromator (horizontal ARAS setup, section 3.1.2)
- Integration of an appropriate optical filter (e.g. narrow band pass filter, compare section 4.3.1)
- Usage of a molecular or atom filter (compare sections 4.3.2 and 4.4)
- Choice of material for optical windows and other optical components

As a consequence, it should be possible to combine most ARAS techniques, if a few precautions are taken. Important is the recording of a complete lamp emission spectrum with respect to the spectral response range of photomultiplier tube. In a second step, atomic emission lines in the spectrum must be identified. To assess the applicability of the ARAS setup as vertical system for a given experiment, the probability of formation of atomic species in the reaction system has to be estimated and possibly interfering absorptions have to be identified. Last, but not least, appropriate steps to restrict the wavelength range must be taken. To demonstrate the underlying thoughts, a possible vertical Cl ARAS experiment will be briefly discussed. It was considered in an attempt to evaluate the suitability of iodine monochloride as an I atom source for the calibration of I ARAS (see section 5.4.1).

The Cl ARAS lamp is operated with mixtures of 1 % molecular chorine (Cl_2) in helium. An inner lamp pressure of 15 mbar proved to be sufficient. The corresponding lamp spectrum is depicted in figure 4.14. Apart from the desired chlorine atomic emission lines, also emission lines of hydrogen, oxygen, nitrogen and carbon atoms could be identified. In experiments on hydrocarbons, the hydrogen and oxygen atomic emission lines in the spectrum have to be suppressed to avoid a distortion of the measurement by hydrogen and oxygen atomic absorption (compare discussion section 4.3.3). However, the use of a quartz optical window as in the vertical I ARAS setup would also block the chlorine atomic emission lines. This problem can be solved by the usage of barium fluoride optical windows in the optical pathway. Thereby, wavelengths shorter than ~ 135 nm are suppressed [34].

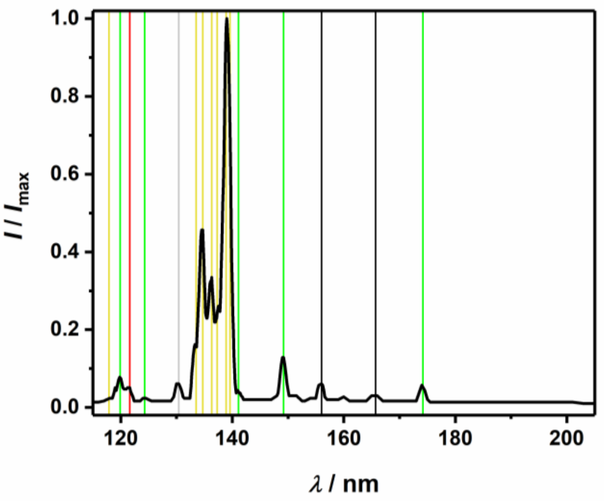

Figure 4.14: Emission spectrum of a Cl ARAS lamp (1 % Cl_2 in He, plamp ~ 15 mbar) and selected atomic emission lines (yellow: chlorine, red: hydrogen, black: carbon, green: nitrogen, grey: oxygen) [28].

5 Thermal Decomposition of Ethyl Iodide: A Test for the Dual ARAS System

5.1 Introduction

The thermal decomposition of ethyl iodide (C_2H_5I) has been investigated in several studies [58, 64-70] throughout the last 25 years. Mechanism and rate coefficients of the system are well known.

$$C_2H_5I \rightarrow C_2H_5 + I \tag{R$_{5.1}$}$$

$$C_2H_5 \rightarrow C_2H_4 + H \tag{R$_{5.2}$}$$

Under shock tube conditions, ethyl iodide mainly reacts by C-I bond fission ($R_{5.1}$). The ethyl radical formed rapidly decomposes to ethylene (C_2H_4) and a H atom ($R_{5.2}$). Since the C-I bond fission is the rate determining step, both reactions can be summarised:

$$C_2H_5I \rightarrow C_2H_4 + H + I \tag{R$_{5.3}$}$$

$$C_2H_5I \rightarrow C_2H_4 + HI \tag{R$_{5.4}$}$$

Butler and Polanyi [71] were the first to note the influence of reaction ($R_{5.4}$) as a second initial reaction channel. Considering only reactions ($R_{5.3}$) and ($R_{5.4}$), concentrations of I and H atoms should be equal at short reaction times.

The relative importance of reactions ($R_{5.1}$) and ($R_{5.4}$) in the consumption of the reactant can be characterized by their branching ratio. This ratio is defined as

$$\phi_{R_{5.1}} = \frac{k_{R_{5.1}}}{k_{R_{5.4}} + k_{R_{5.1}}} = \frac{[I]_\infty}{[C_2H_5I]_0}. \tag{5.1}$$

Branching ratios determined in different studies are compared in figure 5.1. Whilst the values published by Kumaran et al. [58], Miyoshi et al. [72] and Varga et al. [65] show a reasonable good agreement, the one of Weber et al. [66] is significantly lower. Kumaran et al. [58] and Miyoshi et al. [72] both performed shock tube/I ARAS and shock tube/H ARAS experiments. I and H atom yields were determined directly from the measured concentration-time profiles. Weber et al. [66] conducted experiments on considerably higher concentrated mixtures. They followed the thermal decomposition of ethyl iodide at different temperatures in a microreactor/PI-MS setup. The deduced branching ratios depended on the photoionization cross sections of hydrogen iodide and atomic iodine.

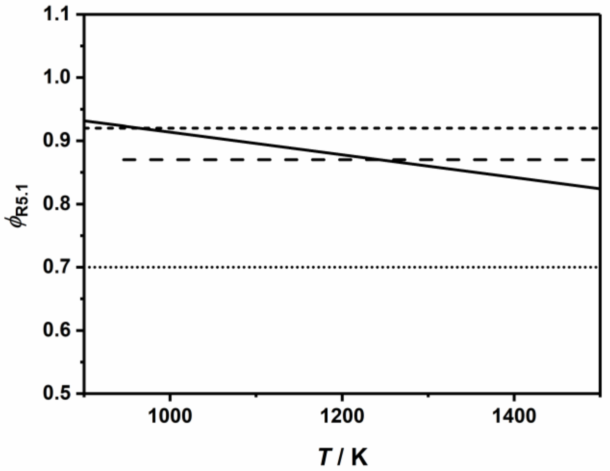

Figure 5.1: Branching ratios for the two initial reaction steps ($R_{5.1}$) and ($R_{5.3}$) in the thermal decomposition of ethyl iodide. Solid line: Varga et al. [65] , dashed line: Kumaran et al. [58], densely dashed line: Miyoshi et al. [72], densely dotted line: Weber et al. [66].

The publication by Varga et al. [65] is based on the experimental results of a shock tube/H ARAS study by Bentz et al. [64]. Additionally taking into account the experimental results of Michael et al. [73] and Vasileiadis and Benson [74] for the reaction

$$H_2 + I \rightarrow H + HI \qquad (R_{5.5})$$

the authors optimized the rate coefficients in the mechanism proposed by Bentz et al. [64]. This optimized mechanism is listed in table 5.1. Branching ratios were determined from the optimized rate coefficients for reactions ($R_{5.1}$) and ($R_{5.4}$).

Table 5.1: Reaction mechanism for the thermal decomposition of ethyl iodide published by Varga et al. [65]. Parameterization: $k(T) = A \times (T/\mathrm{K})^n \times \exp(-E_a/RT)$. Units: s^{-1}, kJ, mol^{-1}, cm^3, K.

	reaction	A	n	E_a	ref.
($R_{5.1}$)	$C_2H_5I \rightarrow C_2H_5 + I$	3.34×10^{13}	0.00	203.5	[65]
($R_{5.2}$)	$C_2H_5 + M \rightarrow C_2H_4 + H + M$	1.00×10^{18}	0.00	139.7	[65]
($R_{5.4}$)	$C_2H_5I \rightarrow C_2H_4 + HI$	4.68×10^{13}	0.00	225.9	[65]
($R_{5.6}$)	$H + HI \rightarrow H_2 + I$	6.61×10^{13}	0.00	4.1	[65]
($R_{5.7}$)	$C_2H_5I + H \rightarrow C_2H_5 + HI$	1.00×10^{15}	0.00	21.5	[65]

The thermal decomposition of ethyl iodide is a suitable test system for the new dual ARAS setup, since mechanistic details are well known. As the concentrations of H and I atoms must be equal for short reaction times, the quality of the measurement and calibration techniques can be assessed. Therefore, as a first trial of the new instrumental setup, branching ratios for the initial steps in the thermal decomposition of ethyl iodide were determined.

Parts of the experiments presented in this chapter have been performed in a student work supervised by the author. F. Poschen conducted some of the experiments on the calibration of I ARAS and the revaluation of the rate coefficient for the C-I bond fission reaction in methyl iodide during his seven week practical lab course (‘Vertieferpraktikum’).

5.2 Experiments and Calibration

To test the performance of the dual ARAS setup, experiments on mixtures of ethyl iodide were conducted. Concentration-time profiles of I and H atoms were recorded simultaneously. Results obtained with both types of dual ARAS setup (horizontal H ARAS + vertical I ARAS and horizontal I ARAS + vertical H ARAS) were evaluated. Branching ratios were deduced directly from the measured I atom concentration-time profiles at long reaction times. A temperature range from 900 to 1400 K was covered in the experiments. Pressures behind the reflected shock waves ranged between 1.6 and 1.8 bar to enable a comparison to older experiments by T. Bentz [75]. Mole fractions of ethyl iodide were varied between 2.2 and 8.0 ppm (absolute concentrations: 2.2×10^{-11} to 1.5×10^{-10} mol cm^{-3} ethyl iodide).

H ARAS experiments were calibrated with mixtures of N_2O and H_2 in argon as described in section 2.2.3. For I ARAS calibration, measurements on the thermal decomposition of methyl iodide were performed. The mixtures contained between 0.5 and 10 ppm methyl iodide in argon. I atom concentrations in the system were simulated with the mechanism proposed by T. Bentz [75] (table 5.2). The thermodynamic data for all species in the mechanisms of this chapter were adopted from the database by Burcat et al. [76].

Table 5.2: Reaction mechanism for the thermal decomposition of methyl iodide (calibration I ARAS) from T. Bentz [75]. Parameterization: $k(T) = A \times (T/\mathrm{K})^{n} \times \exp(-E_a/\mathrm{R}T)$. Units: s^{-1}, kJ, mol^{-1}, cm^3, K.

	reaction	A	n	E_a	ref.
($R_{5.8}$)	$CH_3I + M \rightarrow CH_3 + I + M$	2.65×10^{15}	0.00	165.0	[60]
($R_{5.9}$)	$CH_3 + M \rightarrow CH_2 + H + M$	1.70×10^{-8}	0.00	379.0	[37]
($R_{5.10}$)	$H + I + M \rightarrow HI + M$	2.07×10^{10}	0.50	183.0	[77]
($R_{5.6}$)	$HI + M \rightarrow H + I + M$	5.00×10^{15}	0.00	340.9	[23]
($R_{5.11}$)	$I + HI \rightarrow H + I_2$	7.83×10^{14}	0.00	155.0	[78]
($R_{5.12}$)	$H + HI \rightarrow H_2 + I$	4.76×10^{13}	0.00	2.7	[79]
($R_{5.13}$)	$I + I + M \rightarrow I_2 + M$	2.36×10^{14}	0.00	6.3	[79]

5.3 Experimental Results: Comparison to the Mechanism by Varga et al. [65]

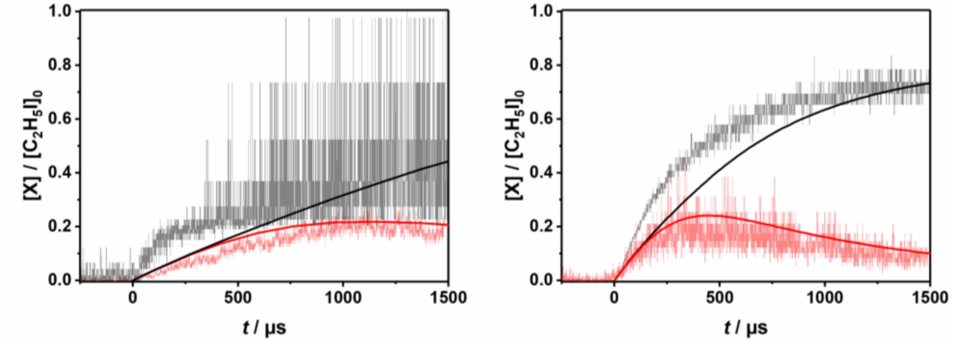

Figure 5.2: Comparison of simulated and measured relative concentration-time profiles for H (red) and I atoms (black). Simulated mechanism: Varga et al. [65] (table 5.1). Experiments: T = 970 K, p = 1.7 bar, $[C_2H_5I]_0$ = 5.1×10^{-11} mol cm^{-3}, $[Ar]_0 = 2.2 \times 10^{-5}$ mol cm^{-3}, horizontal H ARAS, vertical I ARAS (left panel); T = 1012 K, p = 1.2 bar, $[C_2H_5I]_0 = 1.2 \times 10^{-10}$ mol cm^{-3}, $[Ar]_0 = 1.4 \times 10^{-5}$ mol cm^{-3}, horizontal I ARAS, vertical H ARAS (right panel).

In figure 5.2 results of two different measurements are compared to concentration-time profiles simulated based on the mechanism by Varga et al. [65]. The experiments depicted differ not only in their experimental conditions, but also in the experimental technique employed. The lower temperature experiment (left panel) was conducted with a horizontal H ARAS/vertical I ARAS configuration of the dual ARAS setup. Lower absorbances for the I ARAS measurements result in significantly higher signal-to-noise ratios. These get even worse for longer reaction times, as the calibration curves are steeper for higher absorbance values. This problem can be reduced by decreasing the reactant concentrations in the mixtures investigated.

The experiment shown in the right panel of figure 5.2 was performed with a horizontal I ARAS/vertical H ARAS dual ARAS setup. Here, the H ARAS results exhibit the lower signal-to-noise ratio for the same reason previously discussed for the vertical I ARAS results

For both measurements, H atom concentrations are well described by the model. I atom concentrations are underestimated for short reaction times. At long reaction times, the agreement of simulation and experiment improves as can be noted in the right panel of figure 5.2. For temperatures above ~1200 K, the agreement of simulated and experimentally determined profiles improves considerably. This is mainly due to the restricted time resolution of the experiment. The initial increase in I atom concentration is so high that it cannot be resolved by the detection technique anymore.

As discussed in section 5.1, the initial reaction steps in the pyrolysis of ethyl iodide should yield the same amount of H and I atoms. The H ARAS calibration method employed in this work is well established and H atom concentration-time profiles are sufficiently well predicted by the model. Thus, errors in the initial concentrations of ethyl iodide caused by wall adsorption of the reactant are unlikely. In consequence, the I atom concentration-time profiles probably are erroneous. These errors most likely originate from errors in the calibration.

I ARAS experiments presented in this section were calibrated based on measurements of methyl iodide pyrolysis. The corresponding calibration curves strongly depend on the rate coefficient for the C-I bond fission reaction ($R_{5.8}$), as can be noted from the time-dependent sensitivity analysis for iodine atoms in the mechanism by T. Bentz [75] depicted in figure 5.3. A factor two decrease or increase of this rate coefficients leads to a doubling of halving of I atom concentrations at short reaction times. This directly translates into an increase or decrease in the initial slopes of deduced calibration curves.

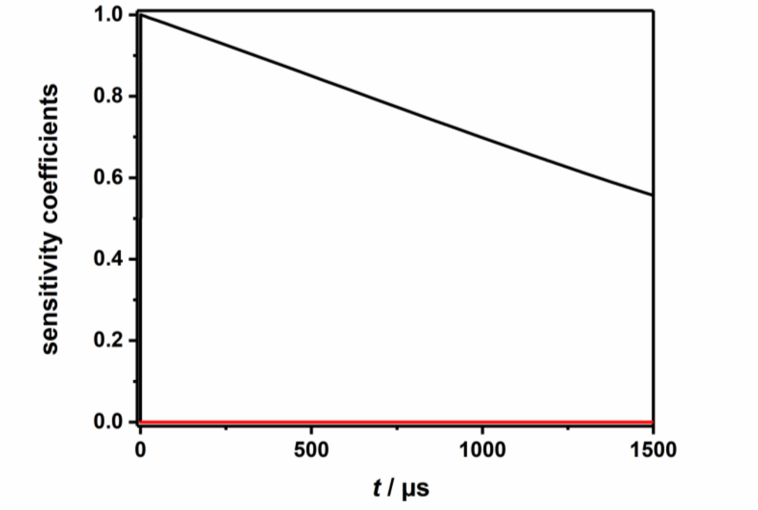

Figure 5.3: Time-dependent sensitivity analysis for I atoms in the thermal decomposition of methyl iodide. Mechanism: T. Bentz ([75], table 5.2). Experimental conditions: T = 1081 K, p = 1.7 bar, $[CH_3I]_0 = 4.59 \times 10^{-11}$ mol cm^{-3}, $[Ar]_0 = 1.93 \times 10^{-5}$ mol cm^{-3}. Reactions: black: ($R_{5.8}$), red: ($R_{5.9}$)-($R_{5.13}$).

To improve the calibration of I ARAS and to obtain consistent results for the pyrolysis of methyl and ethyl iodide, two approaches were chosen. Firstly, a separate I atom source was investigated. Iodine monochloride has been chosen due to its very simple structure. The results of experiments on iodine monochloride decomposition are discussed in section 5.4.1. Secondly, the thermal decomposition of methyl iodide was reviewed and reinvestigated by new shock tube/H ARAS/ I ARAS experiments. Results are presented in section 5.4.2.

5.4 I ARAS Calibration

5.4.1 Iodine Monochloride: An Alternative I Atom Source

Iodine monochloride is synthesized from Cl_2 and I_2 by the reverse reaction of ($R_{5.14}$). Two decomposition pathways are feasible yielding either molecular ($R_{5.14}$), or atomic ($R_{5.15}$) iodine and chlorine. It is sensitive to hydrolysis ($R_{5.16}$) with hydrogen chloride and hypoiodic acid as hydrolysis products.

$$ICl + ICl \rightleftharpoons I_2 + Cl_2 \tag{$R_{5.14}$}$$

$$ICl \rightarrow I + Cl \tag{$R_{5.15}$}$$

$$ICl + H_2O \rightarrow HCl + IOH \tag{$R_{5.16}$}$$

Kinetic studies on iodine monochloride are scarce and mainly concerned with photolysis [80] or bimolecular reactions with halogens [81, 82] or H_2 [83-85]. In most studies, iodine monochloride is synthesized in situ from Cl_2 and I_2. Consequently, the exact determination of the initial reactant concentrations in the experiments is difficult.

Benson et al. [86] discussed iodine monochloride as a possible thermal source of chlorine atoms at lower temperatures (470 – 610 K). They spectroscopically studied the reaction of atomic chlorine with atomic hydrogen in a packed vessel reactor. Iodine monochloride was synthesized inside the reactor.

The only shock tube study on iodine monochloride has been performed by Zhang et al. [87] in 1983. Iodine monochloride was generated in situ in the mixing vessels. Its thermal decomposition was followed spectroscopically (detection wavelength: 423 nm, 669 nm). Temperatures in the experiments ranged between 1000 and 2000 K. A rate coefficient for reaction ($R_{5.15}$) was deduced.

In this work, a few experiments on the thermal decomposition of iodine monochloride were conducted to assess its suitability as an iodine atom source in shock tube experiments. Iodine monochloride was obtained from Sigma-Aldrich and used without further purification. To avoid the hydrolysis of the reactant, all glass vessels have been thoroughly dried and stored over phosphor pentoxide prior to use. Only small amounts of mixtures were prepared to prevent condensation of the reactant in the mixing vessels. During mixture preparation, a pressure of 0.06 mbar iodine monochloride was not exceeded. Mole fractions in the mixtures were set to 4.3 and 5.8 ppm. A temperature range from 1010 to 2010 K was covered by the experiments. Pressures ranged between 1.4 and 1.8 bar.

Experiments were conducted with the new dual ARAS setup (vertical I ARAS, horizontal H ARAS). A detection of hydrogen atoms by H ARAS would have indicated hydrolysis products. However, no absorbance by H atoms was recorded.

In figure 5.4, the results of maximum absorbance measurements (compare section 2.2.3) on iodine monochloride are displayed. For comparison, representative calibration curves deduced from experiments on methyl iodide decomposition are also shown. The results suggest significantly higher I atom concentrations for low absorbance values. Extrapolating the results for the 4.3 ppm mixture to an absorbance value of zero leads to the conclusion that at zero absorbance, circa 4×10^{-11} mol cm^{-3} of iodine atoms should be present in the shock tube. This is highly unlikely. However, it cannot be a consequence of a low sensitivity of the I ARAS technique, as lower concentrations have been resolved in experiments on methyl and ethyl iodide before.

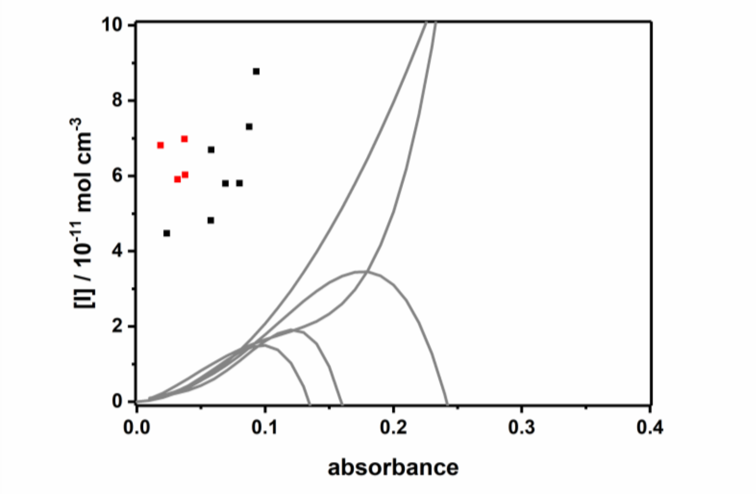

Figure 5.4: Results of maximum absorbance measurements on iodine monochloride (red squares: 5.8 ppm, black squares: 4.3 ppm). Grey lines: calibration curves from experiments on methyl iodide decomposition.

Absorbance values recorded depended on the time between mixture preparation and the experiment. Experiments could only be performed the day after mixture preparation. Two explanations are possible: Either iodine monochloride was directly absorbed onto the walls of the mixing vessel, or it decomposed according to reaction ($R_{5.14}$) and the product(s) were (at least partly) absorbed. Complete dissociation after mixture preparation would not have any influence on the actual atomic concentration as the total numbers of chlorine and iodine atoms do not change.

According to Wiberg [88], iodine monochloride decomposes during evaporation. This is in line with the brown gasses which were noted when the reactant containing glass vessel was evacuated. Lowering the pressure in a system leads to a decrease in evaporation temperatures.

In consequence, it is highly probable that mixtures consisted of molecular chlorine and molecular iodine which are in equilibrium with a certain amount of iodine monochloride. Due to its very low vapour pressure, molecular iodine will most probably condense onto the walls of the mixing vessel. Thereby, the equilibrium ($R_{5.14}$) will be shifted towards the decomposition products. The mixture in the low-pressure section of the shock tube will consist of molecular iodine, maybe some iodine monochloride, and molecular chlorine. Absolute concentrations cannot be assigned due to the apparently complex processes preceding. Hence, calibration of I ARAS by measurements on iodine chloride is not possible.

5.4.2 Thermal Decomposition of Methyl Iodide

5.4.2.1 Literature Overview

The first study on thermal reactions of methyl iodide was conducted by Ogg [89] in 1934. Nine years later, Butler and Polanyi [71] determined bond energies in different organic iodides. To deduce the bond energy of the C-I bond in methyl iodide, they measured rate coefficients for its thermal decomposition at around 767 K (494 °C). However, Horrex and Lapage [90] repeated their experiments, but could not reproduce the rate coefficients of the original study. From their experimental results, the authors deduced a first order rate coefficient of

$$k_{1\mathrm{st}}(T) = 2.6 \cdot 10^{13} \cdot \exp\left(-\frac{229\ \mathrm{kJ\ mol^{-1}}}{\mathrm{R}T}\right)\mathrm{s^{-1}}. \tag{5.1}$$

Saito et al. [91] investigated the thermal decomposition of methyl iodide in shock tube experiments. Mixtures contained 0.2 to 3.0 mol% methyl iodide in argon. Experiments were performed at different pressures (0.4 to 3.2 bar (total densities: 3.5×10^{-6} - 3.9×10^{-5} mol $\mathrm{cm^{-3}}$)) in a temperature range from 1050 to 1500 K. To deduce a rate coefficient for the initial decomposition step, the authors followed the depletion of methyl iodide concentration by monitoring its absorption at 259 and 275 nm. Absorption-time profiles were directly transformed into concentration-time profiles by Beer-Lamberts law. The low pressure rate coefficient was parameterized as

$$k_{2\mathrm{nd}}(T) = 2.5 \cdot 10^{15} \cdot \exp\left(-\frac{178\ \mathrm{kJ\ mol^{-1}}}{\mathrm{R}T}\right)\mathrm{cm^{3}\ mol^{-1}\ s^{-1}}. \tag{5.2}$$

To further interpret their results, the authors proposed a small reaction scheme (9 reactions, 10 species). Computer simulations indicated that the published second order rate coefficient corresponds to the unimolecular C-I bond fission reaction. Four years later, the authors further investigated the thermal decomposition of methyl iodide in two different bath gases, helium and krypton [92]. Collision efficiencies, and average energies transferred per collision, were deduced.

In 1990, Kodama et al. [93] published high-pressure rate coefficients for the dissociation of methyl iodide and perdeuterated methyl iodide. Experiments were conducted in a quartz reactor at seven temperatures between 600 and 650 K and pressures ranging from 20 to 200 mbar. Product yields were measured by gas chromatography and mass spectrometry. Methane and I_2 were identified as the main products under all experimental conditions. From the rate of formation for methane, a dissociation rate coefficient for methyl iodide was deduced.

A comparative study of different methyl radical precursors was conducted by Davidson et al. [94] in 1993. Concentrations of methyl radicals were directly measured by UV laser absorption. From simulations of the measured concentration-time profiles, the authors determined a bimolecular rate coefficient for the decomposition of methyl iodide:

$$k_{2\mathrm{nd}}(T) = 3.0 \cdot 10^{14} \cdot \exp\left(-\frac{133\ \mathrm{kJ\ mol^{-1}}}{\mathrm{R}T}\right)\mathrm{cm^3\ mol^{-1}\ s^{-1}}. \tag{5.3}$$

Baeck et al. [95] studied the reaction of methyl radicals with H_2 in a shock tube/UV absorption experiment at temperatures between 1250 and 1950 K. Azomethane and methyl iodide were utilized as methyl radical precursors. Results were independent from the choice of the precursor molecule. However, to satisfactorily simulate the experimental results obtained for the methyl iodide/H_2 mixtures, the rate coefficient for the C-I bond fission in methyl iodide had to be adjusted. The resulting second order rate coefficient was parameterized as

$$k_{2\mathrm{nd}}(T) = 3.2 \cdot 10^{13} \cdot \exp\left(-\frac{111\ \mathrm{kJ\ mol^{-1}}}{\mathrm{R}T}\right)\mathrm{cm^3\ mol^{-1}\ s^{-1}}. \tag{5.4}$$

A shock tube/I ARAS study on the thermal decomposition of methyl iodide was published by Kumaran et al. [60] in 1997. The experiments covered a temperature range from 1052 to 1616 K at pressures between 135 and 1100 mbar (102 – 828 torr). Mixtures contained 1.2 to 5.8 ppm methyl iodide in krypton. I atoms were detected at 183.0 nm. Absorbance values were transferred to absolute I atom concentrations by Beer-Lamberts law, accepting an absorption cross section of $\sigma_I = 1.93 \times 10^{-14}$ cm^2. From the experimentally determined I atom yield of one, the authors concluded that the C-I bond fission channel is the only decomposition pathway. Bimolecular channels like ‘I + CH_3I’ or ‘CH_3 + CH_3I’ ought to be of negligible importance.

Rate coefficients were determined by least square analysis of semi-log plots of concentration-time profiles and a bimolecular rate coefficient was published:

$$k_{2\mathrm{nd}}(T) = 2.62 \cdot 10^{15} \cdot \exp\left(- \frac{165\ \mathrm{kJ\ mol^{-1}}}{\mathrm{R}T}\right) \mathrm{cm^3\ mol^{-1}\ s^{-1}}. \tag{5.5}$$

In the same year, Takahashi et al. [96] reported on another shock tube/ARAS study under very similar conditions. They investigated the thermal decomposition of methyl iodide and methyl bromide in argon and nitrogen, recording halogen atom concentration-time profiles by I and Br ARAS respectively. Temperatures between 1180 and 1600 K were covered at pressures between 1.5 and 2.2 bar (total concentrations: 8.6×10^{-6} - 4.0×10^{-5} mol cm^{-3}). Rate coefficients were directly determined from measured absorption-time profiles, assuming that Beer-Lambert law is valid for the detection setup utilized. For methyl iodide in argon as bath gas, the following second order rate coefficient was deduced:

$$k_{2\mathrm{nd}}(T) = 2.28 \cdot 10^{15} \cdot \exp\left(- \frac{165\ \mathrm{kJ\ mol^{-1}}}{\mathrm{R}T}\right) \mathrm{cm^3\ mol^{-1}\ s^{-1}}. \tag{5.6}$$

In 2009, Yang et al. [2] studied the suitability of methyl iodide as a methyl radical precursor for higher concentration shock tube studies. They investigated the vibrational relaxation and thermal decomposition of methyl iodide by laser schlieren densitometry at temperatures between 630 and 2200 K and low pressures (27, 88, 197 and 373 mbar (20, 66, 148 and 280 torr)). Mixtures of 2 and 4 % methyl iodide in krypton were used in the decomposition experiments. At lower temperatures, rate coefficients for the initial C-I bond fission reaction were directly deduced from initial density gradients. The rate coefficient was parameterized as

$$k_{2\mathrm{nd}}(T) = 4.23 \cdot 10^{50} \cdot (T/\mathrm{K})^{-9.52} \cdot \exp\left(- \frac{299\ \mathrm{kJ\ mol^{-1}}}{\mathrm{R}T}\right) \mathrm{cm^3\ mol^{-1}\ s^{-1}}. \tag{5.7}$$

To simulate their laser schlieren profiles, the authors developed a medium sized reaction mechanism (34 reactions, 15 species) based on an ethane pyrolysis scheme published by Kiefer et al. [97]. Rate coefficients for the decomposition of ethane yielding two methyl radicals, and the reaction of methyl iodide with H atoms yielding a methyl radical and hydrogen iodide, were varied to optimize the agreement of simulated and measured profiles.

5.4.2.2 Experiments

Measurements of I and H atom concentrations were performed in two different temperature ranges. Experiments at low temperatures (900 to 1250 K) were aimed at the revaluation of the rate coefficient for the initial C-I bond fission reaction. Experiments at high temperatures (1700 to 2000 K) were conducted to crosscheck the available literature mechanisms. At these temperatures, a formation of H atoms was observed. The new dual ARAS setup was utilized for all experiments. Pressures ranged between 1.3 and 1.8 bar.

H ARAS experiments were calibrated with mixtures of N_2O and H_2 in argon as described in section 2.2.3. For I ARAS calibration a combined approach was chosen. At low concentrations, I ARAS was calibrated with experiments on mixtures of ethyl iodide in argon using the Varga mechanism ([65], table 5.1) for the simulation of I atom concentration-time profiles. For high concentrations, results of maximal absorbance measurements on methyl iodide mixtures as discussed in section 2.2.3 were utilized. The approach is further illustrated in figure 5.5.

Straight lines at low absorbances are generated from the results of calibration experiments on ethyl iodide. A slight temperature dependence can be noted. The results of maximal absorbance measurements on methyl iodide are represented by black squares. Both results were fitted separately. Measured absorbance-time profiles were calibrated depending on the absolute absorbance values. For absorbances smaller ~ 0.07, calibration curves from ethyl iodide experiments were used. For values higher ~ 0.07 the fitting polynomial of the maximum absorbance measurements was employed. The resulting ‘final’ calibration curve is represented by the thick red line.

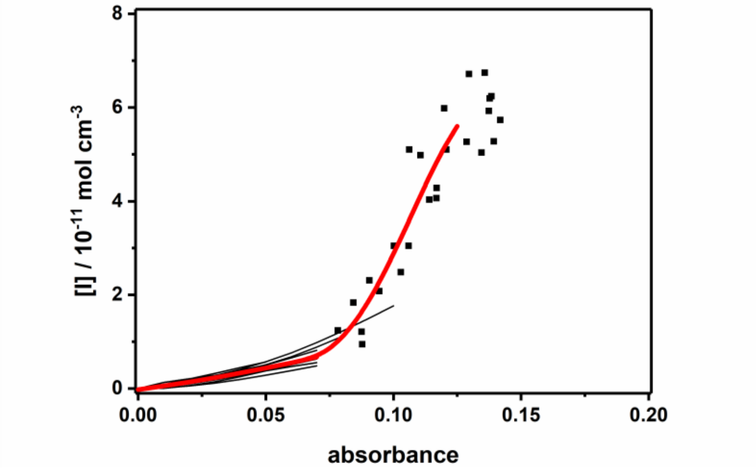

Figure 5.5: Combined approach for the determination of I-ARAS calibration curves. Black lines: calibration curves form ethyl iodide decomposition experiments. Black squares: results from maximum absorbance experiments on methyl iodide/argon mixtures. Red thick line: one calibration curve.

5.4.2.3 I ARAS Results: The C-I Bond Fission in Methyl Iodide

To investigate the C-I bond fission reaction ($R_{5.8}$) in methyl iodide, I ARAS results of the dual ARAS measurements were analysed. For temperatures above ~1250 K the decomposition process could not be temporally resolved by the detector. Thus, only measurements at temperatures between 950 and 1250 K are included in the determination of the rate coefficient for reaction ($R_{5.8}$). Rate coefficients were determined directly from the initial slope of the measured I atom concentration-time profiles as discussed in section 2.3.4. Error bars account to 50 %. Lower signal-to-noise ratios and low absorbances increase the error in the determined rate coefficients compared to results obtained with a horizontal I ARAS setup.

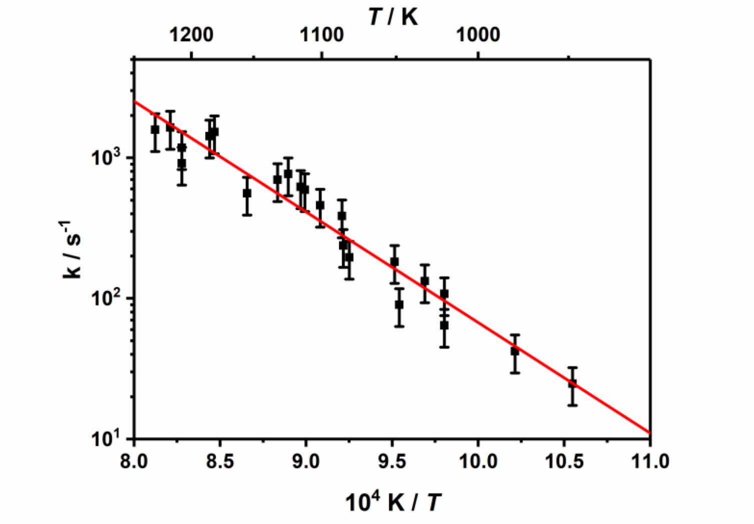

Figure 5.6: Arrhenius plot of the experimentally determined rate coefficients for the unimolecular C-I bond fission reaction in methyl iodide (p = 1.3 – 1.8 bar). Error bars: 50 %. Red line: Arrhenius fit.

From the Arrhenius plot depicted in figure 5.6, a unimolecular rate coefficient was parameterized as

$$k\ (T) = 4.9 \cdot 10^{9} \cdot \exp\left(-\frac{151\ \text{kJ mol}^{-1}}{\text{R}T}\right) \text{s}^{-1}. \tag{5.8}$$

For comparison with the literature, a bimolecular rate coefficient was also determined assuming that the rate coefficient is close to its low pressure limit:

$$k_{(\mathrm{R}5.8)}(T) = 7.4 \cdot 10^{14} \cdot \exp\left(-\frac{160\ \mathrm{kJ\ mol^{-1}}}{\mathrm{R}T}\right) \mathrm{cm^3\ mol^{-1}\ s^{-1}}. \tag{5.9}$$

The rate coefficient deduced in this work lies between the one published by Saito et al. [91] and the ones of Kumaran et al. [60] and Takahashi et al. [96]. The rate coefficients determined by Baeck et al. [95] and Davidson et al. [94] are almost an order of magnitude higher (compare figure 5.7).

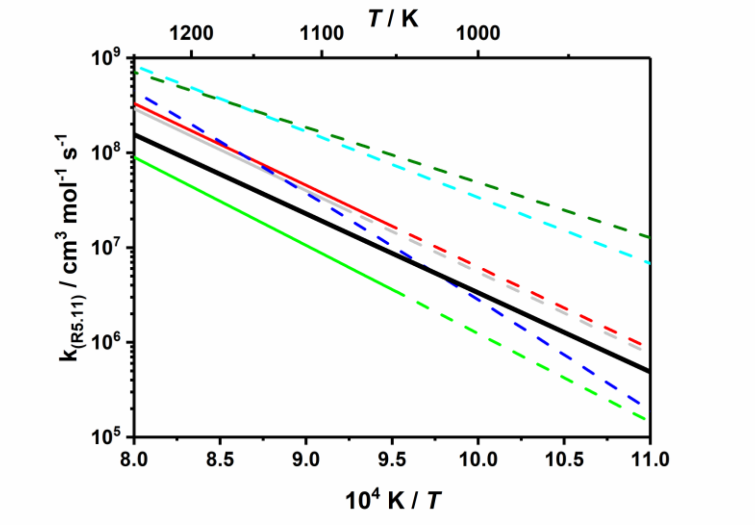

Figure 5.7: Comparison of the bimolecular rate coefficient of this work (straight black line) with rate coefficients from the literature: dark green: Baeck et al. [95] (*p* = 0.3 – 3.4 bar) ; light blue: Davidson et al. [94] (*p* = 1 – 1.25 bar) ; blue: Yang et al. [2] (*p* = 27 – 373 mbar); red: Kumaran et al. [60] (*p* = 0.13 – 1.1 bar); grey: Takahashi [96] (*p* = 1.5 – 2.2 bar); green: Saito et al. [91] (*p* = 0.4 – 3.2 bar).

Kumaran et al. [60] and Takahashi et al. [96] studied the thermal decomposition of methyl iodide in shock tube/I ARAS experiments. The experimental conditions were very similar to the ones in this work. Takahashi et al. [96] deduced rate coefficients directly from the intensity-time profiles recorded. The authors assumed that the reaction proceeds as first order reaction, and Beer-Lamberts law is valid. Whilst the first assumption should be acceptable, the second one is rather critical for ARAS experiments. By working with highly diluted lamp mixtures (0.03 % I_2 in helium compared to 1 % methyl iodide in helium in this work), self-absorption effects in the ARAS setup were reduced. Nevertheless, deviations from Beer-Lamberts law occur for high absorbance values. These influence the rate coefficients determined.

Like Takahashi et al. [96], also Kumaran et al. [60] worked with highly diluted lamp mixtures. For the transformation of absorbance-time profiles into concentration-time profiles, they used Beer-Lamberts law and a constant absorption coefficient. This absorption coefficient has been determined in an earlier study [98] by maximum absorbance experiments on trifluoromethyl iodide (CF_3I). Disadvantages of this type of experiment for the measurement of low concentrations have been discussed in section 2.2.3.

The rate coefficients published by Beack et al. [95], Davidson et al. [94] and Saito et al. [91] were deduced from simulations of experimental results. Saito et al. [91] followed the concentration of methyl iodide, whilst Davidson et al. [94] and Baeck et al. [95] recorded methyl radical concentration-time profiles. Absorption measurements like these can be distorted by secondary absorption of different species. In the case of methyl iodide measurements, secondary absorption would lead to a presumably higher concentration of the reactant and thus a slower depletion. This would result in an underprediction of the rate coefficient. On the contrary, secondary absorption in product concentration measurements leads to the assumption of higher product concentrations, and thus faster product forming reactions. Rate coefficients would be overestimated.

5.4.2.4 H ARAS Results: Mechanistic Considerations

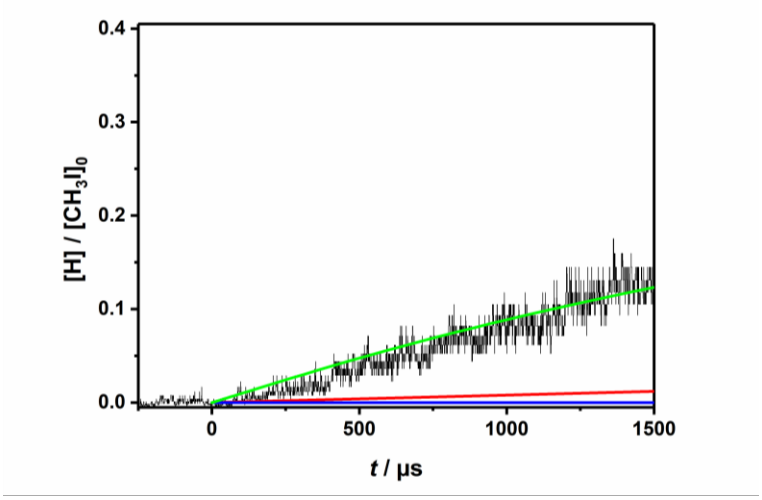

Figure 5.8: Comparison of measured H atom concentrations (T = 1970 K, p = 1.4 bar, $[CH_3I]_0 = 4.9 \times 10^{-11}$ mol cm^{-3}, $[Ar]_0 = 8.9 \times 10^{-6}$ mol cm^{-3}) to simulations with the mechanisms by Saito et al. (blue, [91]), T. Bentz (red, [75]) and Yang et al. (green, [2]).

At temperatures above circa 1650 K, H atoms could be detected in the dual ARAS experiments. In figure 5.8 measured and simulated H atom concentration-time profiles are compared. In the mechanism by Saito et al. [91] no H atom forming or consuming reactions are included. Thus, no H atoms are predicted by the model at any time and temperature.

The only reaction pathway leading to a formation of H atoms in the mechanism by T. Bentz [75] is the unimolecular decomposition of methyl radicals ($R_{5.9}$). As this reaction is slow, only small quantities of H atoms are expected even at high temperatures. The recombination reactions of two methyl radicals, yielding either ethane or an ethyl radical and a H atom, are not included in this model.

These reactions are incorporated in the mechanism by Yang et al. [2]. Furthermore, reactions of hydrocarbons up to propane are considered. The main sources of H atoms are summarized in figure 5.9. H atoms are mainly formed directly from methyl radicals. At lower temperatures, this is mainly due to the recombination reaction forming an ethyl radical and a H atom. For higher temperatures, there is also some influence of the C-H bond fission reaction. This is in line with ethyl radicals being the second most important source of H atoms in the system.

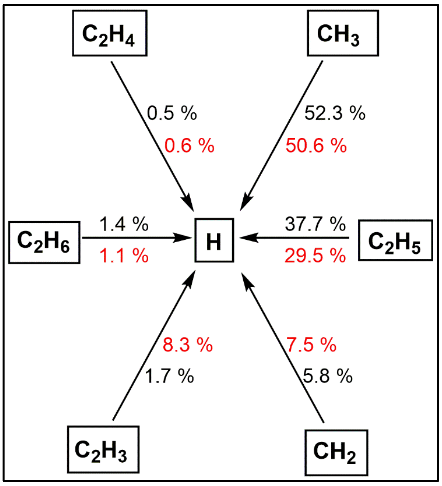

Figure 5.9: Reaction flux analysis for the formation of H atoms in the mechanism by Yang et al. [2]. t ~ 500 µs (black) and t ~ 1500 µs (red). Experimental conditions: T = 1970 K, p = 1.4 bar, $[CH_3I]_0 = 4.9 \times 10_{-11}$ mol cm^{-3}, $[Ar]_0 = 8.9 \times 10^{-6}$ mol cm^{-3}.

From the results of a time-dependent sensitivity analysis (figure 5.10), the recombination reaction of methyl radicals can be identified as the rate determining step in the formation of H atoms from methyl iodide. The C-I bond fission reaction ($R_{5.8}$) is too fast to have an influence.

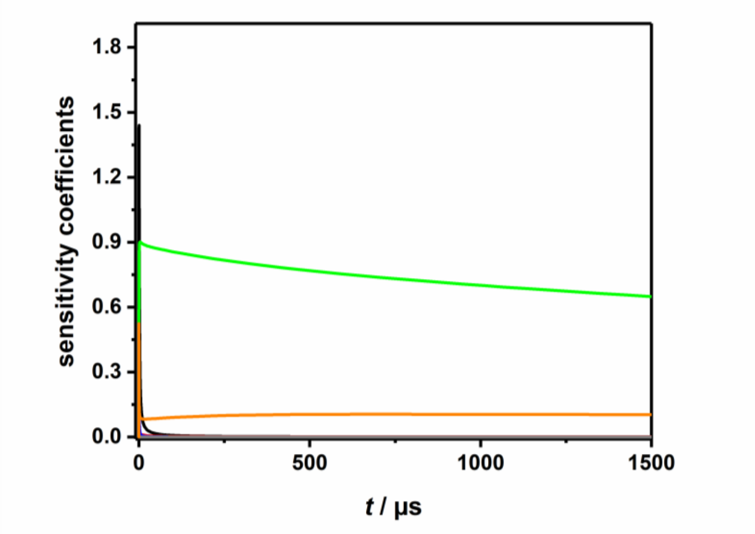

Figure 5.10: Time-dependent sensitivity analysis for H atoms in the mechanism by Yang et al. [2]. Reactions: black: ($R_{5.8}$), green: $CH_3 + CH_3 \rightleftharpoons C_2H_5 + H$ ($R_{5.17}$), orange: ($R_{5.9}$). Experimental conditions: T = 1970 K, p = 1.4 bar, $[CH_3I]_0 = 4.9 \times 10^{-11}$ mol cm^{-3}, $[Ar]_0 = 8.9 \times 10^{-6}$ mol cm^{-3}.

It is therefore possible to describe the experimental results of this work with only a few reactions. These are listed in table 5.3.

Table 5.3: Reaction mechanism for the thermal decomposition of methyl iodide. Parameterization: $k(T) = A \times (T/K)^n \times \exp(-E_a/RT)$. Units: s^{-1}, kJ, mol^{-1}, cm^3, K.

	reaction	A	n	E_a	ref.
($R_{5.8}$)	$CH_3I + M \rightleftharpoons CH_3 + I + M$	7.40×10^{14}	0.00	160	p.w.
($R_{5.9}$)	$CH_3 \rightleftharpoons CH_2 + H$	1.70×10^{-8}	0.00	397	[99]
($R_{5.17}$)	$CH_3 + CH_3 + M \rightleftharpoons C_2H_6 + M$	3.50×10^{-7}	- 7.00	12	[99]
($R_{5.18}$)	$CH_3 + CH_3 \rightleftharpoons C_2H_5 + H$	9.00×10^{-11}	0.00	76	[99]
($R_{5.19}$)	$C_2H_5 + M \rightleftharpoons C_2H_4 + H + M$	1.70×10^{-6}	0.00	140	[99]

The thermal decomposition of methyl iodide is initiated by C-I bond fission ($R_{5.8}$). The rate coefficient for this reaction has been deduced from the I ARAS results of this study (see section 0). Methyl radicals can decompose to methylene and a H atom ($R_{5.9}$), or recombine forming either ethane ($R_{5.17}$) or an ethyl radical and a H atom ($R_{5.18}$). Rapid decomposition of ethyl radicals leads to the formation of ethylene and H atoms ($R_{5.19}$). Rate coefficients for these reactions were adopted from Baulch et al. [99].

Due to the small concentrations of ethane and ethylene, their decomposition reactions are of minor importance in the temperature range investigated. Also, the influence of the hydrogen iodine reactions ($R_{5.6}$) and ($R_{5.10}$) to ($R_{5.13}$) was found to be negligible. Thus, these reactions are not included in the mechanism.

5.5 Reinterpretation of the Ethyl Iodide Experiments

The influence of the rate coefficient for reaction ($R_{5.1}$) on I ARAS calibration curves is illustrated in figure 5.11. Reducing the rate coefficient from the original value to the value deduced from the experiments in this work, leads to a flattening of the calibration curves. The agreement of the calibration curves with the results of the maximum absorption experiments significantly improves. The same effect can be noted for calibration curves of the vertical I ARAS experiment.

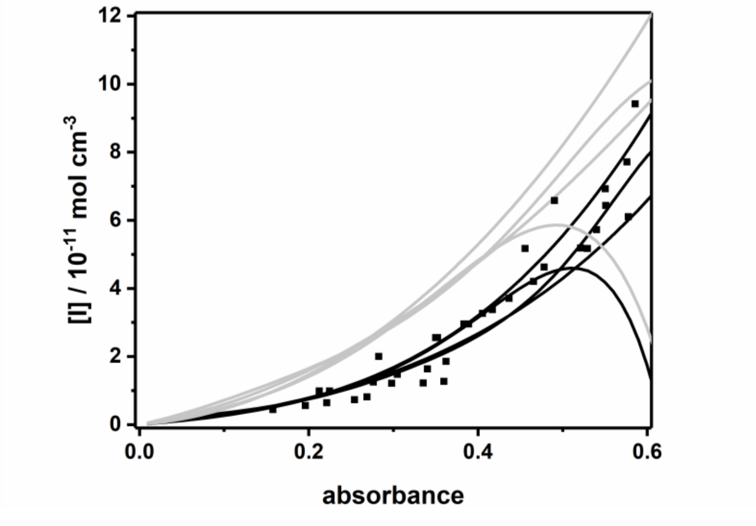

Figure 5.11: Influence of the updated rate coefficient for ($R_{5.8}$) on I ARAS calibration curves from methyl iodide experiments. Black: Calibration with rate coefficient determined in section 0. Grey: Calibration curves obtained with the original mechanism by T. Bentz [75] (table 5.2). Black squares: Results of maximal absorbance experiments on methyl iodide mixtures.

I atom concentration-time profiles deduced with the new calibration curves are depicted in figure 5.12. The improved agreement of simulated and measured concentration-time profiles for both detection setups becomes obvious in comparison with figure 5.2.

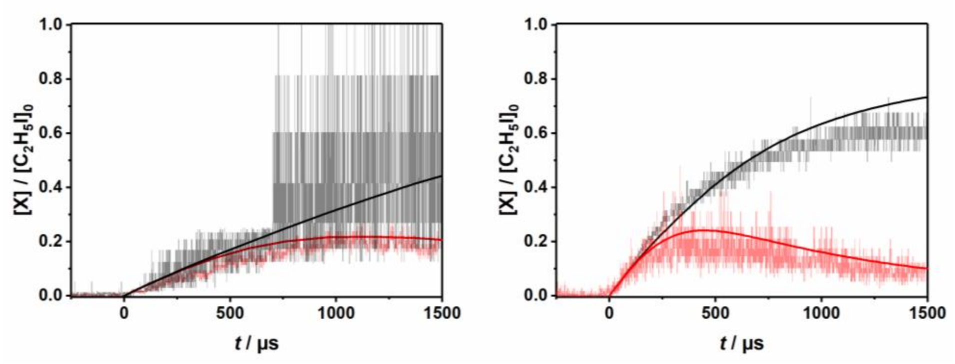

Figure 5.12: Comparison of simulated and measured relative concentration-time profiles for H (red) and I atoms (black). Simulated mechanism: Varga et al. [65] (table 5.1). Experiments: $T = 970$ K, $p = 1.7$ bar, $[C_2H_5I]_0 = 5.1 \times 10^{-11}$ mol cm^{-3}, $[Ar]_0 = 2.2 \times 10^{-5}$ mol cm^{-3}, horizontal H ARAS, vertical I ARAS (left panel). $T = 1012$ K, $p = 1.2$ bar, $[C_2H_5I]_0 = 1.2 \times 10^{-10}$ mol cm^{-3}, $[Ar]_0 = 1.4 \times 10^{-5}$ mol cm^{-3}, horizontal I ARAS, vertical H ARAS (right panel).

Branching ratios were directly determined from I atom concentrations at long reaction times. Due to the lower signal-to-noise ratio of the I atom concentration-time profiles measured with the vertical I ARAS setup only results of horizontal I ARAS experiments were used. At temperatures below 1100 K, the I atom concentrations did not reach a constant value within the measurement time. Hence, only experiments at temperatures above 1100 K were interpreted.

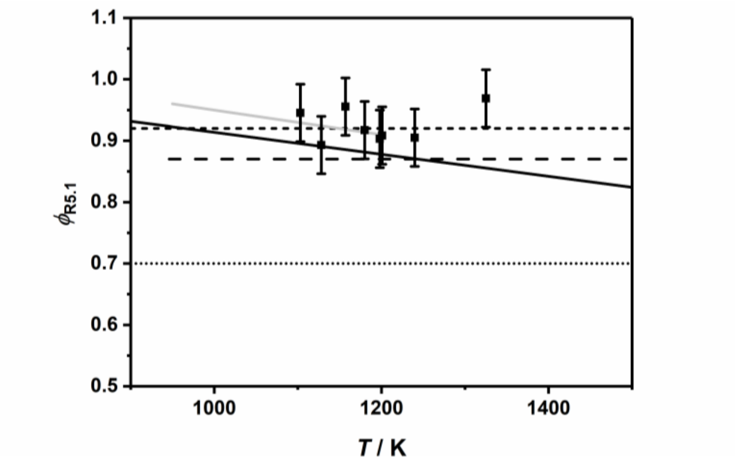

Figure 5.13: Branching ratios for the two initial reaction steps ($R_{5.1}$) and ($R_{5.4}$) in the thermal decomposition of ethyl iodide.Solid line: Varga et al. [65] , dashed line: Kumaran et al. [58], densely dashed line: Miyoshi et al. [72], densely dotted line: Weber et al. [66], grey line: I atom yield from T. Bentz [75]. Black squares: results of this work.

The experimentally determined branching ratios are in good agreement with the I atom yields determined by T.Bentz [75]. However, they are slightly higher than the ones deduced by Varga et al. [65]. This is unexpected, as the kinetic mechanism published by Varga et al. [65] adequately predicts the H- and I ARAS results of this work. It indicates that not only the two competing reaction channels ($R_{5.1}$) and ($R_{5.4}$) have an impact on I atom concentrations.

This hypothesis is supported by the results of a time-dependent sensitivity analysis for I atoms (see figure 5.14).Apart of the initial reaction channels ($R_{5.1}$), ($R_{5.2}$) and ($R_{5.4}$), the reaction of hydrogen iodide with H atoms ($R_{5.6}$) has a non-negligible influence on I atom concentrations. This reaction leads to a depletion of the reaction product of the molecular elimination channel ($R_{5.12}$), whilst increasing the concentration of I atoms in the system. Thereby, reaction ($R_{5.6}$) has a direct influence on the measured I atom yield. The resulting I atom concentrations are higher than expected from the ratio of the rate coefficients for reactions ($R_{5.1}$) and ($R_{5.4}$).

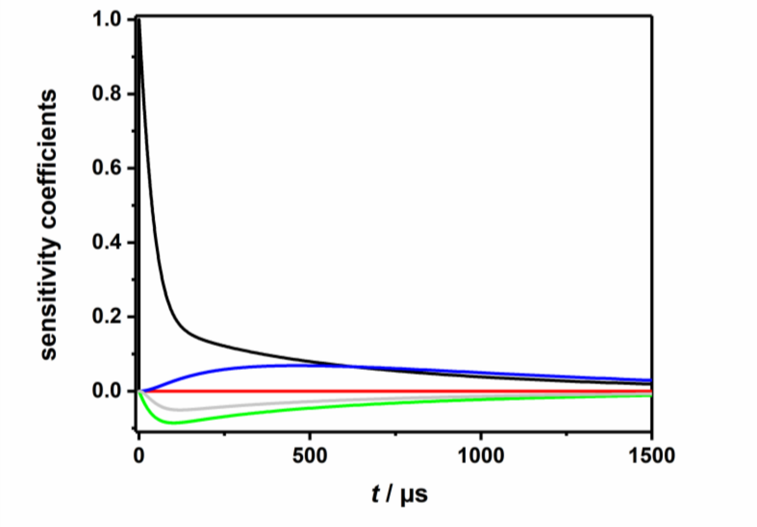

Figure 5.14: Time-dependent sensitivity analysis for I atoms in the mechanism by Varga et al. [65]. Reactions: black: ($R_{5.1}$), red: ($R_{5.2}$), green: ($R_{5.4}$), blue: ($R_{5.6}$), grey: ($R_{5.7}$). Experimental conditions: T = 1180 K, p = 1.62 bar, $[C_2H_5I]_0 = 6.1 \times 10^{-11}$ mol cm^{-3}, $[Ar]_0 = 1.5 \times 10^{-5}$ mol cm^{-3}.

5.6 Conclusions

In this chapter, the pyrolysis of ethyl iodide was investigated as a first trial of the new dual ARAS setup. Branching ratios for the two initial reaction channels, C-I bond fission ($R_{5.1}$) and molecular HI elimination ($R_{5.4}$), were determined and compared to values from earlier studies. Reaction channels influencing the total I atom yield were discussed.

Assuming that I and H atom concentrations at short reaction times have to be equal, possible errors in the calibration procedure of the I ARAS experiments were elucidated. In consequence, the thermal decomposition of methyl iodide was revaluated. The updated rate coefficient for the C-I bond fission in methyl iodide leads to a very good agreement of simulations and experimental profiles for the ethyl iodide measurements.

Disadvantages of the dual ARAS setup were illustrated. The low fraction of iodine atomic resonance radiation of the total radiation emitted by the I ARAS lamp leads to low maximum absorbances in the experiments. Therefore, only highly dilute mixtures with final concentrations below 4×10^{-11} mol cm^{-3} can be investigated. If the investigated species contains one iodine atom, this corresponds to mole fractions between 0.5 and 2.0 ppm reactant in bath gas for experiments at 1 to 2 bar. In combination with H ARAS as the second detection setup, this should not be an issue due to the high sensitivity of H ARAS. Nonetheless, low absorbances lead to higher errors in the absolute concentrations determined. Consequently, options to increase the measurable absorbances should be discussed. One approach would be the insertion of a narrow band pass VUV filter with a centre wavelength of 183 nm into the optical pathway. However, this would also lead to a loss in intensity as observed for the vertical H ARAS setup (compare section 4.3.1). It should be tolerable though, as no additional filter setup is required for I ARAS.

Increasing the fraction of resonance radiation would also improve the signal-to-noise ratio of the recorded concentration-time profiles. Low resonance radiation fractions lead to steeper calibration curves. In consequence, small variations in the absorbance values result in significant variations in the absolute concentrations.

The main application of the dual ARAS setup will be the investigation of the decomposition of hydrocarbon radicals and their halogenated precursor molecules. The halogen ARAS will be employed to track the concentration of the radical species to be investigated. At high temperatures, when precursor molecules completely decompose on a short timescale, information about the concentration of the radical species will be deduced from the initial branching ratio (bond fission vs. molecular elimination). At low temperatures, where the precursor molecule might not completely decompose, this information can be gained directly form the measured concentration-time profiles. I ARAS measurements can be used for both approaches, as long as reactant concentrations are sufficiently low. For a precise determination of branching ratios, the work with a horizontal I ARAS setup has to be preferred due to the better signal to noise ratios.

6 Thermal Decomposition of Furan and its Methyl Substituted Derivatives

6.1 Introduction

2,5-dimethylfuran (2,5-DMF) has often been discussed as a second generation biofuel. With its low water solubility and its high energy density and research octane number [100] it exhibits desirable properties. However, it shows a higher sooting tendency [101, 102] and an increased formation of (potentially hazardous) pollutants [103]. Efforts were made to understand the combustion behaviour of 2,5-DMF in lab scale experiments but also under engine conditions [104-108]. Several mechanisms were developed to appropriately predict product yields, laminar flame speeds, ignition delay times, flame instabilities and other combustion characteristics. Information on the initial steps in 2,5-DMF combustion were mostly deduced from extensive ab initio theoretical calculations [109, 110].

In the combustion and pyrolysis of 2,5-DMF, furan and 2-methylfuran (2-MF) are formed. Hence, to obtain a thorough understanding of 2,5-DMF chemistry, the reactions of the two smaller derivatives have to be known accurately. Although 2-MF and furan [105, 107] also show a promising behaviour in engine tests, their toxicity and carcinogenicity make a wider application unlikely.

Due to the absence of oxygen, pyrolytic processes are dominated by reactions of H atoms. Therefore, elucidating the formation of H atoms at short reaction times, gives crucial information about the initial reaction pathways. These are likely to be unimolecular bond fission reactions, if reactant concentrations are sufficiently low.

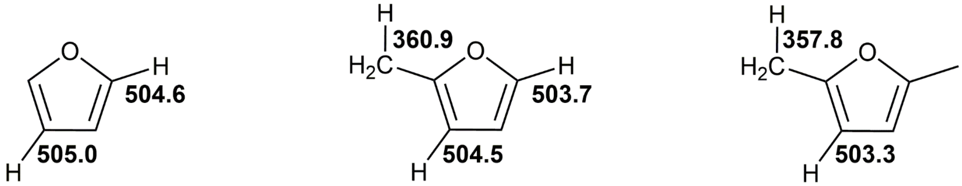

Figure 6.1: Bond dissociation energies of representative C-H bonds in furan, 2-MF and 2,5-DMF in kJ mol^{-1} [111].

The rate of bond fission reactions strongly depends on the bond dissociation energy of the breaking bonds. In 2009, Simmie and Curran [111] published bond dissociation energies for C-C and C-H bonds in different alkyl furans. The C-H bonds in furan and its methyl substituted derivatives can be divided into two groups: those in the methyl group(s) and those of the ring carbon atoms. Bond dissociation energies of C_{ring}-H bonds account to approximately 504 kJ mol^{-1} and are significantly higher than the ones of the C-H bonds in the methyl group(s) (compare figure 6.1). In consequence, the formation of H atoms from 2,5-DMF and 2-MF will most likely proceed by cleavage of a C-H bond in a methyl group. For furan, a direct formation of H atoms is highly improbable.

This chapter aims at a better understanding of the initial steps in the pyrolysis of furan, 2-MF and 2,5-DMF. In section 6.2 an overview of existing mechanisms for the oxidation and pyrolysis of furan derivatives is given. Common features are emphasised, and the choice of the mechanism discussed in this work is elucidated. Sections 6.3 and 6.4 focus on furan and 2-MF respectively. For introduction, the literature is reviewed with special focus on the initial reaction steps under pyrolytic conditions. After a brief description of the experiment, the results of this work are displayed. Changes to the original mechanism are discussed in detail. To close these subsections, the initial reaction pathways under the experimental conditions of this work are pointed out. Section 0 is concerned with the pyrolysis of the third derivative, 2,5-DMF, and thereby refers to the PhD thesis of P. Friese [112]. In section 6.6, the recently published updated version of the mechanism considered in this work is briefly discussed. As conclusion, trends in the formation of H atoms and the initial reaction steps under pyrolytic conditions are summarized.

6.2 Literatur Overview and Choice of Mechanism

In 1991, Organ and Mackie [113] investigated the pyrolysis of furan behind reflected shock waves at temperatures between 1100 and 1700 K and pressures around 20 bar. Time-resolved IR laser absorption measurements were performed to monitor the decomposition behaviour of furan. In addition, product yields were extracted from single pulse experiments with GC-FID, GC-TCD and FT-IR as detection methods. To explain their findings the authors developed a kinetic scheme consisting of 46 reactions and 30 species.

Lifshitz et al. [114] proposed a mechanism (100 reactions, 36 species) for the thermal decomposition of 2-MF. Rate coefficients for the initial steps were extracted from the results of a single pulse shock tube study (T = 1100 – 1400 K, p = 2 – 3 bar) with GC-FID and GC-MS. Additionally to 2-MF and the bath gas argon, the mixtures contained small quantities of 1,1,1-trifluoroethane which served as a ‘chemical thermometer’ to determine the temperature in the experiments. However, in 2013, Sirjean et al. [115] reviewed the rate coefficient for the thermal decomposition of 1,1,1-trifluoroethane employed by Lifshitz et al. [114]. Based on quantum chemical calculations, they found a rate coefficient a factor 3.8 smaller than the original one. With the updated coefficient, they recalculated the temperatures for the experiments by Lifshitz et al. [114] attaining temperatures between 20 to 90 K lower than in the original study.

A year later, in 1998, Lifshitz et al. [116] published a mechanism (181 reactions, 50 species) for the thermal decomposition of 2,5-DMF based on similar experiments. In this model, the 2-MF mechanism [114] was incorporated in a slightly modified version.

In 2000, Sendt et al. [117] studied the initial steps of furan pyrolysis by ab initio quantum chemical methods. The calculated rate coefficients were implemented into a kinetic scheme (82 reactions, 35 species) and the experimental results of Organ and Mackie [113] were simulated.

Tian et al. [118] conducted experiments on premixed furan/oxygen/argon flames at low pressures (p ~ 45 mbar). Mole fraction profiles of different species (reactant, intermediate and product) were obtained by SVUV-PIMS and MBMS. The developed model (1368 reactions, 206 species) is a combination of an earlier mechanism for the oxidation of toluene [119] and a primary and secondary mechanism for the oxidation of furan. Rate coefficients for the initial reaction steps were partly estimated, partly calculated, based on CBS-QB3 level quantum chemical calculations, and partly adopted from Sendt et al. [117]. To account for pressure effects, the latter were extrapolated to the low pressure flame conditions of the experiments. However, for simulations of the pyrolysis results by Organ and Mackie [113] and Fulle et al. [120], the high-pressure coefficients were used. A reasonable good agreement of experimental and simulated profiles was found.

2013 Sirjean et al. [115] developed a mechanism (1459 reactions, 294 species) to describe both pyrolysis and oxidation of 2,5-DMF. This mechanism consists of a reaction basis for toluene [121], the C0-C2 basis proposed by Curran et al. [122] and a 2-MF submechanism. Rate coefficients for reactions of 2-MF were estimated from the analogue reactions of 2,5-DMF. To complete the mechanism, parts of the furan model by Tian et al. [118] were adopted. Rate coefficients for most 2,5-DMF reactions have been taken from a theoretical study on its unimolecular decomposition also published in 2013 [109]. For validation, the authors measured ignition delay times in a shock tube (T = 1300 – 1831 K, p = 1 bar, 4 bar). In addition, the experimental results by Lifhitz et al. [116] were simulated.

Somers et al. [123] conducted experiments on the oxidation and pyrolysis of 2,5-DMF. Oxidation characteristics (e.g ignition delay times, species profiles, laminar burning velocities) were measured with three different experimental facilities (shock tube, jet-stirred reactor, flat burner). To explain the experimental results, a kinetic mechanism (2768 reactions, 545 species) was developed. Rate coefficients for the reactions of 2,5-DMF (decomposition and reactions with radicals) were mainly adopted from the theoretical studies by Simmie and Metcalfe [110] and Sirjean and Fournet [109, 124].

In a different study, Somers et al. [125] measured ignition delay times and laminar burning velocities of 2-MF mixtures with different equivalence ratios. A mechanism (2059 reactions, 391 species) consisting of several literature mechanisms and submechanisms (furan: [117, 118], aromatics: [126], C0-C4:[127-130]) was proposed. Rate coefficients for the initial reactions of 2-MF were calculated based on quantum chemical calculations. The only exceptions are the rate coefficients for the abstraction of a H atom from the methyl group by hydroxyl and methyl radicals. These were estimated in analogy to similar reactions of 2,5-DMF [110].

In the following years, two further mechanisms for 2,5-DMF were published. Cheng et al. [131] used SVUV-PIMS to measure concentration profiles in flow-reactor pyrolysis experiments. Measurements were performed at different pressures ($p \sim 40$ mbar, 200 mbar and 1013 mbar) and temperatures between 780 and 1470 K. A kinetic scheme (1173 reactions, 285 species) consisting of three submechanisms (C0-C4, aromatics, 2,5-DMF) was developed. For the DMF part, reactions from the mechanisms by Sirjean et al. [115] (2,5-DMF), Somers et al. [125] (2-MF) and Tian et al. [119] (furan) were combined. The mechanism was additionally validated against the experimental results of Lifshitz et al. [116], Somers et al. [123] and Djokic et al. [132]. Alexandrino et al. [133] utilized three different flow reactor setups to investigate the oxidation and pyrolysis of 2,5-DMF. The kinetic scheme of their study (1314 reactions, 255 species) incorporates parts of the 2,5-DMF mechanism by Sirjean et al. [115].

In 2014 Liu et al. published one comprehensive mechanism to describe the oxidation behaviour of all three furan derivatives. In a series of three papers [4-6], measurements on stoichiometric and fuel-rich laminar premixed low-pressure flames ($p \sim 25$ mbar, 55 mbar) of furan, 2-MF and 2,5-DMF with EI-MBMS-TOF, GC-FID and GC-TCD are reported. The developed mechanism (1472 reactions, 305 species) has a hierarchical structure and consist of three parts:

- The 2,5-DMF mechanism published by Sirjean et al. [115] including submechanisms for 2-MF and furan oxidation (see discussion above).
- The Nancy reaction base for C_n species ($n > 2$) [121, 134, 135].
- The C0-C2 base mechanism published by Curran [122].

To best describe their experimental results, Liu et al. [4] extended the submechanism for furan by two additional decomposition channels for dihydrofuryl radicals. Tran et al. [5] modified the 2-MF part by including another pathway for the reaction ‘2-MF + H’. The 2,5-DMF part remained unchanged.

Until now, two extended versions of the model by Liu et al. [4-6] have been published. In 2015, Tran et al. [102] reported further experiments on low-pressure flames ($p \sim 40$ mbar) of 2-MF and 2,5-DMF under fuel-rich conditions. GC-FID, GC-TCD and GC-MS were employed to investigate the formation of aromatics and polycyclic aromatic hydrocarbons (PAHs). The original mechanism [4-6] was extended to include reactions of C8-species, ethylbenzene and the formation of PAHs up to C16. 2017 Tran et al. [103] presented new flow-reactor measurements on the three furan derivatives at temperatures between 730 and 1170 K and pressures around 1 bar. Species were detected by EI-MBMS. The mechanism published in 2015 [102] was refined by including calculated rate coefficients for important reactions identified by sensitivity and rate of production analysis.

Of all mechanisms, only the one by Liu et al. [4-6] is aimed at a description of the combustion behaviour of all three furan derivatives. In this work, its suitability for the description of the pyrolysis of furan, 2-MF and 2,5-DMF will be discussed. Since the model was originally developed for experiments under low-pressure conditions, the high-pressure rate coefficients published by Sirjean et al. [115] have been used in the simulations, as recommended in the paper by Liu et al. [4]. Species are named in accordance with the nomenclature used in the original mechanism [4-6].

6.3 Furan

6.3.1 Initial Reaction Pathways in Furan Pyrolysis

The first investigation of furan pyrolysis was conducted by Grela et al. [136] in 1985. They measured product yields at temperatures between 1050 and 1270 K under very low pressure conditions ($p \sim 1.33 \times 10^{-3}$ mbar) by mass spectrometry. A one step unimolecular decomposition of furan to carbon monoxide and a C_3H_4 isomer was proposed. However, the two isomers propyne and allene could not be distinguished experimentally. Additionally, the authors determined a rate coefficient for the overall disappearance of furan. 2-MF and 2,5-DMF were also investigated.

Lifshitz et al., in addition to their mechanistic studies of 2-MF [114] and 2,5-DMF [116] pyrolysis (compare section 6.2), also investigated the thermal decomposition of furan [137] under the same conditions. Propyne, carbon monoxide and acetylene were identified as the main products. Comparing the ratios $[C_2H_2]_t$:$[p\text{-}C_3H_4]_t(T)$ from their furan experiments with the ones found for the thermal decomposition of propyne, they concluded that acetylene has to be formed directly from furan. Thus, the authors suggested an additional decomposition channel for furan leading to acetylene and ketene. However, they were not able to detect the latter.

1991 Organ and Mackie [113] succeeded in detecting ketene in the pyrolysis of furan. Based on thermochemical considerations, they suggested the formation of a biradical by C-O bond cleavage. This biradical can than decompose to carbon monoxide and a C_3H_4-isomer, ketene and acetylene or propargyl and formyl radicals.

Fulle et al. [120] studied the thermal decomposition of furan in a shock tube/TOF-MS experiment (T = 1300 – 1700 K, p = 233 – 333 mbar, 2 % furan in neon). Only propyne/allene, carbon monoxide, ketene and acetylene were detected. Form their results, the authors determined temperature dependent branching ratios for the two decomposition pathways discussed by Lifshitz et al. [137]. The radical formation channel suggested by Organ and Mackie [113] was not taken into account.

In 2009 Vasiliou et al. [138] examined the pyrolysis of furan in a turbulent flow reactor with PI-MS and IR spectroscopy for detection and measured, among other species, propargyl radicals. To identify the source of these radicals the authors performed additional experiments on mixtures of furan and d_3-propyne. From the peak ratio (41/40) in the mass spectra and the natural abundance of deuterium, they concluded that propargyl radicals are a primary product in furan pyrolysis.

The first theoretical study on furan pyrolysis was published in 1998. Liu et al. [139] calculated geometries and energies of equilibrium and transition state structures for the three reaction pathways leading to propyne and carbon monoxide, acetylene and ketene, and allene and carbon monoxide respectively. In analogy to isoxazole decomposition [140], the authors suggested the formation of carbenes as intermediates species. Two years later, Liu et al. [141] published a second paper discussing the biradical pathways proposed by Organ and Mackie [113]. They calculated barrier heights more than 10 kcal / mol higher than the ones derived from the experimental studies. Since calculated barrier heights for the carbene mechanism proposed in [139] were in line with the experimental values, the authors concluded that a carbene mediated mechanism is more feasible.

Sendt et al. [117] arrived at the same conclusions. In addition to potential energy surfaces, the authors also calculated rate coefficients. With these they were able to satisfactorily simulate the species profiles obtained by Organ and Mackie [113].

6.3.2 Experiments

To investigate the thermal decomposition of furan, a total of 36 experiments behind reflected shock waves were performed. H atom concentration-time profiles were measured by time-resolved H ARAS. The experiments covered temperatures between 1350 and 1900 K, and pressures between 0.7 and 1.2 bar. To cover a wide range of initial furan concentrations, four mixtures with mole fractions between 0.5 and 9.5 ppm furan in argon were used. The resulting initial concentrations of furan ranged from 2×10^{-11} to 9×10^{-11} mol cm^{-3}. H ARAS was calibrated with experiments on mixtures of N_2O and H_2 in argon as describe in section 2.2.3.

6.3.3 Mechanistic Considerations

In figure 6.2, measured H atom concentration-time profiles are compared to simulations based on the mechanism by Liu et al. [4-6]. Significant discrepancies are obvious. The experimental data is underpredicted at most times, especially for temperatures above 1600 K. Only for very short reaction times ($t < 30$ µs at $T = 1825$ K) are the experimental results satisfactorily described by the model.

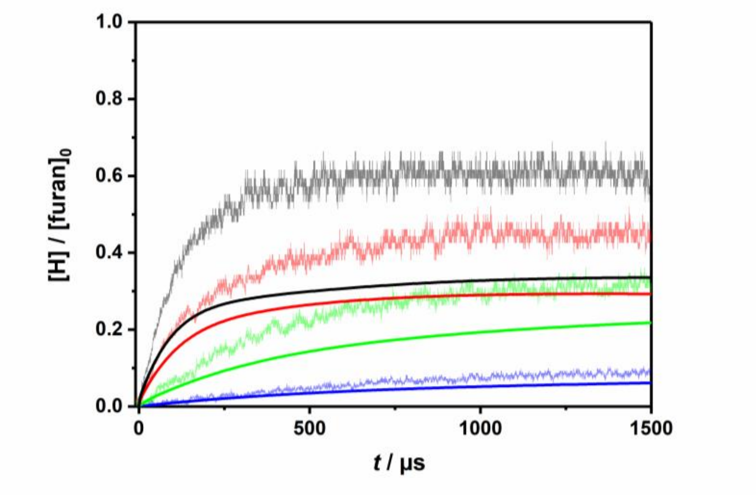

Figure 6.2: Comparison of experimental results to simulations with the mechanism by Liu et al. [4-6] (solid lines). Experimental conditions: T = 1540 K (blue), 1650 K (green), 1770 K (red), 1825 K (black), p ~ 1 bar.

To identify the most influencing reactions, a sensitivity analysis for H atoms was performed. Results for the temperatures depicted in figure 6.2 after a reaction time of 50 µs are presented below. An overview of reactions with the highest sensitivities, the corresponding rate coefficients and the associated literature is given in table 6.1.

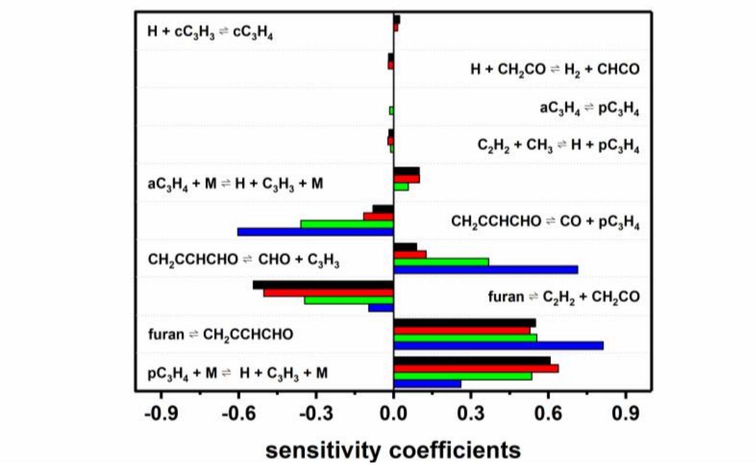

Figure 6.3: Local sensitivity analysis for H atoms of the mechanism by Liu et al. [4-6] at *t* ~ 50 µs. Experimental conditions: *T* = 1540 K (blue), 1650 K (green), 1770 K (red), 1825 K (black), *p* ~ 1 bar.

Table 6.1: Reactions with the highest sensitivities for H atoms in the mechanism by Liu et al. [4-6] and the corresponding rate coefficients. Parameterization: $k(T) = A \times (T/\mathrm{K})^n \times \exp(-E_\mathrm{a}/\mathrm{R}T)$. Units: s^{-1}, kJ, mol^{-1}, cm^3, K.

	reaction	A	n	E_a	ref.
($R_{6.1}$)	$pC_3H_4 + M \rightleftharpoons C_3H_3 + H + M$	4.70×10^{18}	0.000	335	[142]
($R_{6.2}$)	furan $\rightleftharpoons$ $CH_2CCHCHO$	4.58×10^{12}	0.416	297	[118]
($R_{6.3}$)	furan $\rightleftharpoons$ $C_2H_2 + CH_2CO$	1.82×10^{14}	0.534	262	[118]
($R_{6.4}$)	$CH_2CCHCHO \rightleftharpoons CHO + C_3H_3$	7.90×10^{14}	0.000	293	[117, 118]
($R_{6.5}$)	$CH_2CCHCHO \rightleftharpoons CO + pC_3H_4$	6.80×10^{14}	0.419	185	[118]
($R_{6.6}$)	$aC_3H_4 + M \rightleftharpoons C_3H_3 + H + M$	2.00×10^{18}	0.000	335	[142]

Reactions ($R_{6.2}$) to ($R_{6.4}$) are the initial reaction steps in furan consumption under pyrolytic conditions. Although H atoms are not taking part in these steps, their influence on H atom concentration, indicated by the sensitivity analysis, is considerably high. Tian et al. [118] adopted the rate coefficient for reaction ($R_{6.4}$) from the publication by Sendt et al. [117]. The rate coefficients for reactions ($R_{6.2}$), ($R_{6.3}$) and ($R_{6.5}$) were calculated by TST based on CBS-QB3 level theoretical calculations.

In this work, the original rate coefficients for reactions ($R_{6.2}$), ($R_{6.3}$) and ($R_{6.5}$) by Sendt et al. [117] have been adopted to obtain a consistent set of rate coefficients. These were originally optimized for description of the experimental results obtained by Organ and Mackie [113] at pressures around 20 bar. Fulle et al. [120] argued that the reaction rates of the initial furan decomposition steps ought to be close to their high-pressure limit under the experimental conditions of the studies by Lifshitz et al. [137] and Organ and Mackie [113]. Tian et al. [118] received a good agreement of simulations and experimental results, although both, high and low pressure rate coefficients for the initial reaction steps, are implemented in their model. Hence, pressure effects should be minor under the experimental conditions of this work, and the adoption of high-pressure rate coefficients should be justified.

For the thermal decomposition of propyne ($R_{6.1}$) and allene ($R_{6.6}$), Liu et al. [4-6] accepted rate coefficients from a study by Hidaka et al. [142]. These were extracted from IR spectroscopy experiments behind reflected shock waves at temperatures in the range 1200-1570 K and pressures between 1.7 and 2.6 bar. Initial reactant mole fractions were set to 4 % propyne and 1 %, 2 % or 4 % allene in argon respectively. In 2011 Giri et al. [143] published a H ARAS study on highly diluted propyne and allene mixtures (2 – 15 ppm reactant in argon) behind reflected shock waves. Rate coefficients were directly deduced from the initial slope of the H atom concentration-time profiles recorded. Unlike Hidaka et al. [142], Giri et al. [143] found no difference in the decomposition rate coefficients for allene and propyne. As the experimental conditions in the study of Giri et al. [143] well match the conditions in this work, their bimolecular rate coefficient has been adopted for reactions ($R_{6.1}$) and ($R_{6.6}$).

Although the unimolecular decomposition of propargyl radicals was not identified as an important reaction in the sensitivity analysis, it will be discussed here since relatively high mole fractions of propargyl radicals are predicted by the model. In the original mechanism, the C-H bond fission reaction of propargyl radicals is implemented in the form of its reverse reaction, the recombination of propadienylidene radicals (C_3H_2) with H atoms.

Table 6.2: Rate coefficient for the recombination reaction 'C_3H_2 + H' as implemented by Liu et al. [4-6] and calculated rate coefficient for the reverse reaction. Parameterization: $k(T) = A \times (T/\mathrm{K})^n \times \exp(-E_a/RT)$. Units: s^{-1}, kJ, mol^{-1}, cm^3, K.

	reaction	A	n	E_a	ref.
($R_{6.7}$)	$C_3H_2 + H \rightleftharpoons C_3H_3$	1.00×10^{14}	0.000	0	[4-6]
	$C_3H_3 \rightleftharpoons C_3H_2 + H$	1.82×10^{14}	0.534	262	calc.

Reactions of the propargyl radical under pyrolytic conditions were investigated by Scherer et al. [61]. The authors performed shock tube experiments at pressures between 1.5 and 2.2 bar and temperatures between 1400 and 2000 K, detecting H atoms by H ARAS. 3-iodo-propyne was employed as propargyl radical precursor. No pressure dependence was reported. In this work, the rate coefficient for the unimolecular decomposition of propargyl radicals determined in their study has been adopted for the backward reaction of ($R_{6.7}$). For the forward reaction of ($R_{6.7}$), the rate coefficient calculated by Harding et al. [144] has been used.

In figure 6.4, simulations based on the modified and the original mechanism are displayed. Measured concentration-time profiles are well predicted by the new model. For elevated temperatures, slight discrepancies can be noted for longer reaction times. Nevertheless, the qualitative and quantitative behaviour are described reasonably well.

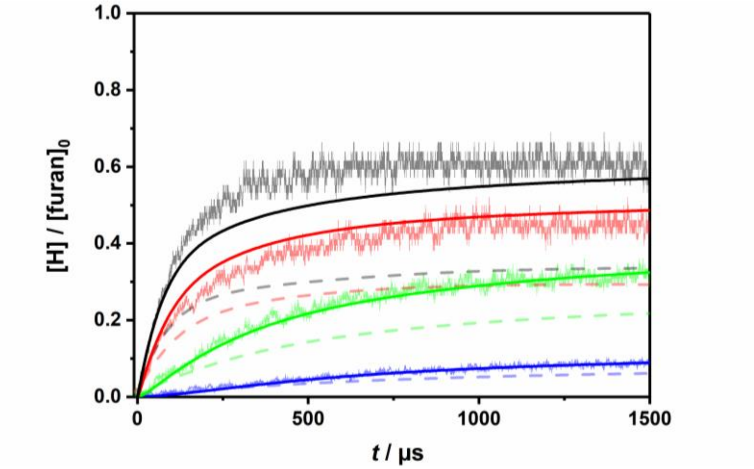

Figure 6.4: Comparison of experimental results to simulations with the modified mechanism (solid lines). Transparent dashed lines: Simulations with the original mechanism by Liu et al. [4-6]. Experimental conditions: T = 1540 K (blue), 1650 K (green), 1770 K (red), 1825 K (black), p ~ 1 bar.

6.3.4 Formation of H atoms in the Pyrolysis of Furan

Due to the high bond dissociation energies of the C_{ring}–H bonds in furan (~ 503 kJ mol^{-1} [111]), a direct release of H atoms from the reactant is highly improbable. Consequently, H atoms at short reaction times will be formed mainly by decomposition of the primary products, propyne (pC_3H_4), propargyl (C_3H_3) and formyl radicals (CHO). Acetylene (C_2H_2) is stable under the experimental conditions of this work and therefore does not contribute to the H atom yield. Ketene decomposition leads to methylene and carbon monoxide. H atoms are not formed directly from ketene.

In figure 6.5 rate coefficients for reactions ($R_{6.1}$) to ($R_{6.7}$) implemented in the modified mechanism are compared to rate coefficients for the reaction

$$\text{furan} \rightarrow \text{products} + \text{H} \qquad (R_{6.8})$$

determined from the initial slope of the measured concentration-time profiles (compare section 2.3.4). The smallest rate coefficients are the ones for the decomposition of propyne/allene and propargyl radicals, which are in good agreement with the one for reaction ($R_{6.8}$). Reaction rates for the initial furan decomposition steps are significantly higher.

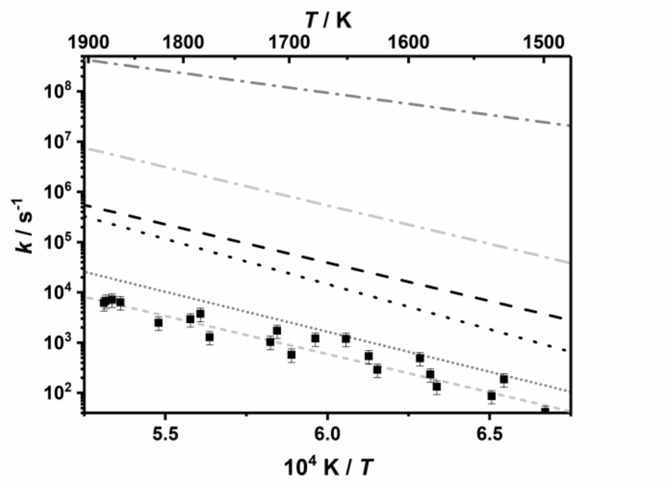

Figure 6.5: Rate coefficients for the reaction ‘furan → products + H’ ($R_{6.8}$) deduced from the initial slope of the measured H atom concentration-time profiles (black squares, error bars: 30 %) and rate coefficients for the main initial decomposition pathways (lines): dash-dot (dark grey):($R_{6.5}$), dash-dot (light grey):($R_{6.4}$), dashed:(R6.2), dotted:($R_{6.3}$), densely dotted:($R_{6.1}$), densely dashed: ‘C_3H_3 → C_3H_2 + H’ (reverse ($R_{6.7}$)).

This indicates that the overall formation of H atoms is indeed determined by the decomposition of the primary products rather than by the decomposition of the reactant itself. A reaction flux analysis for short reaction times can give more information.

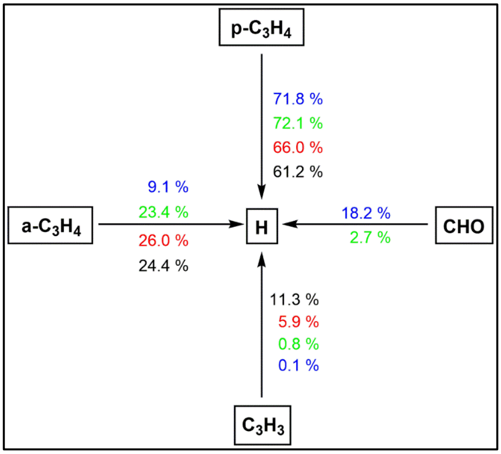

Figure 6.6: Reaction flux analysis for the formation of H atoms at t ~ 50 µs. Experimental conditions: T = 1540 K (blue), 1650 K (green), 1770 K (red), 1825 K (black), p ~ 1 bar.

H atoms are mainly formed from propyne. A second important source is allene, which is solely formed by isomerization of propyne. Toward higher temperatures, the influence of propargyl radicals in the formation of H atoms increases. Formyl radical decomposition only plays a role at low temperatures. Formation of H atoms by C-H bond fission in furan is negligible.

The reaction flux analysis for H atoms in the decomposition of furan (figure 6.7) gives a similar picture. Most H atoms from furan are transferred to 2,3-butadienale ($CH_2CCHCHO$). The reaction channel leading to acetylene and ketene only plays a minor role, although its importance increases with increasing temperature. 2,3-butadienale in turn mainly decomposes to propyne, which has been identified as the main source of H atoms. Apparently propargyl radicals are mostly formed by thermal decomposition of propyne and its isomers allene and cyclopropene. The radical channel leading from 2,3-butadienale to propargyl and formyl radicals is only of minor importance.

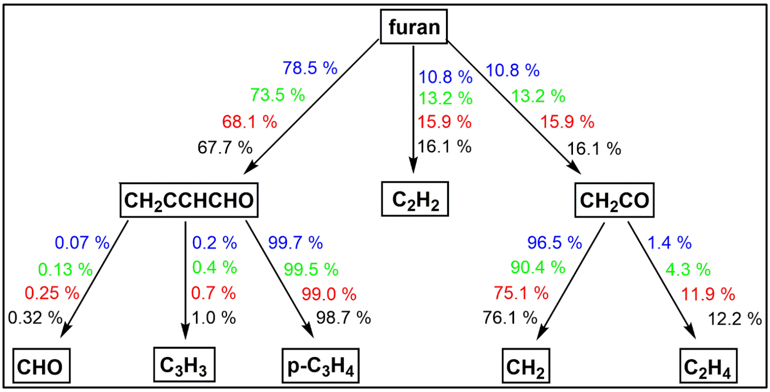
furan
78.5 %
73.5 %
68.1 %
67.7 %
10.8 %
13.2 %
15.9 %
16.1 %
10.8 %
13.2 %
15.9 %
16.1 %
CH2CCHCHO
C2H2
CH2CO
0.07 %
0.13 %
0.25 %
0.32 %
0.2 %
0.4 %
0.7 %
1.0 %
99.7 %
99.5 %
99.0 %
98.7 %
96.5 %
90.4 %
75.1 %
76.1 %
1.4 %
4.3 %
11.9 %
12.2 %
CHO
C3H3
p-C3H4
CH2
C2H4

Figure 6.7: Reaction flux analysis for H atoms in the decomposition of furan at t ~ 50 µs. Experimental conditions: T = 1540 K (blue), 1650 K (green), 1770 K (red), 1825 K (black), p ~ 1 bar.

6.4 2-Methylfuran (2-MF)

6.4.1 Initial Reaction Pathways in 2-MF Pyrolysis

Unlike for furan and 2,5-DMF, only a few studies have been focused on the initial reaction steps in the pyrolysis of 2-MF. The first discussion is found in the publication by Grela et al. [136], which was mentioned in section 6.3.1. In analogy to the reaction pathway suggested for furan, the authors proposed a unimolecular decomposition step yielding carbon monoxide and a C_4H_6-isomer.

Lifshitz et al. [114] stated that the loss of symmetry caused by the methyl group in 2-MF leads to more possible reaction channels compared to furan. In their mechanism, nine different decomposition steps for 2-MF are considered. Four of them lead to carbon monoxide and C_4H_6-isomers (1,2-butadiene, 1,3-butadiene, 1-butyne, 2-butyne). Of the remaining channels, two yield only molecular products (propyne and ketene or acetylene, ethene and carbon monoxide), whilst the other three are radical pathways. These are the C-H bond fission in the methyl group leading to the 2-furanylmethyl radical (furylCH_2) and a H atom, and the C-C and C-O bond fissions in the furan ring leading to acetyl and propargyl radicals or to formyl and C_4H_5 radicals.

In 2014, Somers et al. [145] published a quantum chemical study on the pyrolysis of 2-MF. Potential energy surfaces for different possible reaction pathways were calculated and rate coefficients were deduced by transition state theory, RRKM theory and master equation calculations. According to Somers et al. [145], the thermal decomposition of 2-MF mainly proceeds via carbene mediated ring-opening reactions. The C-H bond fission reaction was found to be of minor importance.

6.4.2 Experiments

To investigate the thermal decomposition of 2-MF, a total 43 experiments behind reflected shock waves were performed. H atom concentration-time profiles were measured by time-resolved H ARAS. The experiments covered temperatures between 1400 and 1900 K, and pressures between 0.8 and 1.2 bar. To cover a wide range of initial 2-MF concentrations, four mixtures with mole fractions between 0.9 and 10.1 ppm 2-MF in argon were used. The resulting initial concentrations of 2-MF ranged from 4×10^{-12} to 1×10^{-10} mol cm^{-3}. H ARAS was calibrated with experiments on mixtures of N_2O and H_2 in argon as described in section 2.2.3.

6.4.3 Mechanistic Considerations

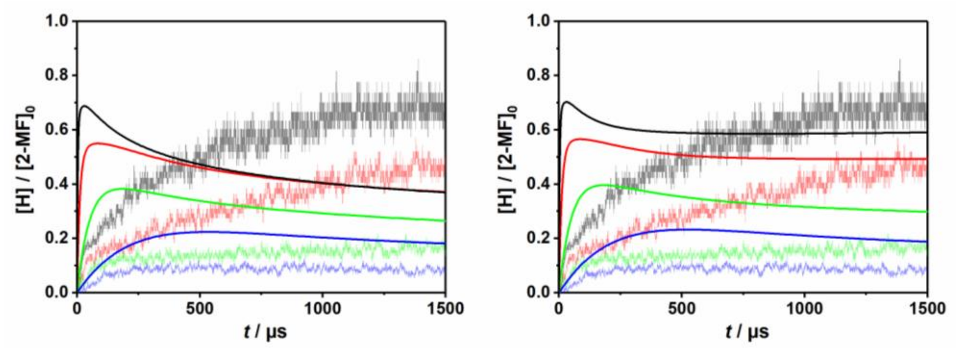

Figure 6.8: Comparison of experimental results to simulations (solid lines) with the mechanism by Liu et al. [4-6] (left) and the modified version of the model (section 6.3.3) (right). Experimental conditions: T = 1480 K (blue), 1580 K (green), 1690 K (red), 1790 K (black), p ~ 1 bar.

In figure 6.8 experimental results are compared to simulations of the original mechanism by Liu et al. [4-6] (left) and to simulations of the mechanism modified for the description of furan pyrolysis (section 6.3.3) (right). Neither of the mechanisms is able to predict the qualitative behaviour of the measured concentration-time profiles. For lower temperatures, H atom concentrations are overestimated at all times. At higher temperatures, the initial rise in H atom concentration is significantly overpredicted. However, for long reaction times, concentrations are predicted fairly well by the modified mechanism.

Simulated concentration-time profiles only differ for temperatures above 1600 K. Modifications implemented in section 6.3.3 mainly concerned rate coefficients for the unimolecular decomposition of propyne, allene and propargyl radicals. In 2-MF pyrolysis, these species are not formed directly from the primary products (compare section 6.4.1). At higher temperatures, the influence of consecutive reactions yielding propyne, allene and propargyl radicals increases and thus the effect of the modified rate coefficients is no longer negligible.

To identify the most influencing reactions, a sensitivity analysis for H atoms was performed. Results for the temperatures depicted in figure 6.8 after a reaction time of 30 µs are presented below. An overview of reactions with the highest sensitivities, the corresponding rate coefficients and the associated literature is given in table 6.3.

As for furan, only a small number of reactions exhibits a high influence on H atom concentrations at short reaction times. These reactions are the decomposition reactions of 2-MF (($R_{6.9}$) to ($R_{6.11}$)) and the primary products (($R_{6.12}$) and ($R_{6.12}$)) formed therein. In the mechanism by Liu et al. [4-6], rate coefficients for these reactions have been estimated in analogy with reactions of furan and 2,5-DMF.

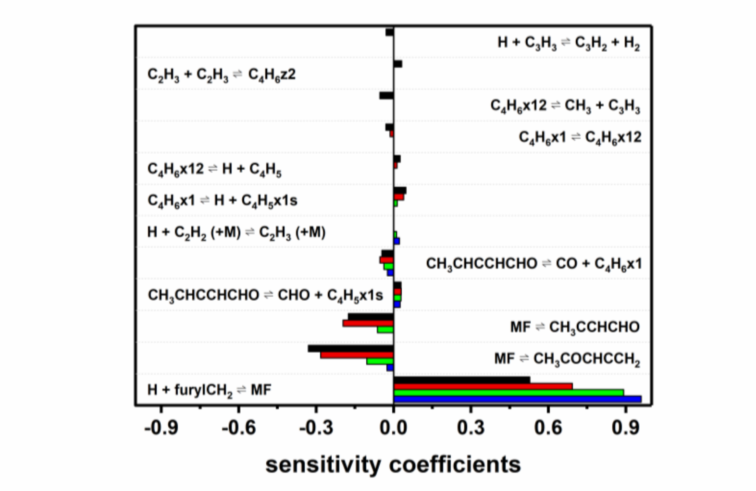

Figure 6.9: Local sensitivity analysis for H atoms in the modified mechanism of section 6.3.3 at *t* ~ 30 µs. Experimental conditions: *T* = 1480 K (blue), 1580 K (green), 1690 K (red), 1790 K (black), *p* ~ 1 bar.

Table 6.3: Reactions with the highest sensitivities for H atoms in the modified mechanism (section 6.3.3) and the corresponding rate coefficients. Parameterization: $k(T) = A \times (T/\mathrm{K})^n \times \exp(-E_a/RT)$. Units: s^{-1}, kJ, mol^{-1}, cm^3, K.

	reaction	A	n	*E*a	ref.
($R_{6.9}$)	H + furylCH$_2$ ⇌ MF	1.00×10^{14}	0.000	0	[4-6]
	MF ⇌ H + furylCH$_2$	4.88×10^{10}	0.515	355	calc.
($R_{6.10}$)	MF ⇌ $CH_3COCHCCH_2$	2.29×10^{12}	0.416	297	[4-6]
($R_{6.11}$)	MF ⇌ $CH_3CHCCHCHO$	2.46×10^{11}	0.659	288	[4-6]
($R_{6.12}$)	$CH_3CHCCHCHO$ ⇌ CHO + C_4H_5	7.90×10^{14}	0.000	293	[4-6]
($R_{6.13}$)	$CH_3CHCCHCHO$ ⇌ CO + C_4H_6x1	6.80×10^{11}	0.419	185	[4-6]

Somers et al. [145] calculated rate coefficients for different reaction steps in the pyrolysis of 2-MF. Additionally to the reactions in table 6.3, the authors considered the formation of an α-carbene at position C(5) (a(5)carbene) and its decomposition. Furthermore, two additional reaction channels for the decompositon of the primary product 3,4-pentadienone ($CH_3COCHCCH_2$) were suggested. In this work, the 1 bar rate coefficients for these reactions published by Somers et al. [145] were incorporated into the modified furan mechanism. Thermochemical data for the α-carbene was taken from Somers et al. [125]. The resulting changes in the simulated H atom concentration-time profiles are illustrated in figure 6.10.

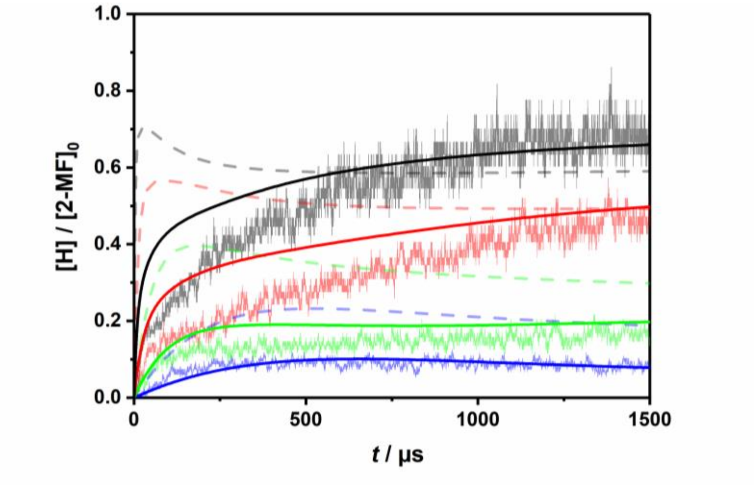

Figure 6.10: Comparison of experimental results to simulations with the modified mechanism (solid lines). Transparent dashed lines: Simulations with the mechanism of section 6.3.3. Experimental conditions: T = 1480 K (blue), 1580 K (green), 1690 K (red), 1790 K (black), p ~ 1 bar.

For low temperatures, the experimentally determined H atom concentrations are predicted reasonably well. However, at higher temperatures only the behaviour for long reaction times is described appropriately. For shorter reaction times, H atom concentrations are still overestimated.

In figure 6.11, the results of a time-resolved sensitivity analysis for H atoms are shown. Only reactions which exhibit significant sensitivity coefficients are included. These are the initial reactions in the decomposition of 2-MF and the newly implemented reactions discussed in this section.

At 1480 K, simulated H atom concentration-time profiles are predominantly influenced by the C-H bond fission reaction ($R_{6.9}$). As the measured concentration-time profile is appropriately predicted by the model, no further changes to the rate coefficient for reaction ($R_{6.9}$) should be made. With rising temperature, the influence of the initial reactions decreases significantly with reaction time. H atom concentrations at long reaction times are mainly determined by a different set of reactions. For temperatures above 1500 K, these are well predicted by the modified model, indicating that the consecutive chemistry in 2-MF pyrolysis is adequately implemented therein. To further improve the model, the 1 bar rate coefficients for reactions ($R_{6.10}$) to ($R_{6.13}$), and the newly integrated reactions, were substituted by the corresponding high-pressure coefficients by Somers et al. [145]. If pressure effects on the rate coefficients for the initial reactions of furan are small (compare section 6.3.3), they should also be small for the reactions of 2-MF.

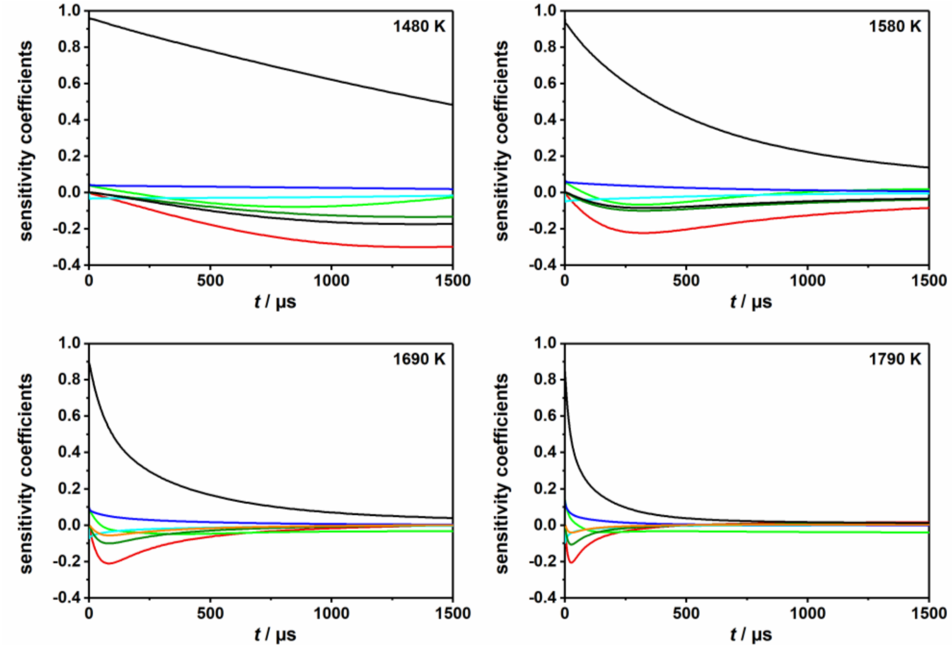

Figure 6.11: Time-resolved sensitivity analysis for H atoms in the modified mechanism. Reactions: reverse ($R_{6.9}$) (black), ($R_{6.10}$) (red), ($R_{6.11}$) (light green), ($R_{6.12}$) (blue), ($R_{6.13}$) (light blue), 'α-(5)Carbene $\rightleftharpoons$ pC_3H_4 + CH_2CO' (dark green), '$CH_3COCHCCH_2$ $\rightleftharpoons$ pC_3H_4 + CH_2CO' (orange). Experimental conditions: T = 1480 K, 1580 K, 1690 K, 1790 K, p ~ 1 bar.

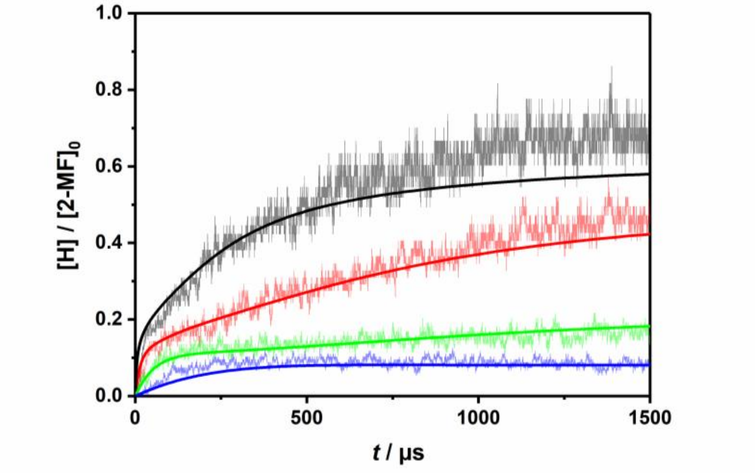

Figure 6.12: Comparison of experimental results to simulations with the modified mechanism (solid lines). Experimental conditions: T = 1480 K (blue), 1580 K (green), 1690 K (red), 1790 K (black), p ~ 1 bar.

The agreement of measured and simulated H atom concentration-time profiles significantly improved. For long reaction times and very high temperatures, H atom concentrations are still slightly underestimated. However, results for short reaction times are described accurately for all temperatures.

6.4.4 Formation of H Atoms in the Pyrolysis of 2-MF

H atoms in 2-MF can be divided in two groups: H atoms with bonds to ring C atoms and H atoms in the methyl group. Simmie et al. [111] calculated bond dissociation energies of ~ 361 kJ mol^{-1} for the C-H bonds in the methyl group and ~ 504 kJ mol^{-1} for the C(ring)-H bonds respectively. The latter are independent of the position of the C-atom in the ring and are close to the values for the C$_{ring}$-H bonds in furan.

For temperatures above 1500 K, measured H atom concentration-time profiles exhibit a kink at short reaction times (compare figure 6.12, figure 6.13). This feature can be explained by two processes of different velocity contributing to the total H atom concentration. For 2-MF these processes are the C-H bond fission reaction directly leading to H atoms and the ring-opening processes in which H atoms are produced by the decomposition of the products.

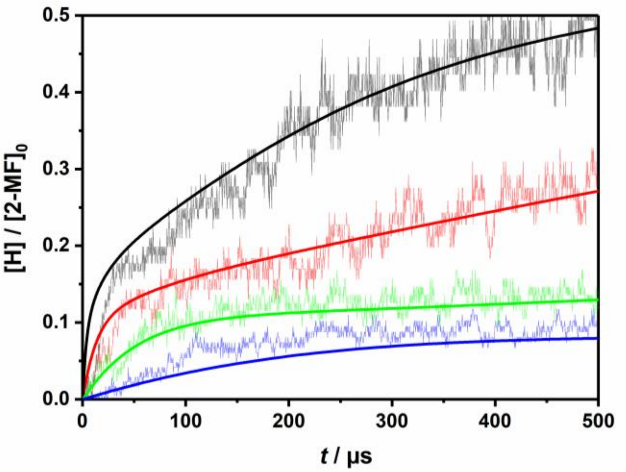

Figure 6.13: Kink at short reaction times. Simulations: solid lines. Experimental conditions: *T* = 1480 K (blue), 1580 K (green), 1690 K (red), 1790 K (black), *p* ~ 1 bar.

In figure 6.14, the dominating processes in the decomposition of 2-MF (A) and the formation of H atoms (B) are illustrated. Most H atoms in 2-MF are transferred to 3,4-pentadienone ($CH_3COCHCCH_2$) and the α-carbene. Apparently, C-H bond fission is only of minor importance for the consumption of 2-MF. On the contrary (compare figure 6.14(B)), H atoms at short reaction times are mostly formed directly from 2-MF. Vinyl and 1,3-butadien-1-yl (nC_4H_5) radicals originate from the decomposition of the 2-methyfuryl radical, which is the second product in the C-H bond fission of 2-MF. 1-butyne-3-yl radicals (C_4H_5-1s) are formed in the decomposition of 3,4-pentadienone. For long reaction times, H atom formation is dominated by the decomposition of the primary products of the ring-opening/carbene mediated processes (compare figure 6.15).

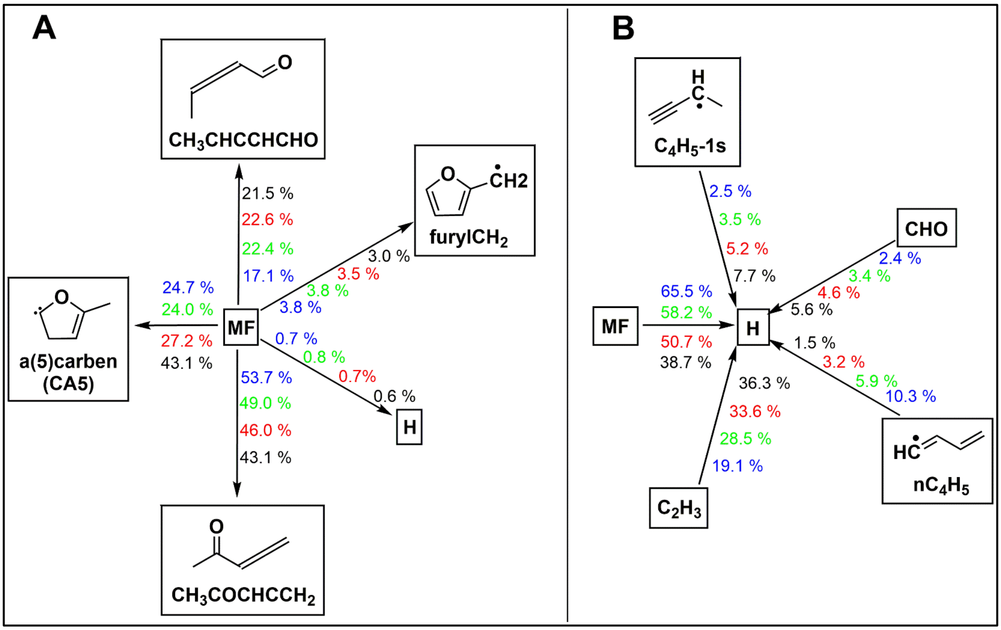
A
CH3CHCCHCHO
21.5 %
22.6 %
22.4 %
17.1 %
furylCH2
CH2
O
3.0 %
3.5 %
3.8 %
3.8 %
a(5)carben
(CA5)
24.7 %
24.0 %
27.2 %
43.1 %
MF
0.7 %
0.8 %
0.7%
0.6 %
H
53.7 %
49.0 %
46.0 %
43.1 %
CH3COCHCCH2
B
C4H5-1s
2.5 %
3.5 %
5.2 %
7.7 %
CHO
2.4 %
3.4 %
4.6 %
5.6 %
MF
65.5 %
58.2 %
50.7 %
38.7 %
H
1.5 %
3.2 %
5.9 %
10.3 %
36.3 %
33.6 %
28.5 %
19.1 %
C2H3
HC
nC4H5

Figure 6.14: Reaction flux analysis for H atoms in the decomposition of 2-MF (A) and in the production of H atoms (B) at *t* ~ 1 μs. Experimental conditions: *T* = 1480 K (blue), 1580 K (green), 1690 K (red), 1790 K (black), *p* ~ 1 bar.

By performing a reaction flux analysis at different reaction times, the time at which the C-H bond fission does not contribute to the formation of H atoms any longer could be identified. At 1690 K, 55 μs have to pass, whilst at 1790 K the C-H bond fission reaction only has an influence within the first 20 μs. These times correlate to the position of the kink in the recorded H atom concentration-time profiles (compare figure 6.13). At very short reaction times, H atoms are predominantly formed by C-H bond fission in 2-MF. As 2-MF is consumed the influence of the indirect H atom formation channels via the decomposition of ring-opening products increases. However, the production of H atoms is slower, since a number of intermediate reaction steps have to occur. Consequently, the slope of the recorded H atom concentration-time profiles decreases.

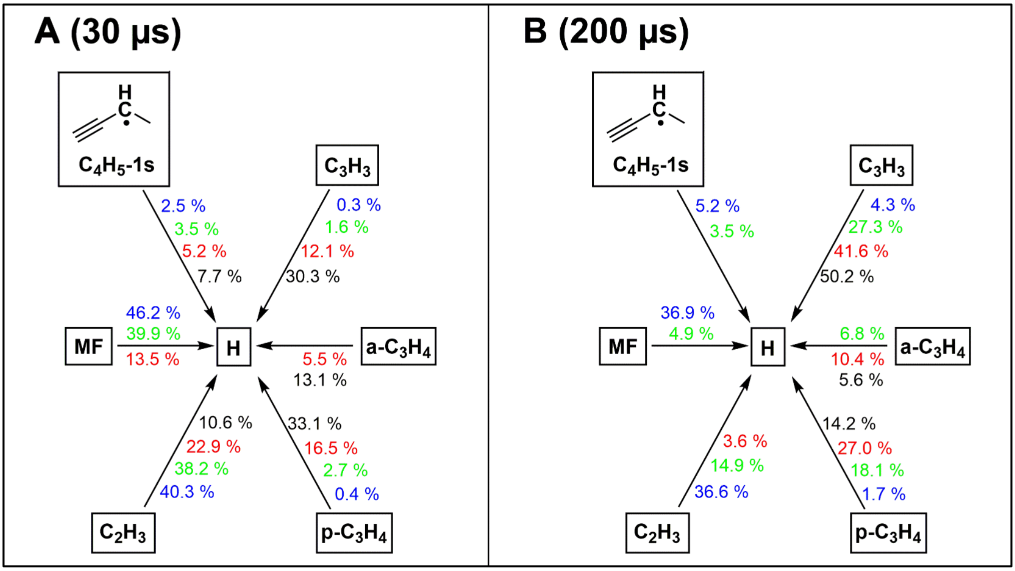
A (30 μs)
H
C
C4H5-1s
C3H3
2.5 %
3.5 %
5.2 %
7.7 %
0.3 %
1.6 %
12.1 %
30.3 %
MF
46.2 %
39.9 %
13.5 %
H
5.5 %
13.1 %
a-C3H4
10.6 %
22.9 %
38.2 %
40.3 %
33.1 %
16.5 %
2.7 %
0.4 %
C2H3
p-C3H4
B (200 μs)
H
C
C4H5-1s
C3H3
5.2 %
3.5 %
4.3 %
27.3 %
41.6 %
50.2 %
MF
36.9 %
4.9 %
H
6.8 %
10.4 %
5.6 %
a-C3H4
3.6 %
14.9 %
36.6 %
14.2 %
27.0 %
18.1 %
1.7 %
C2H3
p-C3H4

Figure 6.15: Reaction flux analysis for the formation of H atoms at *t* ~ 30 μs (A) and *t* ~ 200 μs (B). Experimental conditions: *T* = 1480 K (blue), 1580 K (green), 1690 K (red), 1790 K (black), *p* ~ 1 bar.

6.5 Formation of H Atoms in the Pyrolysis of 2,5-Dimethyfuran (2,5-DMF)

In his PhD thesis P. Friese [112] determined the rate coefficient for the initial reaction step in the pyrolysis of 2,5-DMF, which is the C-H bond fission in one of the methyl groups:

$$\mathrm{DMF} \rightarrow \mathrm{R1C_5H_7O} + \mathrm{H} \qquad (\mathrm{R}_{6.14})$$

He measured H atom concentration-time profiles by H ARAS behind reflected shock waves at temperatures between 1270 and 1520 K and pressures around 1.7 bar and 4.6 bar. Assuming that only reaction ($\mathrm{R}_{6.14}$) contributes to the production of H atoms at short reaction times, rate coefficients were directly extracted from the initial slope of the concentration-time profiles. To support this assumption, the author simulated concentration-time profiles with the three literature mechanisms by Lifshitz et al. [116], Somers et al. [123] and Sirjean et al. [115]. Employing sensitivity and rate of production analysis, an insight into the main decomposition pathways implemented in these models was gained.

To complete this study on the pyrolysis of the three furan derivatives, simulations with the original mechanism by Liu et al. [4-6], and the modified version developed in this work, are compared to H atom concentration-time profiles recorded by P. Friese (figure 6.16). Both models agree reasonably well with the experimental results. Differences for long reaction times and high temperatures are small.

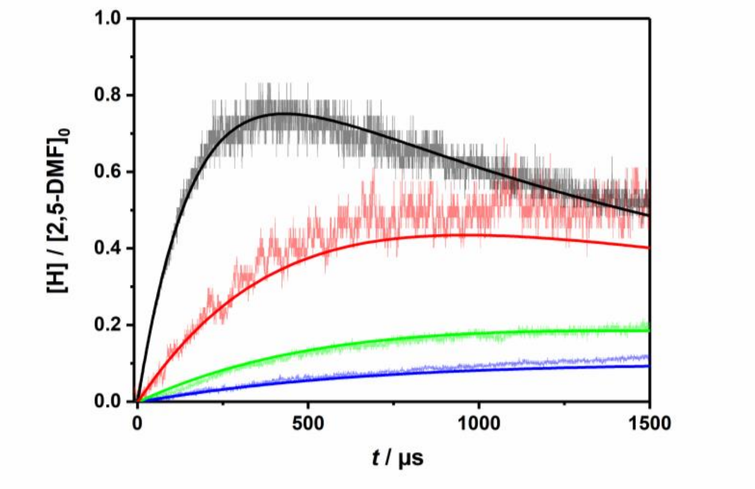

Figure 6.16: Comparison of experimental results from [112] to simulations (dashed lines) with the mechanism by Liu et al. [4-6] and the modified version developed in this work (solid lines). Experimental conditions: T = 1290 K (blue), 1340 K (green), 1400 K (red), 1480 K (black), p ~ 1.7 bar:

The changes implemented in the previous sections have only a minor influence on the predicted H atom concentration-time profiles. In consequence, formation pathways for H atoms in 2,5-DMF pyrolysis must be different from the ones in the pyrolysis of the other two derivatives.

A reaction flux analysis for H atoms identifies the ring-opening reaction to 3,4-hexadien-2-one ($M4C_6H_8O$) as the main consumption pathway for 2,5-DMF (figure 6.17(A)). This intermediate rapidly decomposes yielding the 1-methyl-2-propyne-1-yl radical (C_4H_5-1s) which could be identified as the main source of H atoms (figure 6.17(B)). The direct C-H bond fission in one of the methyl groups appears to be only the second important reaction channel. If the mechanism by Liu et al. [4-6] correctly describes the pyrolysis of 2,5-DMF, the rate coefficient determined by P. Friese [112] corresponds to the reaction

$$\text{DMF} \rightarrow \text{products} + \text{H} \qquad (R_{6.15})$$

rather than to reaction ($R_{6.14}$).

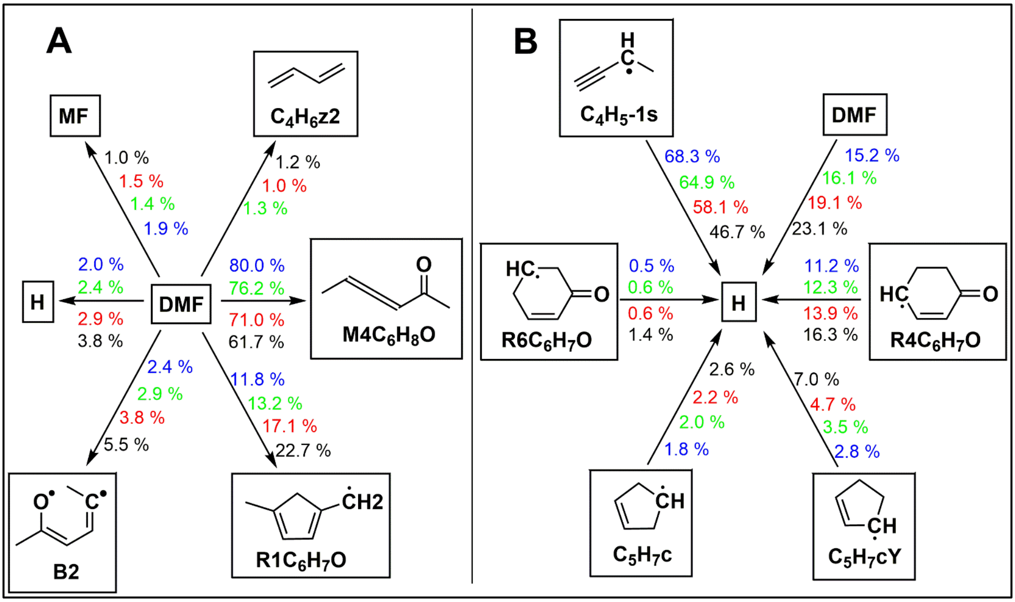
A
MF
C4H6z2
H
DMF
M4C6H8O
B2
R1C6H7O
1.0 %
1.5 %
1.4 %
1.9 %
1.2 %
1.0 %
1.3 %
2.0 %
2.4 %
2.9 %
3.8 %
80.0 %
76.2 %
71.0 %
61.7 %
2.4 %
2.9 %
3.8 %
5.5 %
11.8 %
13.2 %
17.1 %
22.7 %
B
C4H5-1s
DMF
R6C6H7O
H
R4C6H7O
C5H7c
C5H7cY
68.3 %
64.9 %
58.1 %
46.7 %
15.2 %
16.1 %
19.1 %
23.1 %
0.5 %
0.6 %
0.6 %
1.4 %
11.2 %
12.3 %
13.9 %
16.3 %
2.6 %
2.2 %
2.0 %
1.8 %
7.0 %
4.7 %
3.5 %
2.8 %

Figure 6.17: Reaction flux analysis for H atoms in the decomposition of 2,5-DMF (A) and the production of H atoms (B) at *t* ~ 30 µs. Experimental conditions: *T* = 1290 K (blue), 1340 K (green), 1400 K (red), 1480 K (black), *p* ~ 1.7 bar.

In their original publication Sirjean et al. [109] noted the importance of the 2,5-DMF ring-opening channel in the decomposition of the reactant, and pointed out that the assumption made by P. Friese [112] might not hold. As Liu et al. [4-6] adopted the model by Sirjean et al. [109, 115] without further modifications, it is not surprising that similar results are obtained.

6.6 The 2017 Mechanism by Tran et al. [103]

Most recently, Tran et al. [103] adjusted a first modified version [102] of the mechanism by Liu et al. [4-6] to best describe results obtained in flow-reactor experiments at 1 bar (*T* = 730 – 1170 K). Since the experimental conditions in their study are similar to the ones of this work, H atom concentration-time profiles simulated with the 1 bar mechanism by Tran et al. [103] will be briefly discussed here.

In figure 6.18, the experimental results of this work are compared to the simulations with the 2017 mechanism. As for the original version by Liu et al. [4-6], only the results of experiments on 2,5-DMF are well predicted.

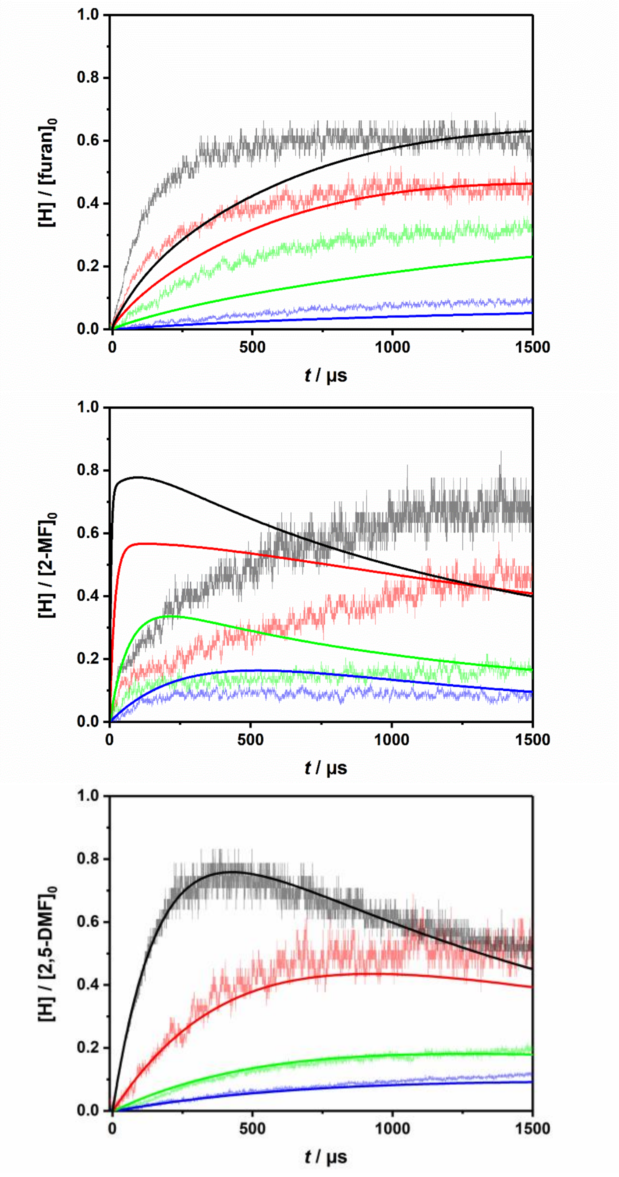

Figure 6.18: Comparison of the experimental results for the pyrolysis of furan, 2-MF and 2,5-DMF (from top to bottom) to simulations (solid lines) with the mechanism by Tran et al. [103]. Experimental conditions: Furan: T = 1540 K (blue), 1650 K (green), 1770 K (red), 1825 K (black), p ~ 1 bar. 2-MF: T = 1480 K (blue), 1580 K (green), 1690 K (red), 1790 K (black), p ~ 1 bar. 2,5-DMF: T = 1290 K (blue), 1340 K (green), 1400 K (red), 1480 K (black), p ~ 1.7 bar.

For furan decomposition, the simulations with the 2017 model show a better agreement compared to simulations with the original one. H atom concentration-time profiles are still underpredicted, especially for short reaction times. However, for high temperatures and long reaction times, simulations and recorded profiles agree well. H atom formation in the pyrolysis of 2-MF is not accurately described by both versions of the model.

The reaction flux analysis for H atoms in the decomposition of furan (figure 6.19(A)) indicates a different influence of the initial reaction channels compared to the modified mechanism of this work (figure 6.6 and figure 6.7). The importance of reaction ($R_{6.3}$) yielding ketene and acetylene is nearly doubled. However, neither ketene nor acetylene are a source of H atoms. H atoms are mainly formed from propyne and, at low temperatures, from formyl radicals (compare figure 6.19(B)). These are products of the decomposition of 2,3-butadienale. As the importance of the decomposition channel leading to 2,3-butadienale is reduced, less H atom sources are formed and thus H atom concentrations are underpredicted. Consequently, the cause of underprediction will most probably lie in the parameterization of the initial reaction steps.

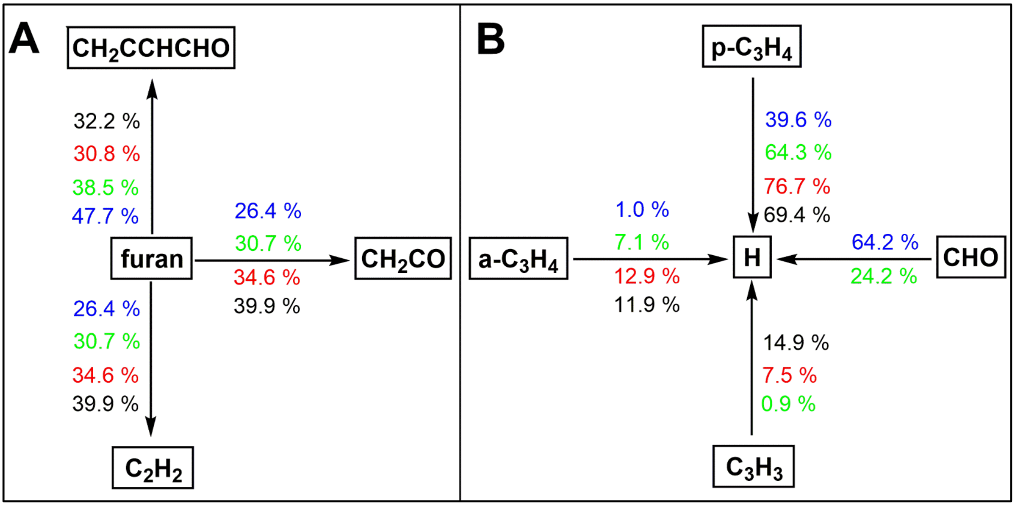

Figure 6.19: Reaction flux analysis for H atoms in the decomposition of furan (A) and the production of H atoms (B) at *t* ~ 30 µs. Experimental conditions: *T* = 1540 K (blue), 1650 K (green), 1770 K (red), 1825 K (black), *p* ~ 1 bar.

For 2-MF, a reaction flux analysis of the 2017 mechanism for H atoms in the consumption of the reactant shows an enhanced importance of the C-H bond fission channel compared to the model developed in this work (figure 6.15). In consequence, more H atoms are formed at short reaction times. While the relative importance of the decomposition channels leading to 3,4-pentadienone and 2,3-pentadienale is similar for both models, the importance of the α-carbene channel is significantly lower in the 2017 version by Tran et al. [103]. For long reaction times, H atom consuming reaction steps must play an important role, as the model by Tran et al. predicts a decrease of H atom concentrations. With respect to the formation of H atoms, the reaction flux analysis of the two models shows similar results.

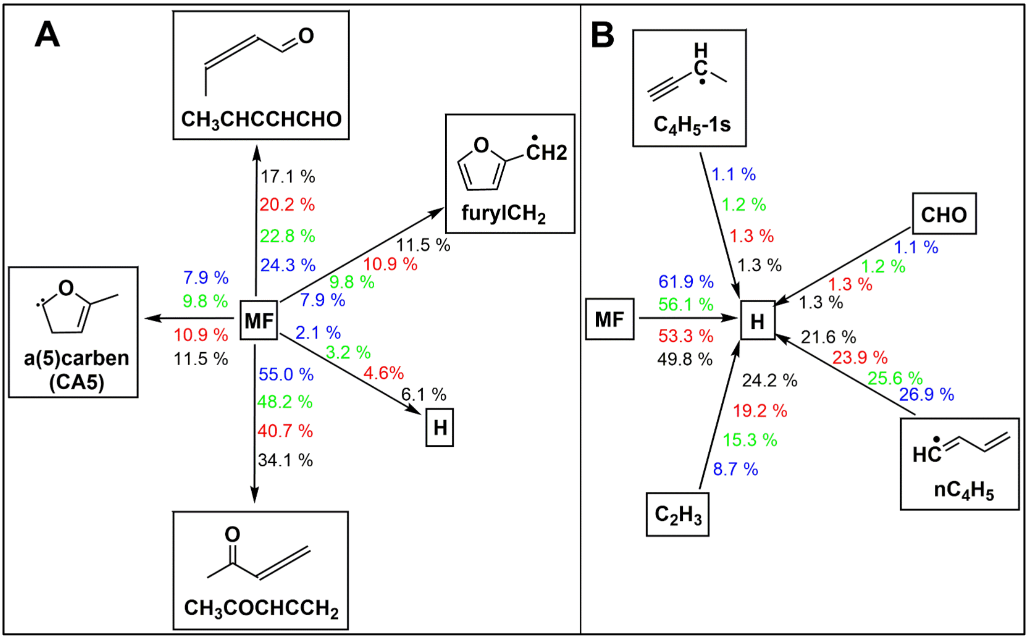
A
CH3CHCCHCHO
17.1 %
20.2 %
22.8 %
24.3 %
furylCH2
CH2
11.5 %
10.9 %
9.8 %
7.9 %
7.9 %
9.8 %
10.9 %
11.5 %
a(5)carben
(CA5)
MF
2.1 %
3.2 %
4.6%
6.1 %
H
55.0 %
48.2 %
40.7 %
34.1 %
CH3COCHCCH2
B
C4H5-1s
1.1 %
1.2 %
1.3 %
1.3 %
CHO
1.1 %
1.2 %
1.3 %
1.3 %
MF
61.9 %
56.1 %
53.3 %
49.8 %
H
21.6 %
23.9 %
25.6 %
26.9 %
24.2 %
19.2 %
15.3 %
8.7 %
C2H3
nC4H5

Figure 6.20: Reaction flux analysis for H atoms in the decomposition of 2-MF (A) and the production of H atoms (B) at *t* ~ 1 µs. Experimental conditions: *T* = 1480 K (blue), 1580 K (green), 1690 K (red), 1790 K (black), *p* ~ 1 bar.

6.7 Conclusions

In this chapter the initial steps in the pyrolysis of furan, 2-MF and 2,5-DMF were discussed with focus on the formation of H atoms. To gain information, the mechanism by Liu et al. [4-6] was modified to best describe the experimental results obtained in this work. Sensitivity and reaction flux analysis were applied to identify the most important reaction steps in the formation of H atoms.

As expected from the bond dissociation energies of C-H bonds in the three molecules (compare section 6.1), a direct formation of H atoms by C-H bond fission only occurs for the methylated furan derivatives.

With increasing methylation of the furan ring, the lowest temperature at which H atoms could be detected under shock tube conditions decreases (furan: ~ 1500 K, 2-MF: ~ 1400 K, 2,5-DMF: ~ 1200 K). This indicates a change in the reaction pathways for H atom formation. An increasing importance of the C-H bond fission reaction from furan to 2,5-DMF would be in line with the bond dissociation energies and the increasing number of H atoms bound in methyl groups (2-MF: 3, 2,5-DMF: 6). However, the analysis of the modified mechanism developed in this work does not support this hypothesis. Whilst the C-H bond fission dominates the H atom production from 2-MF at short reaction times, the 1-butyne-3-yl radical is the main source of H atoms in 2,5-DMF pyrolysis. 1-butyne-3-yl radicals are directly formed from the ring-opening product 3,4-hexadien-2-one. Which channel actually dominates the formation of H atoms from 2,5-DMF cannot be distinguished by H ARAS experiments alone. Nevertheless, H ARAS experiments on the thermal decomposition of 3,4-hexadien-2-one and the 2-methy-5-methylfuryl radical formed by the C-H bond fission reaction could give important information. It should be kept in mind, that Liu et al. [4-6] adopted the mechanism by Sirjean et al. [115] for the description of 2,5-DMF chemistry without further modifications. The result is in line with the results obtained by Sirjean et al. [115].

Simulations with the 2017 mechanism by Tran et al. [103] give a slightly improved description of the production of H atoms in the thermal decomposition of furan compared to the original mechanism by Liu et al. [4-6]. The relative importance of the different initial reaction channels with respect to the formation of H atoms was discussed. A closer look at the parameterization of the initial reaction pathways will be necessary to further evaluate the mechanism.

7 Overall Conclusions and Outlook

This shock tube/ARAS work in general can be divided into three distinct parts:

Instrumental works

Throughout this work different instrumental modifications have been tested.

Even though the test of the new membrane system did not lead to the expected improvement in reproducibility, its use in further studies is recommendable. As the cutter system prevents the uncontrolled splintering of the membranes, it could improve the work on the shock tube/TOF-MS experiment. Another trial on the reproducibility should be performed with significantly thinner polycarbonate sheets as diaphragms.

The constructed filter flange was tested in two experimental setups. As an oxygen filter, it proved sufficient to omit the atomic oxygen emission lines at ~ 130 nm. Utilizing the filter flange as an atomic filter, the fraction of resonance radiation was determined.

Main focus of the instrumental works was the test of a dual ARAS setup consisting of a H ARAS and an I ARAS detection unit. The two possible combinations were discussed. For a horizontal H ARAS/vertical I ARAS setup, the main advantage lies in the preservation of the quality of measured H ARAS profiles. However, due to the low fraction of resonance radiation emitted by the I ARAS lamp, the signal quality of the I ARAS results decreases. It is acceptable for experiments on highly diluted mixtures.

With a vertical H ARAS/horizontal I ARAS setup, the quality of the I ARAS measurements significantly improves. However, due to the loss in intensity in the H ARAS setup caused by the necessity of the utilization of the oxygen filter, the signal-to-noise ratio of the H ARAS experiments decreases. For the operation of a vertical H ARAS experiment, a different approach should be considered: The H ARAS lamp spectrum consists of hydrogen, oxygen and nitrogen atomic emission lines and might also exhibit carbon atomic emission lines to longer wavelengths. H ARAS experiments are mainly disturbed by absorption by oxygen atoms in the calibration procedure. No interference of the other atomic lines is to be expected in most systems. It was shown in this work, that the oxygen atomic emission line could be omitted by the usage of an oxygen filter. Thus, it should be possible to operate a vertical H ARAS setup without the narrow band pass filter utilized in this work. This should solve the problem of too low intensities and the consequential low signal-to-noise ratios.

Additionally, the integration of other ARAS detection methods into the dual ARAS experiment has been discussed.

Ethyl iodide and the calibration of I ARAS

As a first trial of the new dual ARAS setup, the branching ratios of the initial pathways in the thermal decomposition of ethyl iodide were determined. A good agreement of the results with values from previous studies could be obtained. Differences between branching ratios and I atom yields were discussed.

Throughout the experiments, inconsistencies in the calibration of I ARAS with methyl iodide became obvious. Therefore, the thermal decomposition of methyl iodide was revaluated. For these measurements, I ARAS was calibrated by experiments on ethyl iodide under the condition that H and I atom concentrations are equal at short reaction times. The rate coefficient for the C-I bond fission in methyl iodide was determined to

$$k_{(\mathrm{R}_{5.11})}(T) = 7.4 \cdot 10^{14} \cdot \exp\left(-\frac{160\ \mathrm{kJ\ mol^{-1}}}{\mathrm{R}T}\right) \mathrm{cm^3\ mol^{-1}\ s^{-1}}.$$

Additionally, a small reaction mechanism was deduced to explain the formation of H atoms from methyl iodide at high temperatures.

To achieve a reliable calibration of I ARAS under different experimental conditions, an investigation of the pressure dependence of the rate coefficient for the C-I bond fission ($\mathrm{R}_{5.8}$) would be beneficial.

Pyrolysis of furan derivatives

In the third part of this work, the initial steps in the pyrolysis of the three furan derivatives furan, 2-MF and 2,5-DMF were investigated. The oxidation mechanism published by Liu et al. [4-6] was modified to best describe the H atom concentration-time profiles recorded in this study. The modified mechanism was analysed by means of sensitivity and reaction flux analysis to identify the major pathways in the formation of H atoms. The influence of increasing methylation of the furan moiety was discussed.

Overall rate coefficients for the reaction

$$\text{reactant} \rightarrow \text{products} + \mathrm{H} \qquad (\mathrm{R}_{7.1})$$

determined from the initial slope of the measured H atom concentration-time profiles are compared in figure 7.1. Rate coefficients increase with increasing methylation. This could indicate an increasing influence of the C-H bond fission channel as suspected from the bond dissociation energies for different C-H bond calculated by Simmie and Curran [111]. The results of the analysis of the modified mechanism partly contradict this conclusion. As shown in chapter 6, the importance of the C-H bond fission does increase from furan to 2-MF. However, for 2,5-DMF the modified mechanism ascribes the formation of H atoms to the decomposition of the primary product 3,4-hexadien-2-one (M4C_6H_8O) of the ring-opening reaction. Based on the result of this work, it is not possible to unequivocally identify the source of the H atoms formed. Further investigations of the thermal decomposition of the primary products of the C-H bond fission and the ring-opening process would be necessary.

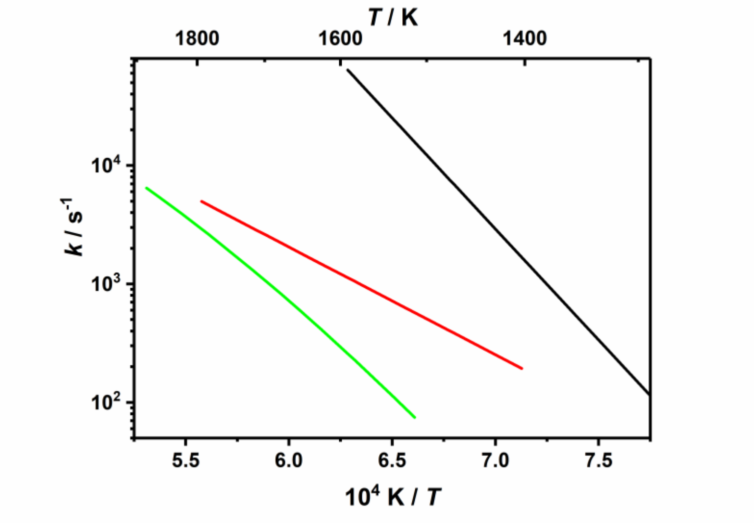

Figure 7.1: Overall rate coefficients for the reaction 'reactant → products + H' for furan (green), 2-MF (red) and 2,5-DMF (black) determined from the initial slope of the recorded H atom concentration-time profiles.

Appendix

A.1 Chemicals and Gases

substance	CAS number	purity	distributor
argon (Ar)	7440-37-1	$\geq$ 99.999 %	Air Liquide
hydrogen (driver gas)	1333-74-0	$\geq$ 99.9 %	Air Liquide
hydrogen (mixtures)	1333-74-0	$\geq$ 99.999 %	Messer Griesheim
helium (He)	7440-59-7	$\geq$ 99.999 %	Air Liquide
nitrous oxide (N_2O)	10024-97-2	$\geq$ 99.5 %	Air Liquide
oxygen (O_2)	7782-44-7	$\geq$ 99.998 %	Air Liquide
chlorine (Cl_2)	7782-50-5	$\geq$ 99.998 %	Air Liquide
nitrogen (N_2)	7727-37-9	$\geq$ 99.995 %	Air Liquide
2,5-dimethylfuran	626-86-5	99 %	Sigma-Aldrich
2-methylfuran	534-22-5	99 %	Sigma-Aldrich
furan	110-00-9	$\geq$ 99 %	Sigma-Aldrich
ethyl iodide	75-03-6	99 %	Sigma-Aldrich
methyl iodide	74-88-4	99.5 %	Sigma-Aldrich
iodine monochloride	7790-99-0	99.998 %	Sigma-Aldrich

A.2 Identified Atomic Emission Lines in Accordance with Ref. [28]

A.2.1 Hydrogen (H)

λ / nm	transition
121.6	${}^2S_{1/2} \leftarrow {}^2P^0_{3/2}$ ${}^2S_{1/2} \leftarrow {}^2P^0_{1/2}$

A.2.2 Nitrogen (N)

λ / nm	transition
119.9	${}^4S^0_{3/2} \leftarrow {}^4P_{5/2}$
120.0	${}^4S^0_{3/2} \leftarrow {}^4P_{3/2}$ ${}^4S^0_{3/2} \leftarrow {}^4P_{1/2}$
124.3	${}^2D^0_{5/2} \leftarrow {}^2D_{5/2}$
141.1	---
149.2	${}^2D^0_{5/2} \leftarrow {}^2P_{3/2}$
149.4	---
174.2	${}^2P^0_{3/2} \leftarrow {}^2P_{3/2}$

A.2.3 Carbon (C)

λ / nm	transition
126.1	---
127.7	${}^3P_0 \leftarrow {}^3D_2^0$ ${}^3P_1 \leftarrow {}^3D_1^0$ ${}^3P_1 \leftarrow {}^3D_3^0$
128.0	${}^3P_2 \leftarrow {}^3P_2^0$
132.9	---
156.0	${}^3P_1 \leftarrow {}^3D_2^0$ ${}^3P_1 \leftarrow {}^3D_3^0$
165.5	${}^3P_1 \leftarrow {}^3P_2^0$
165.7	${}^3P_0 \leftarrow {}^3P_1^0$ ${}^3P_2 \leftarrow {}^3P_2^0$
165.8	${}^3P_2 \leftarrow {}^3P_1^0$

A.2.4 Oxygen (O)

λ / nm	transition
130.2	${}^3P_2 \leftarrow {}^3S_1^0$
130.4	${}^3P_1 \leftarrow {}^1S_1^0$
130.6	${}^3P_0 \leftarrow {}^1S_1^0$

A.2.5 Chlorine (Cl)

λ / nm	transition
117.9	---
133.5	${}^2P^0_{3/2} \leftarrow {}^2P_{1/2}$
134.7	${}^2P^0_{3/2} \leftarrow {}^2P_{3/2}$
135.1	${}^2P^0_{1/2} \leftarrow {}^2P_{1/2}$
136.3	${}^2P^0_{1/2} \leftarrow {}^2P_{3/2}$
137.9	${}^2P^0_{3/2} \leftarrow {}^4P_{3/2}$
138.9	${}^2P^0_{3/2} \leftarrow {}^4P_{5/2}$ ${}^2P^0_{1/2} \leftarrow {}^4P_{1/2}$
139.6	${}^2P^0_{1/2} \leftarrow {}^4P_{3/2}$

A.2.6 Iodine (I)

λ / nm	transitions
136.1	---
139.0	---
142.5	---
144.6	---
145.7	${}^2P^0_{3/2} \leftarrow {}^2[2]_{5/2}$
149.2	---
151.4	---
151.8	${}^2P^0_{1/2} \leftarrow {}^2[1]_{1/2}$
159.3	---
161.7	---
170.2	${}^2P^0_{1/2} \leftarrow {}^2[1]_{3/2}$

λ / nm	transitions
178.2	${}^{2}P^{0}_{3/2} \leftarrow {}^{2}[2]_{3/2}$
179.9	---
184.4	${}^{2}P^{0}_{1/2} \leftarrow {}^{2}[1]_{3/2}$

A.3 Abbrevations of Experimental Techniques

GC	gas chromatography
GC-FID	gas chromatography flame ionization detector
GC-TCD	gas chromatography thermal conductivity detector
GC-MS	gas chromatography mass spectrometry
FT-IR	fourier transform infrared spectroscopy
MS	mass spectrometry
TOF-MS	time of flight mass spectrometry
PI-MS	photoionization mass spectrometry
SVUV-PIMS	synchrotron vacuum ultraviolet photoionization mass spectrometry
MBMS	molecular beam mass spectrometry
EI-MBMS	electron ionization molecular beam mass spectrometry
EI-MBMS-TOF	electron ionization molecular beam mass spectrometry (time of flight)

A.4 Experimental Conditions and Rate Coefficients for the Thermal Decomposition of Methyl Iodide

T / K	p / bar	[Ar] / mol cm^{-3}	$[CH_3I]_0$ / mol cm^{-3}	k / s^{-1}
950	1.73	2.2×10^{-5}	5.2×10^{-11}	25
980	1.72	2.3×10^{-5}	5.0×10^{-11}	42
1020	1.64	2.0×10^{-5}	4.6×10^{-11}	108
1020	1.66	2.0×10^{-5}	4.7×10^{-11}	64
1030	1.64	1.8×10^{-5}	4.6×10^{-11}	133
1050	1.64	1.9×10^{-5}	5.2×10^{-11}	90
1050	1.58	1.6×10^{-5}	3.8×10^{-11}	182
1080	1.73	1.9×10^{-5}	4.6×10^{-11}	196
1080	1.67	1.9×10^{-5}	5.1×10^{-11}	238
1090	1.69	1.9×10^{-5}	4.5×10^{-11}	386
1100	1.79	2.0×10^{-5}	4.6×10^{-11}	459
1110	1.56	1.7×10^{-5}	4.6×10^{-11}	592
1110	1.71	2.0×10^{-5}	4.4×10^{-11}	622
1120	1.67	1.8×10^{-5}	4.3×10^{-11}	767
1030	1.84	2.0×10^{-5}	4.6×10^{-11}	769
1150	1.67	1.7×10^{-5}	4.1×10^{-11}	559
1180	1.78	1.8×10^{-5}	4.3×10^{-11}	1524
1180	1.69	1.7×10^{-5}	4.1×10^{-11}	1424
1210	1.59	1.6×10^{-5}	4.4×10^{-11}	1177
1220	1.64	1.6×10^{-5}	3.9×10^{-11}	1644
1230	1.76	1.7×10^{-5}	4.7×10^{-11}	1584

A.5 Experimental Conditions and Branching Ratios for the Thermal Decomposition of Ethyl Iodide

T / K	p / bar	[Ar] / mol cm^{-3}	$[C_2H_5I]_0$ / mol cm^{-3}	$\phi_{R5.1}$
1100	1.65	1.80×10^{-5}	6.99×10^{-11}	0.94
1130	1.68	1.78×10^{-5}	4.08×10^{-11}	0.89
1160	1.64	2.15×10^{-5}	4.90×10^{-11}	0.95
1180	1.62	1.65×10^{-5}	6.41×10^{-11}	0.92
1200	1.65	1.65×10^{-5}	4.17×10^{-11}	0.90
1200	1.23	1.23×10^{-5}	9.56×10^{-11}	0.91
1240	1.60	1.56×10^{-5}	6.03×10^{-11}	0.90
1320	1.21	1.10×10^{-5}	8.50×10^{-11}	0.97

A.6 Experimental Conditions for the Thermal Decomposition of Furan Detivatives

A.6.1 Furan

T / K	p / bar	[Ar] / mol cm^{-3}	[furan]$_0$ / mol cm^{-3}
1540	1.06	8.3×10^{-6}	4.4×10^{-11}
1650	1.10	8.0×10^{-6}	3.7×10^{-11}
1770	1.05	7.1×10^{-6}	6.6×10^{-11}
1825	0.91	6.0×10^{-6}	5.6×10^{-11}

A.6.2 2-Methylfuran

T / K	p / bar	[Ar] / mol cm^{-3}	[2-MF]$_0$ / mol cm^{-3}
1480	1.12	9.1×10^{-6}	4.0×10^{-11}
1580	1.09	8.2×10^{-6}	3.6×10^{-11}
1690	0.93	6.6×10^{-6}	2.9×10^{-11}
1790	0.97	6.5×10^{-6}	6.6×10^{-11}

A.6.3 2,5-Dimethylfuran

All experiments were conducted by P. Friese during his PhD thesis [112].

T / K	p / bar	[Ar] / mol cm^{-3}	[2,5-DMF]$_0$ / mol cm^{-3}
1290	1.64	1.5×10^{-5}	6.1×10^{-11}
1340	1.68	1.5×10^{-5}	6.3×10^{-11}
1400	1.61	1.4×10^{-5}	4.7×10^{-11}
1480	1.60	1.3×10^{-5}	5.2×10^{-11}

A.7 Rate Coefficients Implemented in the Modified Furan Mechanism

Rate coefficients implemented into the original mechanism for the oxidation of furan and its methyl substituted derivatives [4-6]. For a detailed discussion see chapter 6.

Parameterization: $k(T) = A \times (T/\mathrm{K})^n \times \exp(-E_\mathrm{a}/\mathrm{R}T)$. Units: s^{-1}, kJ, mol^{-1}, cm^3, K.

	reaction	A	n	E_a	ref.
($\mathrm{R}_{6.2}$)	furan $\rightleftharpoons$ $CH_2CCHCHO$	5.90×10^{13}	0.000	293	[117]
($\mathrm{R}_{6.3}$)	furan $\rightleftharpoons$ $C_2H_2 + CH_2CO$	9.00×10^{14}	0.000	344	[117]
($\mathrm{R}_{6.5}$)	$CH_2CCHCHO \rightleftharpoons CO + pC_3H_4$	1.70×10^{13}	0.000	168	[117]
($\mathrm{R}_{6.1}$)	$pC_3H_4 + M \rightleftharpoons C_3H_3 + H + M$	2.16×10^{43}	-6.810	421	[143]
($\mathrm{R}_{6.6}$)	$aC_3H_4 + M \rightleftharpoons C_3H_3 + H + M$	2.16×10^{43}	-6.810	421	[143]
($\mathrm{R}_{6.7}$)	$C_3H_2 + H \rightarrow C_3H_3$	2.66×10^{14}	0.220	0.36	[144]
	$C_3H_3 \rightarrow C_3H_2 + H$	5.20×10^{12}	0.000	328	[61]
	MF $\rightleftharpoons$ H + $\mathrm{furylCH_2}$	1.42×10^{65}	-14.34	494	[145]
($\mathrm{R}_{6.10}$)	MF $\rightleftharpoons$ $CH_3COCHCCH_2$	1.75×10^{10}	1.000	284	[145]
	$CH_3COCHCCH_2 \rightleftharpoons CH_3CO + C_3H_3$	1.52×10^{25}	-2.480	329	[145]
	$CH_3COCHCCH_2 \rightleftharpoons pC_3H_4+CH_2CO$	3.91×10^{8}	1.480	281	[145]
($\mathrm{R}_{6.11}$)	MF $\rightleftharpoons$ $CH_3CHCCHCHO$	2.15×10^{10}	0.750	292	[145]
($\mathrm{R}_{6.13}$)	$CH_3CHCCHCHO \rightleftharpoons CO + C_4H_6x1$	7.30×10^{10}	0.690	182	[145]
	$CH_3CHCCHCHO \rightleftharpoons CO + C_4H_6x12$	3.40×10^{11}	1.000	247	[145]
	MF $\rightleftharpoons$ a(5)Carben	2.26×10^{10}	0.990	270	[145]
	a(5)Carben $\rightleftharpoons$ $pC_3H_4+CH_2CO$	8.54×10^{12}	0.680	132	[145]

Bibliography

[1] Lifshitz, A.;Skinner, G. B.;Wood, D. R., *J. Chem. Phys.*, **1979**, 70, 5607-5613.

[2] Yang, X.;Goldsmith, C. F.;Tranter, R. S., *J. Phys. Chem. A*, **2009**, 113, 8307-8317.

[3] Ben-Dor, G.;Igra, O.;Elperin, T., *Handbook of Shock Waves*, Academic Press, **2000**.

[4] Liu, D.;Togbé, C.;Tran, L.-S.;Felsmann, D.;Oßwald, P.;Nau, P.;Koppmann, J.;Lackner, A.;Glaude, P.-A.;Sirjean, B.;Fournet, R.;Battin-Leclerc, F.;Kohse-Höinghaus, K., *Combust. Flame*, **2014**, 161, 748-765.

[5] Tran, L.-S.;Togbé, C.;Liu, D.;Felsmann, D.;Oßwald, P.;Glaude, P.-A.;Fournet, R.;Sirjean, B.;Battin-Leclerc, F.;Kohse-Höinghaus, K., *Combust. Flame*, **2014**, 161, 766-779.

[6] Togbé, C.;Tran, L.-S.;Liu, D.;Felsmann, D.;Oßwald, P.;Glaude, P.-A.;Sirjean, B.;Fournet, R.;Battin-Leclerc, F.;Kohse-Höinghaus, K., *Combust. Flame*, **2014**, 161, 780-797.

[7] Oertel, H., *Stossrohre*, 1 ed., Springer, Wien, **1966**.

[8] Green, E. F.;Toennies, J. P., *Chemische Reaktionen in Stosswellen*, 1 ed., Springer-Verlag, **2013**.

[9] Zel'dovich, Y. B.;Raizer, Y. P., *Physics of Shock Waves and High-Temperature Hydrodynamic Phenomena*, 3 ed., Dover, **2002**.

[10] Myerson, A. L.;Thompson, H. M.;Joseph, P. J., *J. Chem. Phys.*, **1965**, 42, 3331-3332.

[11] Thielen, K.;Roth, P., *Proc. Combust. Inst.*, **1985**, 20, 685-693.

[12] Davidson, D. F.;Hanson, R. K., *Int. J. Chem. Kinet.*, **1990**, 22, 843-861.

[13] Appel, D.;Appleton, J. P., *Proc. Combust. Inst.*, **1975**, 15, 701-715.

[14] Roth, P.;Just, T., *Ber. Bunsenges. Phys. Chem.*, **1975**, 79, 682-686.

[15] Naudet, V.;Abid, S.;Paillard, C. E., *J. Chim. Phys.*, **1999**, 96, 1123-1145.

[16] Pamidimukkala, K. M.;Lifshitz, A.;Skinner, G. B.;Wood, D. R., *J. Chem. Phys.*, **1981**, 75, 1116-1122.

[17] Roth, P.;Just, T., *Ber. Bunsenges. Phys. Chem.*, **1977**, 81, 572-577.

[18] Lim, K. P.;Michael, J. V., *J. Chem. Phys.*, **1993**, 98, 3919-3928.

[19] Kunz, A.;Roth, P., *Proc. Combust. Inst.*, **1998**, 27, 261-267.

[20] Dean, A. J.;Davidson, D. F.;Hanson, R. K., *17th International Symposium on Shock Tubes and Waves, Lehigh, PA*, **1989**,

[21] Dean, A. J.;Hanson, R. K.;Bowman, C. T., *J. Phys. Chem.*, **1991**, 95, 3180-3189.

[22] Braun-Unkhoff, M.;Frank, P.;Just, T., *Ber. Bunsenges. Phys. Chem.*, **1990**, 94, 1417-1425.

[23] Wintergerst, K., *Reaktionskinetische Untersuchungen von verbrennungsrelevanten Methan- und Methylenreaktionen*, Dissertation, Universität Stuttgart, **1993**.

[24] Braun, W.;Bass, A. M.;Davis, D. D., *J. Opt. Soc. Am.*, **1970**, 60, 166-170.

[25] Zemansky, M. W.;Mitchell, A. C. G., *Resonance Radiation and Excited Atoms*, 2nd ed., Cambridge University Press, Cambridge, **1961**.

[26] Cowan, R. D.;Dieke, G. H., *Rev. Mod. Phys.*, **1948**, 20, 418-455.

[27] Ladenburg, R.;Reiche, F., *Ann. Phys.*, **1913**, 347, 181-209.

[28] Sansonetti, J. E.;Martin, W. C., *J. Phys. Chem. Ref. Data*, **2005**, 34, 1559-2259.

[29] Myerson, A. L.;Watt, W. S., *J. Chem. Phys.*, **1968**, 49, 425-433.

[30] Meltzer, R. J., *Appl. Opt. Opt. Eng.*, **1969**, 5, 47-84.

[31] Czerny, M.;Turner, A. F., *Z. Phys.*, **1930**, 61, 792-797.

[32] Naumann, H.;Schröder, G., *Bauelemente der Optik. Taschenbuch der technischen Optik*, 6 ed., Carl Hanser Verlag, München, **1992**.

[33] Samson, J. A.;Ederer, D. L., *Vacuum Ultraviolet Spectroscopy II*, Academic Press, San Diego, **2000**.

[34] Samson, J. A.;Ederer, D. L., *Vacuum Ultraviolet Spectroscopy I*, Academic Press, San Diego, **2000**.

[35] Lifshitz, A., *Shock Waves in Chemistry*, 1 ed., Marcel Dekker, INC. , New York, **1981**.

[36] Röhrig, M.;Petersen, E. L.;Davidson, D. F.;Hanson, R. K., *Int. J. Chem. Kinet.*, **1996**, 28, 599-608.

[37] Baulch, D. L.;Cobos, C. J.;Cox, R. A.;Esser, C.;Frank, P.;Just, T.;Kerr, J. A.;Pilling, M. J.;Troe, J.;Walker, R. W., *J. Phys. Chem. Ref. Data*, **1992**, 21, 411-734.

[38] Cohen, N.;Westberg, K. R., *J. Phys. Chem. Ref. Data*, **1983**, 12, 531-590.

[39] Bozzelli, J. W.;Chang, A. Y.;Dean, A. M., *Proc. Combust. Inst.*, **1994**, 25, 965-974.

[40] Tsang, W., *J. Phys. Chem. Ref. Data*, **1991**, 20, 221-273.

[41] Warnatz, J., *Rate Coefficients in the C/H/O System*, Springer, **1984**.

[42] Steinfeld, J. I.;Francisco, J. S.;Hase, W. L., *Chemical Kinetics and Dynamics*, 2 ed., Prentice Hall, Upper Saddle River, **1999**.

[43] Warnatz, J.;Maas, U.;Dibble, R. W., *Verbrennung*, 3 ed., Springer, Berlin, **2001**.

[44] Cuoci, A.;Frassoldati, A.;Faravelli, T.;Ranzi, E., *XXXIV Meeting of the Italian Section of the Combustion Institute*, **2011**, 1-6.

[45] Cuoci, A.;Frassoldati, A.;Faravelli, T.;Ranzi, E., *Comput. Phys. Commun.*, **2015**, 192, 237-264.

[46] Turányi, T.;Tomlin, A. S., *Analysis of Kinetic Reaction Mechanisms*, 1 ed., Springer, Heidelberg, **2014**.

[47] Arrhenius, S., *Z. Phys. Chem.*, **1889**, 4, 226-248.

[48] Kooij, D. M., *Z. Phys. Chem.*, **1893**, 12, 155-161.

[49] Lindemann, F. A.;Arrhenius, S.;Langmuir, I.;Dhar, N. R.;Perrin, J.;McC. Lewis, W. C., *J. Chem. Soc. Faraday Trans.*, **1922**, 17, 598-606.

[50] Lindemann, F. A., *Philos. Mag.*, **1920**, 40, 671-674.

[51] Hinshelwood, C. N., *Proc. R. Soc. London, Ser. A,*, **1926**, 113, 230-233.

[52] Rice, O. K.;Ramsperger, H. C., *J. Am. Chem. Soc.*, **1928**, 50, 617-620.

[53] Kassel, L. S., *J. Phys. Chem.*, **1927**, 32, 1065-1079.

[54] Marcus, R. A., *J. Chem. Phys.*, **1952**, 20, 359-364.

[55] Marcus, R. A.;Rice, O. K., *J. Phys. Chem.*, **1951**, 55, 894-908.

[56] Bentz, T., *ARASKalib*, private communication.

[57] Giri, B. R., private communications.

[58] Kumaran, S. S.;Su, M.-C.;Lim, K. P.;Michael, J. V., *Proc. Combust. Inst.*, **1996**, 26, 605-611.

[59] Keller-Rudek, H.;Moortgat, G. K.;Sander, R.;Sörensen, R., *Earth Syst. Sci. Data*, **2013**, 5, 365-373.

[60] Kumaran, S. S.;Michael, J. V., *Int. J. Chem. Kinet.*, **1997**, 29, 535-543.

[61] Scherer, S.;Just, T.;Frank, P., *Proc. Combust. Inst.*, **2000**, 28, 1511-1518.

[62] Lynch, K. P.;Schwab, T. C.;Michael, J. V., *Int. J. Chem. Kinet.*, **1976**, 8, 651-671.

[63] Maki, R. G.;Michael, J. V.;Sutherland, J. W., *J. Phys. Chem.*, **1985**, 89, 4815-4821.

[64] Bentz, T.;Szőri, M.;Viskolcz, B.;Olzmann, M., *Z. Phys. Chem.*, **2011**, 225, 1117.

[65] Varga, T.;Zsély, I. G.;Turányi, T.;Bentz, T.;Olzmann, M., *Int. J. Chem. Kinet.*, **2014**, 46, 295-304.

[66] Weber, K. H.;Lemieux, J. M.;Zhang, J., *J. Phys. Chem. A*, **2009**, 113, 583-591.

[67] Yamauchi, N.;Miyoshi, A.;Kosaka, K.;Koshi, M.;Matsui, H., *J. Phys. Chem. A*, **1999**, 103, 2723-2733.

[68] Mertens, J. D.;Wooldridge, M. S.;Hanson, R. K., *Chemical and Physical Processes in Combustion*, **1994**, 106-107.

[69] Yang, X.;Tranter, R. S., *Int. J. Chem. Kinet.*, **2012**, 44, 433-443.

[70] Yang, J. H.;Conway, D. C., *J. Chem. Phys.*, **1965**, 43, 1296-1303.

[71] Butler, E. T.;Polanyi, M., *Trans. Faraday Soc.*, **1943**, 39, 19-36.

[72] Miyoshi, A.;Yamauchi, N.;Kosaka, K.;Koshi, M.;Matsui, H., *J. Phys. Chem. A*, **1999**, 103, 46-53.

[73] Michael, J. V.;Kumaran, S. S.;Su, M. C.;Lim, K. P., *Chem. Phys. Let,*, **2000**, 319, 99-106.

[74] Vasileiadis, S.;Benson, S. W., *Int. J. Chem. Kinet.*, **1997**, 29, 915-925.

[75] Bentz, T., *Stoßwellenuntersuchungen zur Reaktionskinetik ungesättigter und teiloxidierter Kohlenwasserstoffe*, Dissertation, Universität Karlsruhe (TH), **2007**.

[76] Goos, E.;Burcat, A.;Ruscic, B., *Extended Third Millennium Thermodynamic Database for Combustion and Air-Pollution Use with Updates from Active Thermochemical Tables.*, http://burcat.technion.ac.il/dir/BURCAT.THR, (last access: July 2017).

[77] Campbell, E. S.;Fristrom, R. M., *Chem. Rev.*, **1958**, 58, 173-234.

[78] Garrett, B. C.;Truhlar, D. G., *J. Am. Chem. Soc.*, **1979**, 101, 5207-5217.

[79] Baulch, D. L.;Duxbury, J.;Grant, S. J.;Montague, D. C., *J. Phys. Chem. Ref. Data*, **1981**, 10, 1-721.

[80] Christie, M. I.;Roy, R. S.;Thrust, B. A., *Trans. Faraday Soc.*, **1959**, 55, 1149-1152.

[81] Clyne, M. A. A.;Cruse, H. W., *J. Chem. Soc., Faraday Trans. 2*, **1972**, 68, 1281-1299.

[82] Clyne, M. A. A.;Cruse, H. W., *J. Chem. Soc., Faraday Trans. 2*, **1972**, 68, 1377-1387.

[83] Hofer, L. J. E.;Wiig, E. O., *J. Am. Chem. Soc.*, **1945**, 67, 1441-1444.

[84] Bonner, W. D.;Gore, W. L.;Yost, D. M., *J. Am. Chem. Soc.*, **1935**, 57, 2723-2724.

[85] Sherman, A.;Li, N., *J. Am. Chem. Soc.*, **1936**, 58, 690-691.

[86] Benson, S. W.;Cruickshank, F. R.;Shaw, R., *Int. J. Chem. Kinet.*, **1969**, 1, 29-43.

[87] Zhang, R.;Sha, G.;Han, D.;Wang, Y.;Zhang, C., *Lixue Xuebao*, **1983**, 197-202.

[88] Wiberg, N., *Lehrbuch der Anorganischen Chemie*, 102 ed., Walter de Grutyer, Berlin

New York, **2008**.

[89] Ogg, J. A. J., *J. Am. Chem. Soc.*, **1934**, 56, 526-536.

[90] Horrex, C.;Lapage, R., *Discuss. Faraday Soc.*, **1951**, 10, 233-234.

[91] Saito, K.;Tahara, H.;Kondo, O.;Yokubo, T.;Higashihara, T.;Murakami, I., *Bull. Chem. Soc. Jpn.*, **1980**, 53, 1335-1339.

[92] Saito, K.;Tahara, H.;Murakami, I., *Bull. Chem. Soc. Jpn.*, **1984**, 57, 3023-3024.

[93] Kodama, S.;Ooi, Y., *Bull. Chem. Soc. Jpn.*, **1990**, 63, 877-885.

[94] Davidson, D. F.;Chang, A. Y.;Di Rosa, M. D.;Hanson, R. K., *J. Quant. Spectrosc. Radiat. Transfer*, **1993**, 49, 559-571.

[95] Baeck, H. J.;Shin, K. S.;Yang, H.;Qin, Z.;Lissianski, V.;Gardiner, W. C., *J. Phys. Chem.*, **1995**, 99, 15925-15929.

[96] Takahashi, K.;Inoue, A.;Inomata, T., *20th International Symposium on Shock Waves*, Pasadena, **1996**, 2, 959-964.

[97] Kiefer, J. H.;Santhanam, S.;Srinivasan, N. K.;Tranter, R. S.;Klippenstein, S. J.;Oehlschlaeger, M. A., *Proc. Combust. Inst.*, **2005**, 30, 1129-1135.

[98] Kumaran, S. S.;Su, M.-C.;Lim, K. P.;Michael, J. V., *Chem. Phys. Let.*, **1995**, 243, 59-63.

[99] Baulch, D. L.;Bowman, C. T.;Cobos, C. J.;Cox, R. A.;Just, T.;Kerr, J. A.;Pilling, M. J.;Stocker, D.;Troe, J.;Tsang, W.;Walker, R. W.;Warnatz, J., *J. Phys. Chem. Ref. Data*, **2005**, 34, 757-1397.

[100] Román-Leshkov, Y.;Barrett, C. J.;Liu, Z. Y.;Dumesic, J. A., *Nature*, **2007**, 447, 982-986.

[101] Alexandrino, K.;Salvo, P.;Millera, Á.;Bilbao, R.;Alzueta, M. U., *Combust. Sci. Technol.*, **2016**, 188, 651-666.

[102] Tran, L.-S.;Sirjean, B.;Glaude, P.-A.;Kohse-Höinghaus, K.;Battin-Leclerc, F., *Proc. Combust. Inst.*, **2015**, 35, 1735-1743.

[103] Tran, L.-S.;Wang, Z.;Carstensen, H.-H.;Hemken, C.;Battin-Leclerc, F.;Kohse-Höinghaus, K., *Combust. Flame*, **2017**, 181, 251-269.

[104] Zhong, S.;Daniel, R.;Xu, H.;Zhang, J.;Turner, D.;Wyszynski, M. L.;Richards, P., *Energy Fuels*, **2010**, 24, 2891-2899.

[105] Wang, C.;Xu, H.;Daniel, R.;Ghafourian, A.;Herreros, J. M.;Shuai, S.;Ma, X., *Fuel*, **2013**, 103, 200-211.

[106] Daniel, R.;Wei, L.;Xu, H.;Wang, C.;Wyszynski, M. L.;Shuai, S., *Energy Fuels*, **2012**, 26, 6661-6668.

[107] Ma, X.;Xu, H.;Jiang, C.;Shuai, S., *Appl. Energy*, **2014**, 122, 247-260.

[108] Zhang, Q.;Chen, G.;Zheng, Z.;Liu, H.;Xu, J.;Yao, M., *Fuel*, **2013**, 103, 730-735.

[109] Sirjean, B.;Fournet, R., *Phys. Chem. Chem. Phys.*, **2013**, 15, 596-611.

[110] Simmie, J. M.;Metcalfe, W. K., *J. Phys. Chem. A*, **2011**, 115, 8877-8888.

[111] Simmie, J. M.;Curran, H. J., *J. Phys. Chem. A*, **2009**, 113, 5128-5137.

[112] Friese, P., *Kinetische Untersuchung der Rolle von Wasserstoffatomen bei der Pyrolyse von 2,5-Dimethylfuran*, Dissertation, Karlsruher Institut für Technologie, **2013**.

[113] Organ, P. P.;Mackie, J. C., *J. Chem. Soc., Faraday Trans.*, **1991**, 87, 815-823.

[114] Lifshitz, A.;Tamburu, C.;Shashua, R., *J. Phys. Chem. A*, **1997**, 101, 1018-1029.

[115] Sirjean, B.;Fournet, R.;Glaude, P. A.;Battin-Leclerc, F.;Wang, W.;Oehlschlaeger, M. A., *J. Phys. Chem. A*, **2013**, 117, 1371-1392.

[116] Lifshitz, A.;Tamburu, C.;Shashua, R., *J. Phys. Chem. A*, **1998**, 102, 10655-10670.

[117] Sendt, K.;Bacskay, G. B.;Mackie, J. C., *J. Phys. Chem. A*, **2000**, 104, 1861-1875.

[118] Tian, Z.;Yuan, T.;Fournet, R.;Glaude, P.-A.;Sirjean, B.;Battin-Leclerc, F.;Zhang, K.;Qi, F., *Combust. Flame*, **2011**, 158, 756-773.

[119] Tian, Z.;Pitz, W. J.;Fournet, R.;Glaude, P.-A.;Battin-Leclerc, F., *Proc. Combust. Inst.*, **2011**, 33, 233-241.

[120] Fulle, D.;Dib, A.;Kiefer, J. H.;Zhang, Q.;Yao, J.;Kern, R. D., *J. Phys. Chem. A*, **1998**, 102, 7480-7486.

[121] Bounaceur, R.;Da Costa, I.;Fournet, R.;Billaud, F.;Battin-Leclerc, F., *Int. J. Chem. Kinet.*, **2005**, 37, 25-49.

[122] Sarathy, S. M.;Vranckx, S.;Yasunaga, K.;Mehl, M.;Oßwald, P.;Metcalfe, W. K.;Westbrook, C. K.;Pitz, W. J.;Kohse-Höinghaus, K.;Fernandes, R. X.;Curran, H. J., *Combust. Flame*, **2012**, 159, 2028-2055.

[123] Somers, K. P.;Simmie, J. M.;Gillespie, F.;Conroy, C.;Black, G.;Metcalfe, W. K.;Battin-Leclerc, F.;Dirrenberger, P.;Herbinet, O.;Glaude, P.-A.;Dagaut, P.;Togbé, C.;Yasunaga, K.;Fernandes, R. X.;Lee, C.;Tripathi, R.;Curran, H. J., *Combust. Flame*, **2013**, 160, 2291-2318.

[124] Sirjean, B.;Fournet, R., *Proc. Combust. Inst.*, **2013**, 34, 241-249.

[125] Somers, K. P.;Simmie, J. M.;Gillespie, F.;Burke, U.;Connolly, J.;Metcalfe, W. K.;Battin-Leclerc, F.;Dirrenberger, P.;Herbinet, O.;Glaude, P. A.;Curran, H. J., *Proc. Combust. Inst.*, **2013**, 34, 225-232.

[126] Metcalfe, W. K.;Dooley, S.;Dryer, F. L., *Energy Fuels*, **2011**, 25, 4915-4936.

[127] Kéromnès, A.;Metcalfe, W. K.;Heufer, K. A.;Donohoe, N.;Das, A. K.;Sung, C.-J.;Herzler, J.;Naumann, C.;Griebel, P.;Mathieu, O.;Krejci, M. C.;Petersen, E. L.;Pitz, W. J.;Curran, H. J., *Combust. Flame*, **2013**, 160, 995-1011.

[128] Lowry, W.;de Vries, J.;Krejci, M.;Petersen, E.;Serinyel, Z.;Metcalfe, W.;Curran, H.;Bourque, G., *J. Eng. Gas Turbines Power Tran. ASME*, **2011**, 133, 091501.

[129] Healy, D.;Donato, N. S.;Aul, C. J.;Petersen, E. L.;Zinner, C. M.;Bourque, G.;Curran, H. J., *Combust. Flame*, **2010**, 157, 1526-1539.

[130] Laskin, A.;Wang, H.;Law, C. K., *Int. J. Chem. Kinet.*, **2000**, 32, 589-614.

[131] Cheng, Z.;Xing, L.;Zeng, M.;Dong, W.;Zhang, F.;Qi, F.;Li, Y., *Combust. Flame*, **2014**, 161, 2496-2511.

[132] Djokic, M.;Carstensen, H.-H.;Van Geem, K. M.;Marin, G. B., *Proc. Combust. Inst.*, **2013**, 34, 251-258.

[133] Alexandrino, K.;Millera, Á.;Bilbao, R.;Alzueta, M. U., *Proc. Combust. Inst.*, **2015**, 35, 1717-1725.

[134] Gueniche, H. A.;Glaude, P. A.;Fournet, R.;Battin-Leclerc, F., *Combust. Flame,* **2007**, 151, 245-261.

[135] Husson, B.;Bounaceur, R.;Tanaka, K.;Ferrari, M.;Herbinet, O.;Glaude, P. A.;Fournet, R.;Battin-Leclerc, F.;Crochet, M.;Vanhove, G.;Minetti, R.;Tobin, C. J.;Yasunaga, K.;Simmie, J. M.;Curran, H. J.;Niass, T.;Mathieu, O.;Ahmed, S. S., *Combust. Flame*, **2012**, 159, 1399-1416.

[136] Grela, M. A.;Amorebieta, V. T.;Colussi, A. J., *J. Phys. Chem.*, **1985**, 89, 38-41.

[137] Lifshitz, A.;Bidani, M.;Bidani, S., *J. Phys. Chem.*, **1986**, 90, 5373-5377.

[138] Vasiliou, A.;Nimlos, M. R.;Daily, J. W.;Ellison, G. B., *J. Phys. Chem. A*, **2009**, 113, 8540-8547.

[139] Liu, R.;Zhou, X.;Zhai, L., *J. Comput. Chem.*, **1998**, 19, 240-249.

[140] Higgins, J.;Zhou, X.;Liu, R., *J. Phys. Chem. A*, **1997**, 101, 7231-7235.

[141] Liu, R.;Zhou, X.;Zuo, T., *Chem. Phys. Let,*, **2000**, 325, 457-464.

[142] Hidaka, Y.;Nakamura, T.;Miyauchi, A.;Shiraishi, T.;Kawano, H., *Int. J. Chem. Kinet.*, **1989**, 21, 643-666.

[143] Giri, B. R.;Fernandes, R. X.;Bentz, T.;Hippler, H.;Olzmann, M., *Proc. Combust. Inst.*, **2011**, 33, 267-272.

[144] Harding, L. B.;Klippenstein, S. J.;Georgievskii, Y., *J. Phys. Chem. A*, **2007**, 111, 3789-3801.

[145] Somers, K. P.;Simmie, J. M.;Metcalfe, W. K.;Curran, H. J., *Phys. Chem. Chem. Phys.*, **2014**, 16, 5349-5367.

Publications

Publications in peer-reviewed scientific journals

Weber, I.; Golka, L.; Olzmann, M. ‘Thermal decomposition of propene: A shock-tube/ H-ARAS and modeling study’ *Proc. Combust. Inst.*, **2017**, 36, 299-306.

Presentations on Scientific Conferences

Weber, I.; Syskowski, S.; Olzmann, M. ‘Thermal decomposition of pentadienes: The effect of resonance stabilization on the kinetics’ International Conference on Chemical Kinetics, 2015, Ghent, Belgium.

Weber, I.; Golka, L.; Olzmann, M. ‘Thermal decomposition of propene: A shock-tube/ H-ARAS and modeling study’, 36th International Symposium on Combustion, 2016, Seoul, South-Korea.

Weber, I.; Genthner, L.; Friese, P.; Olzmann, M. ‘Pyrolysis of furan and its methyl-substituted derivatives: A H-ARAS/TOF-MS shock-tube study’, Rapid Poster Talk, Cleaner Combustion and Diagnostics, Bunsen Discussion Meeting, 2017, Bielefeld, Germany.

Poster Presentations

Golka, L.; Weber, I.; Olzmann, M. ‘Thermal decomposition of propene: A shock-tube/ H-ARAS and modeling study’, Bunsen Tagung 2016, Rostock, Germany.

Weber, I.; Genthner, L.; Friese, P.; Golka, L.; Olzmann, M. ‘Comparative study of the initial steps in the pyrolysis of furan and its methyl-substituted derivatives’, 36th International Combustion Symposium 2016, Seoul, South-Korea.

Weber, I.; Genthner, L.; Friese, P.; Olzmann, M. ‘Pyrolysis of furan and its methyl-substituted derivatives: A H-ARAS / TOF-MS shock-tube study’, Cleaner Combustion and Diagnostics, Bunsen Discussion Meeting, 2017, Bielefeld, Germany.

Curriculum Vitae

Personal Details

Name:	Isabelle Kathrin Weber
Place of birth:	Frankfurt am Main, Germany
Nationality:	German

Education

1995 – 1999	Anna-Schmidt-Schule, Frankfurt am Main
April – July 1999	Grundschule am Tegelschen Ort, Berlin
1999 – 2007	Humboldt-Gymnasium Berlin-Tegel, Berlin
2007	Abitur
July – Dec. 2007	Aspect College Perth, Perth, Australia
2008 – 2013	Studies of chemistry at the Karlsruhe Institute of Technology (KIT), Karlsruhe
Oct. 2013	Diploma
Since Oct. 2013	Scientific coworker at the Institute of Physical Chemistry, Molecular Physical Chemistry Group (Prof. Dr. M. Olzmann), Karlsruhe Institute of Technology (KIT), Karlsruhe